Experimental Characterization and Simulation of a Tethered Aerostat with Controllable Tail Fins

Alistair John George Howard

Department of Mechanical Engineering
McGill University, Montreal
September 2007

A thesis submitted to McGill University in partial
fulfillment of the requirements of the degree of
Masters of Engineering

Abstract

This research investigated the use of a streamlined aerostat with movable tail fins to control the pitching motion of an aerostat in a turbulent wind environment. The goal of the research was to reduce the pitch fluctuations of the aerostat by actively controlling the tail fins. A streamlined aerostat with four rigid tail fins was modified to include flap type trailing edge control surfaces on the horizontal tail fins. Airborne sensors and a ground station with wind sensors were used for the control of the aerostat and data logging.

In order to characterize its motion and to establish a performance baseline, the aerostat was flown numerous times without active control. The effectiveness of the tail-fin control surfaces was determined by measuring the open-loop response of the aerostat to a step change in the control surface deflection. The results from the uncontrolled and open loop testing were used to develop the closed loop control system which was then tested experimentally.

An additional goal of this research was to adapt a non-linear dynamic simulation to simulate the controllable aerostat used in this experiment. The experimental aerostat's aerodynamic and geometric properties were characterized for use in the dynamic model. In general, the 'non-dynamic' quantities in the simulation showed a good match and the dynamic variables did not show as good of a match between the simulation and the experiment suggesting that the model does not correctly represent the dynamic behaviour of the aerostat.

Résumé

Cette recherche a examiné l’utilisation d’un ballon à ligne profilée avec ailettes mobiles pour contrôler le tangage de ce ballon dans un environment venteux. Le but de cette recherche a été de réduire les fluctuations de l’inclinaison du ballon en contrôllant activement les ailettes arrières. Un ballon à helium à ligne profilée avec quatre ailettes rigides a été modifié en ajoutant des surfaces de contrôle du type aileron sur les ailettes arrières horizontales. Des capteurs à bord de l’aérostat et une station terrestre avec capteurs de vent ont été utilisés pour le contrôle de l’aérostat et l’entrée des données.

Pour caractériser le mouvement et pour etablir une performance de base de l’aérostat, il a été volé plusieurs fois sans contrôle actif. L’efficacité des surfaces de contrôle sur les ailettes arrières a été determinée en mesurant la réponse à boucle ouverte de l‘aérostat d’un changement progressif du braquage des surfaces de contrôle. Les resultats des tests non-contrôlés et de ceux contrôlés à boucle ouverte de l’aérostat ont étés utilisés pour développer le système à boucle fermée qui a ensuite été testé expérimentalement.

Un but additionel de cette recherche a été d’adapter une simulation dynamique non-linéaire pour simuler l’aérostat contrôlable utilisé dans cette expérience. Les propriétés aérodynamiques et géometriques de l’aérostat experimental ont étés caractérisés pour utilisation dans ce modèle dynamique. Géneralement, les quantités ‘non-dynamiques’ dans la simulation étaient en bonne correspondence pendant que les variables dynamiques correspondaient moins bien entre la simulation et les données expérimentales. Ceci suggère que ce modèle ne représente pas entièrement correctement le comportement de l’aérostat.

Acknowledgements

First and foremost I would like to express my sincere gratitude to my supervisor, Meyer Nahon, for taking me on as a student, giving me the support necessary for a difficult project, and for remaining patient with me throughout the past three years.

I would like to thank Philippe Coulombe-Pontbriand for the immense amount of time and energy that he spent helping me with this project. There's no doubt that I owe much of my success with this thesis to him. Thank you to Etienne Frenette, for all of his skill, assistance, time, and energy. Thanks to Casey Lambert for giving me advice, helping me work through my simulation code, and on numerous occasions being available to spend a day flying the aerostat.

I would also like to thank the group of co-op students who worked with me during the project for bring their new ideas and energies. These students are Magnus Nordenborg, Karel Steurs, and Florent Brossat.

Thank you to Ian Strachan for the use of his aerostat during my first year of experimentation, and for the loan of instrumentation. Also, thank you to Inna Sharf for generously allowing me to use her brand new orientation sensor for an entire summer.

Thanks to Nick Rowe for getting me on my bike every day and back into racing. Thanks to my Mom and Dad for their support. Finally, big thank you to my wife, Lisa, for supporting me in everything I do and being there for me each and every day.

Table of Contents

List of Figures

List of Tables

Chapter 1 Introduction

1.1 Background

An aerostat is a lighter-than-air vehicle that takes advantage of buoyancy to create lift. The term “aerostat” is derived from the “aerostatic” lift force that is created by the buoyancy of the aerostat’s body. The body typically contains a lighter-than-air gas, such as helium, which creates the craft’s buoyancy. Tethered aerostats are permanently attached to the ground through a cable or tether which permits them to station-keep and maintain a localized position without the expenditure of energy. This allows them to remain airborne for long-periods of time and makes them attractive for applications that require high-endurance aerial platforms. Tethered aerostats are used in a wide range of military, scientific, and surveillance applications. For example:

- The US Border Patrol and Drug Enforcement Agency uses a network of radar-equipped aerostats along the Mexican border to detect low flying aircraft [1].
- The US military uses aerostats similar to the one shown in Figure 1.2 for ‘over the hill’ surveillance [2].
- Scientists in Nova Scotia use an aerostat deployed from a ship to monitor the movement of whales in the Bay of Fundy [3].
- A Canadian design called the “Large Adaptive Reflector” (LAR) would use an aerostat to support the receiver of a large radio telescope, shown in Figure 1.1 [4].

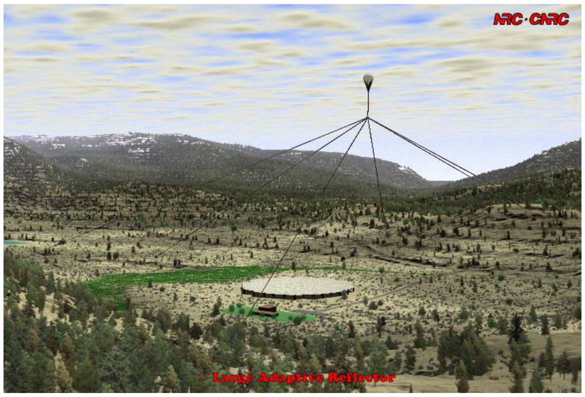

Figure 1.1 - The Large Adaptive Reflector concept [5]

Figure 1.2 - TCOM's 17M aerostat with sensor package mounted to the belly [6]. This aerostat is commonly used for military applications.

In these and other applications, the aerostat will typically carry a payload with an instrumentation package such as a camera, antenna, or radar. Without exception, the aerostats are uncontrolled, and so to compensate for the aerostat's motion and tendency to align with the wind direction, the payload is sometimes mounted on a movable platform. This platform can turn and tilt to align the payload in the desired direction but it is limited to aligning the payload with a specific axis. When the aerostat is subject to a turbulent wind, this can be a challenging task. In informal discussions with users it was noted that the most problematic motion was the pitching motion of the aerostat which was particularly difficult to compensate for with a movable payload platform. The LAR project presents an additional challenge. In this application, the principal requirement is for the tension in the aerostat's tether to remain as constant as possible [4].

1.2 Thesis Objectives and Motivation

There exist numerous applications where an aerostat with a stable and predictable motion, specifically about the pitch axis, would be desirable. Furthermore, reducing the fluctuations in pitch might accomplish a second desirable goal of reducing the variations in the tether tension.

Many different methods to actively control a tethered aerostat are possible and other passive methods to improve the performance have been proposed [7]. Although most of them have been routinely applied in other applications, none of these methods has ever been attempted experimentally with a streamlined tethered aerostat. One promising method of pitch control is to use actuated horizontal fins, as is done in conventional aircraft and airships. However this approach has never been applied to a tethered aerostat.

All prior modelling and simulation tools developed for aerostats have assumed a completely passive aerostat. In parallel with the development of an experimental facility for actively controlled aerostats, there is a need for these simulation tools to be improved in order to predict the performance of a controllable aerostat.

1.3 Literature Review

Outside of a limited group of researchers and companies, tethered aerostats have received little attention in literature. The majority of the attention has been directed towards the development of non-linear dynamic simulations of large, tethered streamlined aerostats [8].

Experimental characterization of an aerostat is an expensive and resource intensive study. The U.S. Army has invested large amounts of resources performing full scale flight testing of an instrumented 71 m long aerostat [9]. The costs and manpower required to fly an aerostat of this size and to its operational altitudes (> 2500 m) are prohibitive. For this reason, research has been focused on the development of dynamic models in order to accurately predict an aerostat's performance before an expensive full-scale aerostat is deployed. At the university level, the validation of these models has typically been performed with less expensive smaller aerostats. Canadian researchers have developed a concept for a large radio telescope (LAR) using an aerostat to support the telescope's receiver [4]. As a proof of concept and to improve their dynamic understanding, the researchers experimentally tested a one-third scale experimental model of the aerostat

[10]. Even at one-third scale, the aerostat measured 18 metres. In 2005, Coulombe-Pontbriand designed and built a small scale experimental testing facility where he investigated the dynamic characteristics of a spherical aerostat [11]. Coulombe-Pontbriand's work was used as a foundation for this thesis and was central to the development of the experimental system.

The majority of the dynamic models of aerostat are based on the 1972 work by Delaurier in which he performed a stability analysis of an aerodynamically shaped tethered balloon [12]. This work was the first to use a cable model and it resulted in a first-order solution to predict the motion of a tethered aerostat.

One of the more difficult problems encountered when modelling an aerostat is the determination of the aerodynamic parameters. In 1981, Jones and Delaurier, developed techniques to approximate the aerodynamic parameters of an aerostat [13]. This work was based on wind-tunnel testing of five scale model aerostats. Jones and Krausman used these aerodynamic estimation methods and developed a non-linear dynamic simulation of a tethered aerostat and validated their simulation using experimental results [14]. Jones also validated the experimental model by using wind tunnel tests with a 1/72 scale model [15].

The dynamics model used in the research presented in this thesis was originally developed by Lambert [16]. Lambert combined the dynamics model developed by Jones and Delaurier with methods developed by Nahon [17], to simplify the implementation in a non-linear dynamics model. This model was validated against experimental results for an 18 m aerostat in 2006 [10].

After the aerostat itself, the most important component of the aerostat model is the tether. Jones and Krausman used a discretized lumped-mass tether in 1982 in the first 3-D nonlinear dynamics model [14]. The implementation of the tether in the model used in this thesis was developed by Driscoll and Nahon [18] for use with the mathematical modelling of moored buoy systems. This model incorporates the effects of cable stiffness, internal damping, gravity, drag, and has been validated experimentally [16].

Very little research has been performed on active control of streamlined tethered aerostats. One proposal that incorporates active control and a tethered aerostat is the LAR project [4]. However, in this implementation the aerostat itself is passive, and a network of tethers is used to control the position of the aerostat. In 2005, as part of the LAR project, Deschenes and Nahon looked at methods of reducing an aerostat's payload motion by incorporating various forms of active and passive control [19]. This research used simulations to predict the performance of a streamlined aerostat suggested that it may be advantageous to control an aerostat with tail fins.

1.4 Research Overview

This research investigates using an aerostat with movable tail fins to control the pitching motion of a streamlined aerostat in a turbulent environment. A small streamlined aerostat with trailing edge control surfaces on the tail fins was tested experimentally. The experimental results were then used to validate a non-linear dynamics simulation of a small tethered aerostat. This thesis is divided into sections describing the experimental facility, the experimental flights, and the improvements made to the existing aerostat simulation.

The second chapter describes the development of the experimental facility. The facility includes a streamlined tethered aerostat with a wireless instrumentation system. The design process for the aerostat with controllable tail fins is presented including the assumptions that were made and the constraints imposed by the aerostat and component manufacturers. This chapter also illustrates in detail the wireless instrumentation system and its measurement capabilities. The method of measuring the aerostat's position, attitude, and tether tension in real-time is presented in detail.

The third chapter presents the program of experimental flights that were performed with the controllable aerostat. The method of, and issues with, characterizing an outdoor experimental environment based solely on wind speed is discussed. Results from both controlled and uncontrolled flights are given and the iterative development of the pitch control algorithm is shown. Finally some analysis of the performance of the controllable aerostat is presented.

The fourth chapter presents the work done on a non-linear, dynamic simulation of the aerostat. A description of the methods used to determine the various physical and aerodynamic parameters is given as well as a series of improvements to the wind-model. Finally, a brief comparison between the simulated aerostat and the experimental aerostat is made.

Chapter five concludes the thesis and gives a series of recommendations for future research.

Chapter 2 Experimental System

The experimental system developed for this project is an extension of work done at McGill University [20], [11]. The system consists of three major components: a streamlined tethered aerostat, an airborne instrumentation system, and a ground-based computer. A general overview of the system is shown in Figure 2.1.

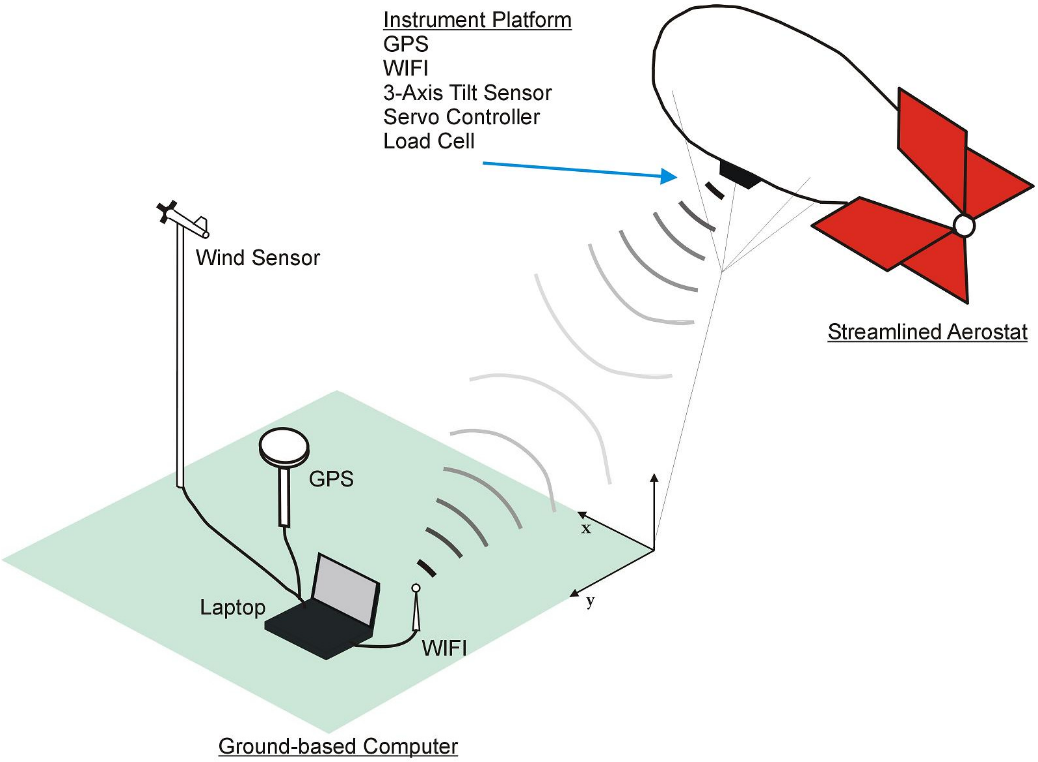

Figure 2.1 - Overview of the experimental system

An 8.76m long streamlined aerostat with four rigid fins was modified to include flap type control surfaces on the horizontal tail fins. Attached to the belly of the aerostat was an instrumentation system that provided position, orientation and tether tension data. The instrumentation system communicated with a ground based computer through a local area WIFI network.

The ground station monitored all instruments in real time and recorded the tether tension and aerostat orientation. Position data was collected through the use of a pair of high precision differential GPS receivers. This allowed for position to be accurately determined in real time with accuracy better than 3cm. One GPS unit was positioned on the instrument platform and the other was in a fixed position on the ground. A ground station also acquired wind direction and speed data from three wind sensors, shown in Figure 2.2, mounted on a nearby tower.

Figure 2.2 - One of three wind sensors mounted near the ground station

2.1 Aerostat Design

Prior research [7] on the LAR system indicated that an aerostat with controllable tailfins might yield substantial performance improvements in that system. Thus, the experimental goals were to investigate the control possibilities of a streamlined aerostat with movable tail surfaces. Since no such aerostat was commercially available, it was determined that an existing design would have to be modified four our purposes. Based on prior experience [11] at McGill University, Aerostar Inflatables was chosen as the aerostat manufacturer. Aerostar is an experienced manufacturer, producing a variety of helium inflatables including aerostats ranging in size from 3.7m to 15.2m.

The baseline aerostat chosen for this experiment had to meet a set of criteria:

- It should be safely operated by two persons
- It should have a free-lift of approximately 25 kg
- The fins should be rigid and modifiable for the addition of control surfaces

The TRF-900 streamlined aerostat manufactured by Aerostar was chosen as the starting point for the aerostat design. The TRF-900 is a 7.5 m long aerostat with four rigid tail fins configured in a horizontal and vertical arrangement. In consultation with our group, Aerostar modified the TRF to include controllable tail fins. They also extended the hull of the aerostat by 1.26 m to increase the buoyancy and compensate for the added weight of the controllable tail fins. The modified aerostat is 8.76m long with a maximum diameter of 2.95m and the fins have a span of 2.56m and is shown in Figure 2.3. The aerostat included 8 load patches to attach handling lines and the harness. The harness consisted of six nylon ropes in lengths from 2.96 to 4.18 m (Table 11 details the harness locations and lengths).

Figure 2.3 - TRF-900 streamlined aerostat manufactured by Aerostar

2.1.1 Tail-fin Design

The tail fin design was constrained by the torque that could be supplied to rotate the control surface. The tail-fin had to be sized so that an inexpensive and lightweight motor could be used as an actuator. As a starting point in the design of the horizontal control surfaces, it was decided to estimate the maximum possible flap chord, given the maximum torque of 2.35 Nm of a standard hobby style servo available at the time of design. Other assumptions made during the design process were:

- The servo arm and pushrod connecting arm would be of equal length (no gear ratio multiplying the torque).
- The maximum flap deflection would be 30 degrees
- The maximum free stream wind velocity would be 10 m/s
- The maximum angle of attack of the fin would be 30 degrees

The un-modified TRF-900 fins were constructed with a lightweight aluminum frame covered with Nylon. The fins were flat (no camber) and had a rectangular aspect ratio. Figure 2.4 shows a rear and side view of the tail fins. The Nylon covering was a single layer thick.

Figure 2.4 - Rear and side views of the TRF-900 aerostat showing the tail fin construction

To estimate the aerodynamic parameters, the fin was approximated as a flat plate with a 2-D lift curve slope of 2π. Its tip-tip span was 2.26m and the chord was 1.55m + c_f with c_f the unknown flap chord length.

Jacobs [21] gives the lift coefficient of a symmetrical airfoil with trailing flap as

$$C_L = a \cdot (\alpha + k\delta) \tag{2.1}$$

Where a is slope of the lift curve corresponding to the aspect ratio under consideration, α is the angle of attack, δ is the flap deflection and k is given by

$$k = \frac{\cos^{-1}(1-2E) + 2\sqrt{E(1-E)}}{\pi} \tag{2.2}$$

Where E is the ratio of flap chord to total chord. The torque required to deflect a full span (tip to tip) flap is given by

$$H = \frac{1}{2}\rho V^2 S_f c_f C_H \tag{2.3}$$

With ρ the density of air taken as 1.269 kg/m^3, V is the velocity of the air, c_f is the flap chord S_f is the flap area and C_H given by

$$C_H = h_o C_L - h\delta + C_{ho} \tag{2.4}$$

The parameters h and h_o are functions of E and are given by Jacobs [21], C_{ho} is the hinge moment at zero flap deflection (assumed to be zero).

Equation (2.4) was first used to determine the coefficient C_H as a function of the angle of attack, the flap deflection, and the chord ratio E. A maximum angle of attack of 30 degrees and a maximum flap deflection of 30 degrees were chosen arbitrarily to err on the conservative side.

The resulting function of the chord ratio, E, was then used in equation (2.3) to give the maximum torque, H, as a function of the chord ratio. Assuming a maximum torque of 2.35 Nm it was found that the maximum chord ratio is 0.156. This gives a chord length of 0.28m.

These calculations should be considered conservative. It is likely that a larger chord could be used. The calculations assume that the servo arm and the pushrod-connecting arm are of equal length. Therefore there is no multiplication of the moment due to gearing. The high-end digital servos can rotate +/-90 degrees from center. The flap deflection will be less than 90 degrees so we should be able to increase the effective torque by gearing the servos (changing the ratio of the servo arms and the pushrod arms). The influence of the aerostat body is completely ignored. It will affect the flow and reduce the effectiveness of the flaps therefore reducing the requisite torque.

The results from these calculations were used to design the control surfaces for the modified TRF-900 aerostat. A chord length of 0.315m was selected.

2.1.2 Servos

The horizontal control surfaces were actuated using robotic hobby servos. Hobby servos are widely available, reliable, inexpensive, and provide high levels of torque for their size and power requirements. They also function using a simple pulse train command and do not require specialized power sources. The HSR-5995TG (HSR) coreless digital servos shown in Figure 2.5 were chosen to actuate the tail fins because they were the servo with the highest torque available at the time of purchase.

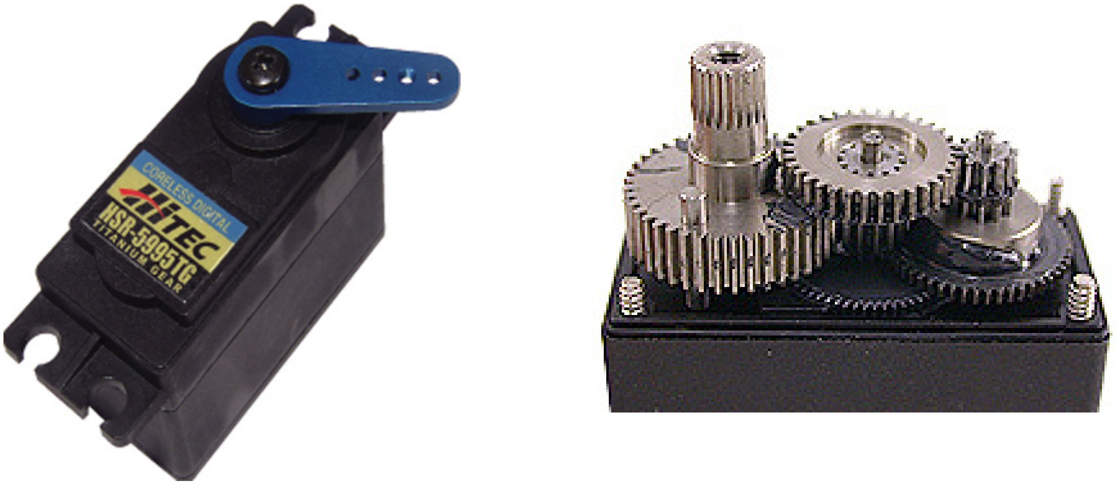

Figure 2.5 - Photographs showing outside and internals of the HITEC robotic servos [22]

The HSR is a specialized digital servo developed for robotic applications. It operates using a standard pulse train input and a supply voltage of 4.8 – 6.0V. It uses a titanium alloy gear and provides a stall torque of 2.94 Nm. Under no-load, the servo rotates at a speed of 500 deg/s [23].

The port and starboard control surfaces were each actuated by a separate servo. The servos were mounted to the underside of the rear tail fins and were attached to the rear control surface with a pushrod. The pushrod was offset from the control surface in order to increase the moment arm. The configuration is shown in Figure 2.6.

Figure 2.6 - Servo mounted on the fin with a pushrod

2.2 Instrumentation Platform and Sensors

The instrument platform housed all of the airborne sensors, the power supply, the batteries, and the communications hardware.

The instrument platform had a number of design requirements:

1. The instrument platform should be as lightweight as possible in order to minimize the effects on the dynamics of the aerostat
2. The platform should be strong and stable
3. Material choices should minimize magnetic interference with the orientation sensor.
4. The attachment method should be flexible to allow the positioning to be varied longitudinally on the aerostat
5. The attachment method must minimize the necessary alterations to the aerostat.

The instrumentation platform was an evolution of a platform successfully flown on a spherical aerostat by Coulombe-Pontbriand [11]. The new instrumentation platform offered many design improvements including improved wireless communications, more reliable load-cell instrumentation, and a stronger and reinforced platform. Additions to the platform included an orientation sensor, rechargeable batteries, a multi-voltage power supply, and a servo controller.

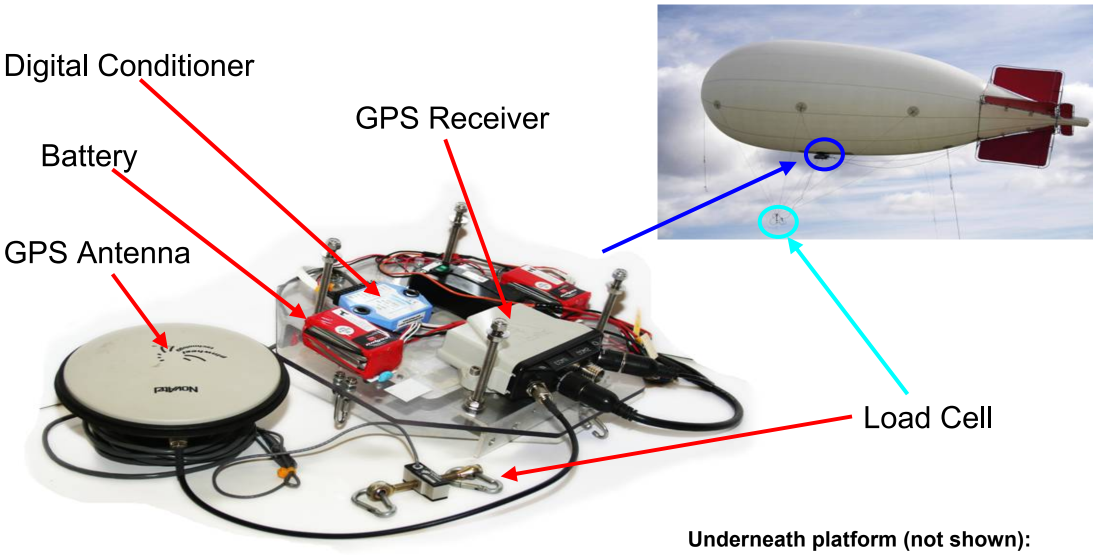

Underneath platform (not shown):

- Wireless Serial LAN
- 3-Axis Tilt Sensor
- Servo controller

Figure 2.7 - Instrumentation platform

The instrument platform was attached to the belly of the aerostat using Velcro and stabilization lines. A 1.4 m x 0.5 m section of Velcro was added to the belly of the aerostat and a smaller 0.5 m x 0.5 m section of Velcro was fixed to the instrument platform. Three stabilization lines attached to load patches at the side and rear of the aerostat helped hold the platform in place and acted as added security.

Polycarbonate was chosen as the material for the main platform because it offers many advantages including being very easy to machine and drill, which allows for quick modifications in the field and in the lab. It is also flexible enough to withstand some bending. Two pieces of L-channel aluminum were attached to the underside of the platform. These served three purposes: first, they reinforced the platform and gave strength to the support rods, second, they provided a convenient point of attachment for instruments and increased the available attachment points, and third, they acted as skids to protect the instruments when the platform was placed on the ground.

2.2.1 Tilt Sensor

Two widely available orientation sensors were considered for use on the aerostat. The Honeywell HMR3300 tilt sensor (HMR) and the Microstrain GX1 tilt sensor (GX1) were both chosen as options because of their low cost, availability, and support for RS232 communications.

Both the HMR and the GX1 use accelerometers to measure the earth's gravitational field, to calculate their respective roll and pitch angles. The GX1 has additional rate gyros which improve the roll and pitch angle readings. Both sensors also use magnetometers to measure the yaw orientation of the sensor with respect to the earth's magnetic field.

To check the dynamic performance of the two sensors they were both mounted on a 2.24 m long pendulum which was attached to a roof beam in the lab. Both the GX1 and the HMR were mounted so that their roll sensors would measure during the pendulum movement. A similar test was performed with the pitch axis and almost identical results were found.

The pendulum was released from an angle of approximately 20 degrees and then left to swing freely until its motion decayed. A magnetic sensor was mounted to record the time when the pendulum passed through 11.3 degrees. The output from this sensor was recorded using a USB DAQ.

Figure 2.8 shows the output for the HMR and the GX1 when released from just past 20 degrees. The HMR was sampled at 5 Hz (the maximum achievable sampling rate of this sensor) and the GX1 at 30 Hz. The horizontal dashed line represents the position where the magnetic sensor is located. The pendulum only passes through this point during its first few cycles and after that its motion has decayed too much. Also on this figure is a square wave showing each time the magnetic sensor is triggered. The measured frequency of oscillation is 0.4 Hz which is on the same order of magnitude as the dominant frequency of a tethered aerostat system.

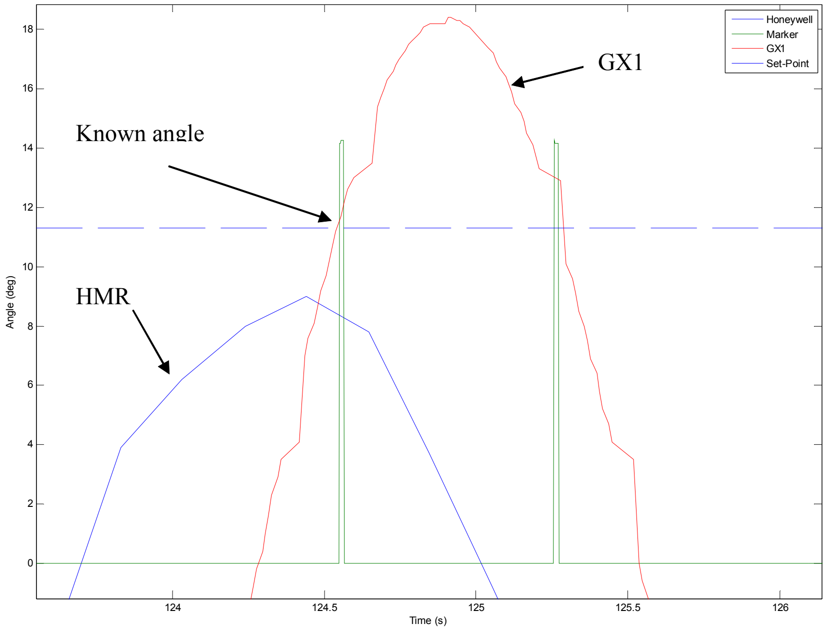

Figure 2.8 - Plot showing the angle measured by both the GX1 and the Honeywell tilt sensors while mounted on the pendulum.

These results show that the HMR does not measure the correct angle of the sensor during dynamic motion. This is likely because the HMR relies only on accelerometers to measure its angle with respect to the horizontal plane and therefore dynamic accelerations will affect its output. The GX1 uses a combination of accelerometers and rate gyros to measure its angle which provides better performance under dynamic motion.

Both sensors determine their heading by using magnetometers to measure the earth's magnetic field. Magnetometers are subject to interference from magnetic sources such as ferrous metals. In order to reduce the interference, care was taken during construction of the platform to eliminate any sources of magnetic interference. It is very difficult to avoid having to measure the earth's magnetic field in order to determine heading. The uses of dual GPS receivers to measure heading should be investigated in future implementations of the instrument platform.

Due to its better dynamic performance, the GX1 was chosen to measure the orientation of the aerostat. In addition to its better dynamic performance, the GX1 has a number of other advantages over the HMR [24, 25].

- The GX1 is capable of measuring a wider range of pitch and roll compared to the HMR (± 180^{o} compared to ± 60^{o}).
- The GX1 has a maximum sampling rate of 100Hz. The HMR advertises a maximum sampling rate of 8Hz, however in practice, 5Hz was more reasonable.
- The GX1 supports RS485 communications which allows for multiple instruments to use a single serial line. This will provide some flexibility when planning future instrumentation upgrades.

2.2.2 Load Cell and Analog to Digital Converter

The tension in the main tether was measured using a Transducer techniques MLP-75 load cell [26]. The MLP-75 is capable of measuring a maximum load of 34kg (75lb). The unit operates using a voltage bridge with an excitation of 10 VDC and an output of 2mV/V and includes built in temperature compensation. The MLP-75 was positioned at the confluence point of the six harness tethers and the single main tether as shown in Figure 2.7.

The MLP-75 was connected to an Omega D1521 analog to digital converter that provided a 5 VDC excitation to the load cell, measured the load cell output at 5Hz [27], and converted the analog input to an ASCII output for transmission to the DIGI wireless server using RS232.

2.2.3 GPS

Position data was collected at 10Hz through the use of a pair of high precision differential GPS (DGPS) receivers. Our implementation of DGPS consisted of a base station receiver located at a fixed control point on the ground and a roving receiver on the instrumentation platform. The ground station was a dual-frequency Novatel DL-4 plus GPS receiver and the rover was a Novatel FlexPak-G2L dual-frequency receiver. Both the rover and the base station were equipped with Novatel 702 dual-frequency L1/L2 antennas. The output of each receiver was recorded in GPB format for later processing. Each receiver also produced ephemeris data, which was recorded as EPP files in order to improve the precision of the post-processed data.

Post processing of the GPS data was performed using the GrafNav DGPS software from Waypoint Consulting Inc. The post processing of the GPS data allowed for the 3-D position to be determined with an accuracy better than 3 cm [11].

2.2.4 Power Supply

The power-supply for the instrumentation system was designed to meet a range of requirements.

1. It should be capable of providing three different voltage outputs (5 VDC, 8 VDC, and 12 VDC).
2. It should be able to supply a separate voltage with a large current to the servos.
3. It is necessary to minimize possible magnetic interference.
4. It should be lightweight and if possible, rechargeable.

The current draw of a prototype instrumentation platform, measured in a laboratory test (10.41 V supplied), is shown in Table 1, along with the manufacturer specified voltage requirements for each component.

Table 1 – The voltage and current requirements of the various components on the instrumentation platform. Current requirements are for 10.41V supplied.

Instrument	Current (A)	Voltage (V)
GPS with Antenna	0.30	6 – 18
Omega Digital Conditioner and Load Cell	0.10	10 – 30
DIGI Wireless Server	0.53	9 – 30
GX1 Tilt Sensor	0.03	5.2 – 12
Servo 8 Torque Board servo controller	0.01	5.5 – 9
Total	0.97	Not applicable

The instrument platform also supplied the voltage for a pair of HITEC robotic servos. The power specifications for the robotic servos are shown in Table 2.

Table 2 - Specified current requirements for two HITEC robotic servos

Servo	Current (A)	Voltage (V)
No load	0.03	5
Locked	4.20	5

It was difficult to make estimates of the current use of the servos during flight because the load on the servos and activity level of the servos could only be roughly estimated. For the power supply design, it was estimated the instrument platform would require 1 A and each servo would require a mean of 1 A. Therefore, the energy requirements would be 3 A at 5 V. From past experience, a minimum of 1 hour of flight time is necessary. This resulted in a requirement of 3000 mAh at greater than 10 V.

Because of the small lift capability of the aerostat and for simplicity, batteries were the obvious choice to store the energy required by the instrumentation.

FMA-Direct Cell-Pro rechargeable lithium-polymer batteries were chosen for energy storage on the instrument platform. These have very good energy density, have no magnetic characteristics, are rechargeable, and are readily available because of their popularity with radio-controlled aircraft flyers. Two 2000mAh FMA lithium polymer batteries were selected for the instrument platform providing a maximum voltage of 16.8V and a current capacity of 4000mAh.

The power supply system was split into three tiers:

1. 5V regulated supply for the servos. Two 5V LM1084 voltage regulators were used to provide the servos with a regulated power supply. These were installed with 30W heat sinks exposed to the air flow across the bottom of the instrument platform.
2. 8V regulated supply for the GX1 and the servo controller board.
3. Unregulated power for the GPS, DIGI Wireless Server, and the Omega D1521. Each of these instruments has built in voltage regulation capable of dealing with the full range of possible battery voltages.

2.2.5 Servo Controller

Each servo is controlled by sending a 50Hz pulse train over a signal wire. The position of the servo is determined by the width of the pulse which can vary between 1ms and 2ms. To control the servos through an RS232 link from the ground based computer, a Netmedia Servo 8 Torque Board (NS8) was used. The NS8 converts an ASCII command received through its RS232 port into a 50 Hz pulse train for a servo. It is possible to control up to 8 servos using the NS8.

2.2.6 Wireless Communications

The instrumentation on the platform communicated with the ground based computer through a Digi PortServer TS W MEI wireless server (Digi). The Digi has four switch selectable RS232/422/485 RJ45 ports which accept the sensor inputs. It provides a wireless link to the ground based computer though an 802.11b wireless Ethernet network [28]. The software on the ground-based computer communicated with the instruments through the Digi using either TCP sockets or virtual serial ports. Each instrument connected to the Digi through a serial connection. The Digi is highly configurable and provides robust communications at baud rates up to 115.2kbps. Figure 2.9 shows a schematic describing the connection between each device and the communications between the airborne and ground station.

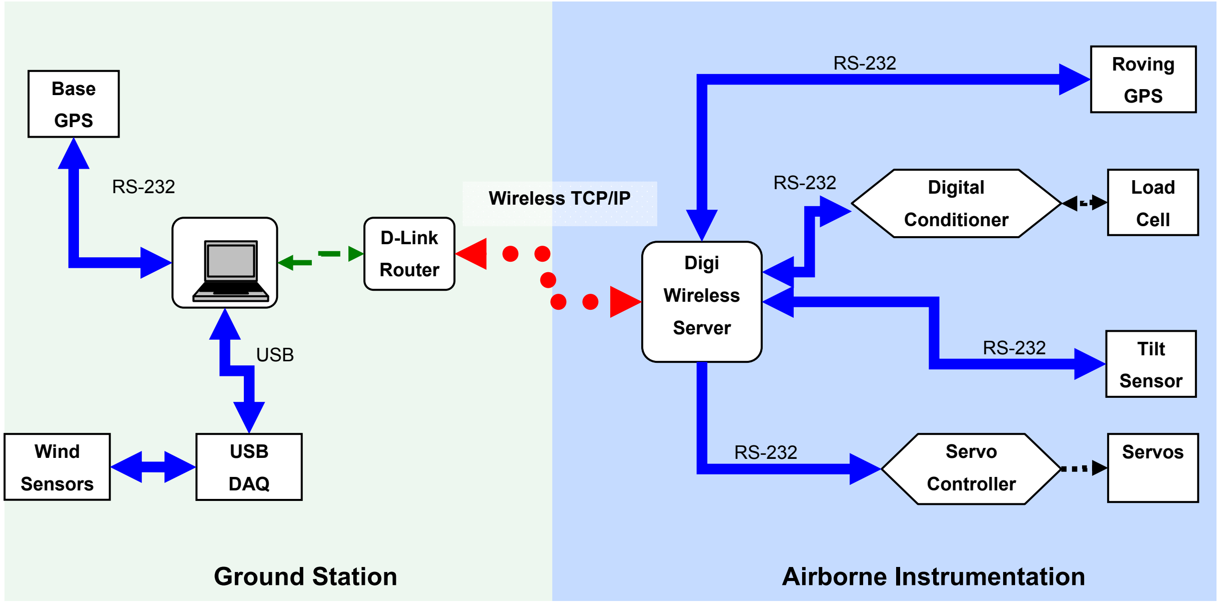

Figure 2.9 - Schematic of the communication between each instrument

The control system is implemented on the ground based computer which communicates wirelessly with the instrumentation platform and flap actuators. This introduces a time lag in the control system which is aggravated by the response of the servos and the mechanical linkage.

The magnitude and phase response of the servo system was determined experimentally by measuring the output flap angle in response to input servo arm commands at different frequencies. The output flap angle was measured with a potentiometer attached to the hinge of the flap. The resistance of the potentiometer changed in relation with the angle of the flap and the relationship between the angle and resistance of the potentiometer was determined experimentally. The servo angle was commanded by the servo controller using a laptop programmed to output a servo command signal.

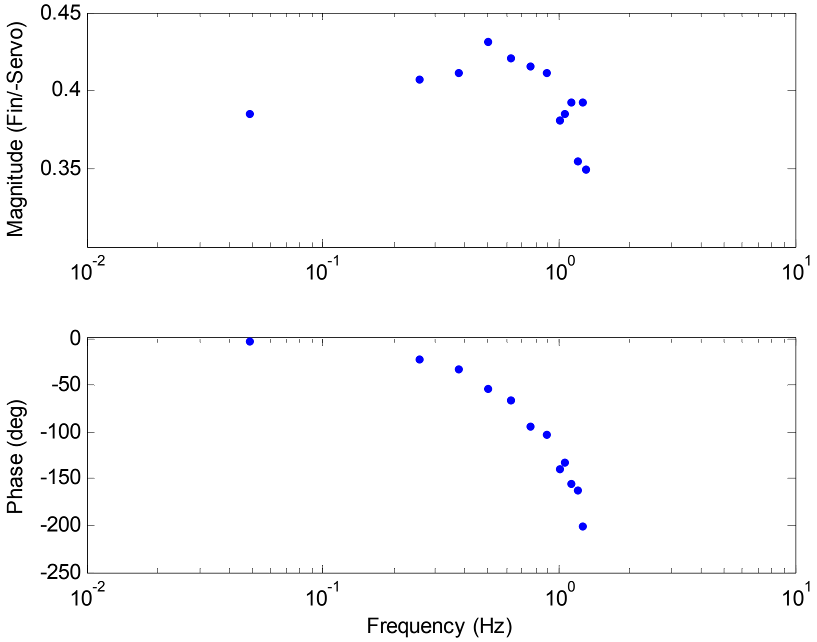

Figure 2.10 - Experimental magnitude and phase response of the servo control system

Figure 2.10 shows the magnitude and phase response of the entire control system. The output of this system is the measured flap angle and the input is the angle commanded by the laptop computer. Beyond 1.25 Hz the response of the system became erratic and impossible to measure. The controller is only effective up to approximately 1Hz, beyond which the response drops off sharply and the delay increases quickly.

2.3 Ground Station

The ground station acts as a central control station for the aerostat system. The central component of the ground station was an IBM ThinkPad personal laptop that monitored the airborne instruments, recorded the wind sensor data, recorded the base-station and roving GPS raw data, and processed the control-algorithms that were used to determine the actuation of the tail fins. The ground based computer communicated with the airborne wireless server through a D-Link DI-614 802.11g wireless router that was configured as an access point.

2.3.1 Winch

An A.G.O. Environmental Electronics Ltd. CSW-1 winch was available from previous research performed at McGill University [11] and is shown in Figure 2.11. The winch is powered by a standard 12V car battery. It is capable of retrieving a 30kg load at a rate of 6-10 m/min [11].

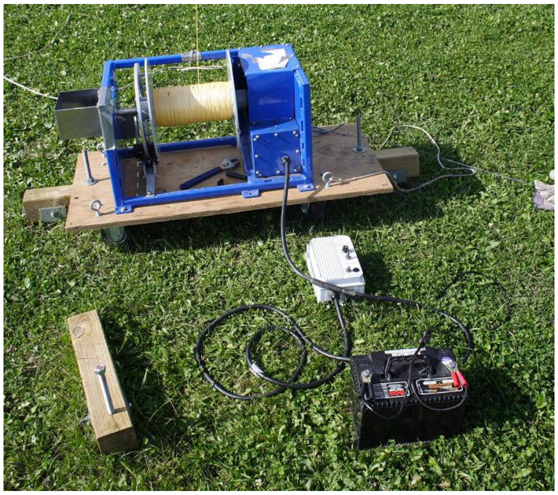

Figure 2.11 - CSW-1 winch with control box and battery power

The winch is mounted on a mobile platform so that it can be stored between flights. When deployed, the winch was secured to a base station at the launch site. The base station consists of three metal anchors driven 1.2 m into the ground. The winch platform is bolted to two of the three anchors. This provides a stationary base to launch the aerostat from. The arrangement of the anchors allows for four different winch orientations and the orientation for a particular flight was chosen depending on the dominant wind direction.

2.3.2 Tether

The size of the main tether was chosen by estimating the maximum static tension in the tether based on the aerostat's lift and drag. The drag force of the aerostat is given by:

$$D = \frac{1}{2}\rho U^2 A C_D \tag{2.5}$$

where C_D is the drag coefficient estimated as a cylinder to be 0.2, ρ is the air density taken as 1.229 kg/m^3, U is the free stream wind velocity, and A is the reference area which was 10.73 m^2.

Assuming that there is equilibrium between the free lift of the aerostat L, the tension T, and the drag D we can solve for T using

$$T = \sqrt{L^2 + D^2} \tag{2.6}$$

Equation (2.5) gives a tension of 385 N at 15 m/s. Under real-world conditions, the peak tension in the tether would be higher than the equilibrium tension due to the accelerations of the aerostat. Because of this, and from past experience, it was decided that a safety factor of at least 5 would be required for the minimum strength of the tether.

Plasma 12 Strand polyethylene synthetic rope from Cortland cable was chosen for the main tether based on past experience at McGill University [11]. Plasma rope has a high strength to weight ratio and high elastic modulus. The closest Plasma cable that meets the design requirements of the aerostat is the 1.75mm 12 strand nylon cable whose properties are shown in Table 3.

Table 3 - Properties and specifications of Cortland 1.75 mm dia Plasma 12 Strand Nylon cable

Diameter (mm)	**Density (kg/m^3)**	**Elastic Modulus (Gpa)**	**Minimum Tensile Strength (kN)**	**Safety Factor**
1.75	830	38	3.3	8.5

2.3.3 Software

Custom software, called the "Aerostat Data Logging and Control System" (AeroDacs), was developed by Etienne Frenette, another Masters student in the lab, for data-acquisition and control using LabView. A screenshot of the software is shown in Figure

2.12. AeroDacs was installed on the ground based computer (shown in Figure 2.9) and was used for two main functions:

1. The synchronization, acquisition, and recording of all the data from all the instruments.
2. The processing of specific data in real-time, computation of control algorithms, and transmission of commands to the tail-fin servos.

The acquisition of data from the instruments was performed in two different ways. The wind speed and wind direction were sampled directly using a USB DAQ. This sampling was through a USB connection and was performed at 5 Hz. The instruments onboard the aerostat (load cell, and tilt sensor) were connected to the ground based computer through a TCP/IP connection as outlined in Section 2.2.6. Both instruments required AeroDacs to send a request for data to which they would reply with the most recent data sample. Both instruments were sampled at 5 Hz.

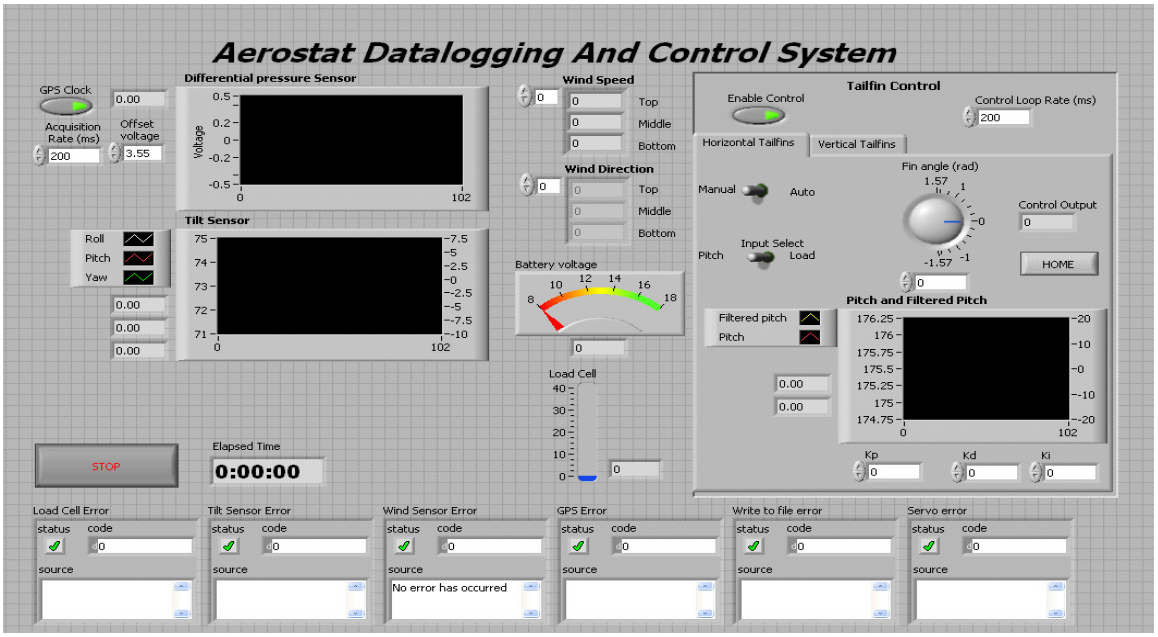

Figure 2.12 - Screenshot of the AeroDacs software used for controlling the aerostat from the ground based computer and logging sensor data

AeroDacs processed the acquired tilt-sensor data in real-time and used the PID control algorithm to generate a desired servo command. This servo command was sent through the TCP/IP connection by AeroDacs to the servo controller (Figure 2.9). AeroDacs made it possible to adjust the gains used by the PID in real-time. This allowed for adjustments to the PID and control system as well as debugging to be made with the aerostat at altitude. The PID control was operated in synchronization with the data-acquisition at 5 Hz.

AeroDacs displayed the data from each instrument in real-time. This facilitated observations of the behavior of the aerostat from the ground. AeroDacs also allowed manual control of the tail fins, which made open-loop control and the debugging of the control system easier.

AeroDacs used the ground station GPS as an external clock to time-synchronize all of the instruments. The GPS data from both the rover and the base station were recorded with separate software from Waypoint Consulting called RTK-Nav. RTK-Nav is real-time DGPS processing software; however in this implementation, it was used strictly as a means to acquire and record the raw GPS data which was later post-processed using Waypoint Consulting's GrafNav (post-processing the GPS data results in better accuracy and lower computational costs in the field).

2.3.4 Wind Sensors

Three R.M Young 05103-10 anemometers from Campbell Scientific, as shown in Figure 2.13, were used to measure the wind speed and direction. The sensors were mounted on a tower approximately 10 metres from the ground station at 2.56 m, 6.1 m, and 9.7 m above the ground. The output of each sensor was recorded using a PMD-1208FS USB DAQ. The raw data was then post-processed using Matlab.

Figure 2.13 - Wind sensor tower with three Young sensors mounted at different heights

Each wind speed sensor outputs a sinusoid which is related to the wind speed by its frequency [29]:

$$U = 0.098f \tag{2.7}$$

where U is the wind speed and f is the measured frequency of the sinusoid.

A Fast-Fourier transform of each 0.2 s portion of raw data was performed using Matlab. The dominant frequency in each portion was extracted and used in equation (2.7). This gives a sampling frequency of 5 Hz.

Each wind direction sensor also outputs a pulse every five seconds. The magnitude of this pulse is related to the direction the wind is blowing from in degrees by [29]:

$$\theta_w = \frac{355}{2.5}W \tag{2.8}$$

where W is the pulse voltage, and θ_w is measured positive clockwise, viewed from above, with the zero angle representing true-north. The wind sensor direction was calibrated in order to verify equation (2.8). The differential GPS system was used to survey the wind tower to determine true north. It was determined that the cross beam on the tower points approximately true north. Its exact bearing was determined by the GPS survey.

While recording the voltage output, the bottom wind sensor was rotated through 360 degrees and the output was recorded. Table 4 shows the surveyed direction, the processed output from the sensor, and the error between the two.

Table 4 - Surveyed direction and sensor output for lower wind sensor

Surveyed Sensor Direction from True North (degrees)	Sensor Output Angle (degrees)	Error (degrees)
3.2	1.8	1.4
93.2	85.4	7.8
183.2	177.5	5.7
273.2	281.0	-7.8

A 12-bit PMD-1208FS analog to digital converter (PMD) was used to record the output from the wind sensors. The PMD was set to an input range of +/- 10V which has an accuracy of 0.029766 V [30]. The input resolution error combined with the accuracy of the PMD gives a total error of +/- 0.0322V. Using equation (2.8) this gives a total error due to the PMD of +/- 4.57^0. This error makes up the majority of the error shown in Table 4. The rest of the error can be attributed to measurement error. It should also be noted that only the bottom sensor was calibrated in this manner. It is assumed that the other two sensors functioned at the same accuracy.

The wind speed sensor measures the wind speed using a propeller. The inertia of the propeller introduces a phase lag to the measurement. A propeller anemometer, such as the Young's wind sensor is a first order system that is defined by its time constant [31]:

$$\tau = {}^{L}\!/_{U} \tag{2.9}$$

Where L is the distance constant and U is the mean wind speed. The time constant τ depends on the wind speed.

The distance constant is defined as the length of fluid flow that must pass for a sensor to respond to 63.2% of a step change in speed. For the Young's wind sensor, the distance constant is 2.7m [29].

Using equation (2.9), at the mean wind speed measured on July 19th of 2.2 m/s, the time constant of the Young sensor is 1.23 sec. Figure 2.14 shows the bode plot of a first order system with a time constant of 1.23 sec.

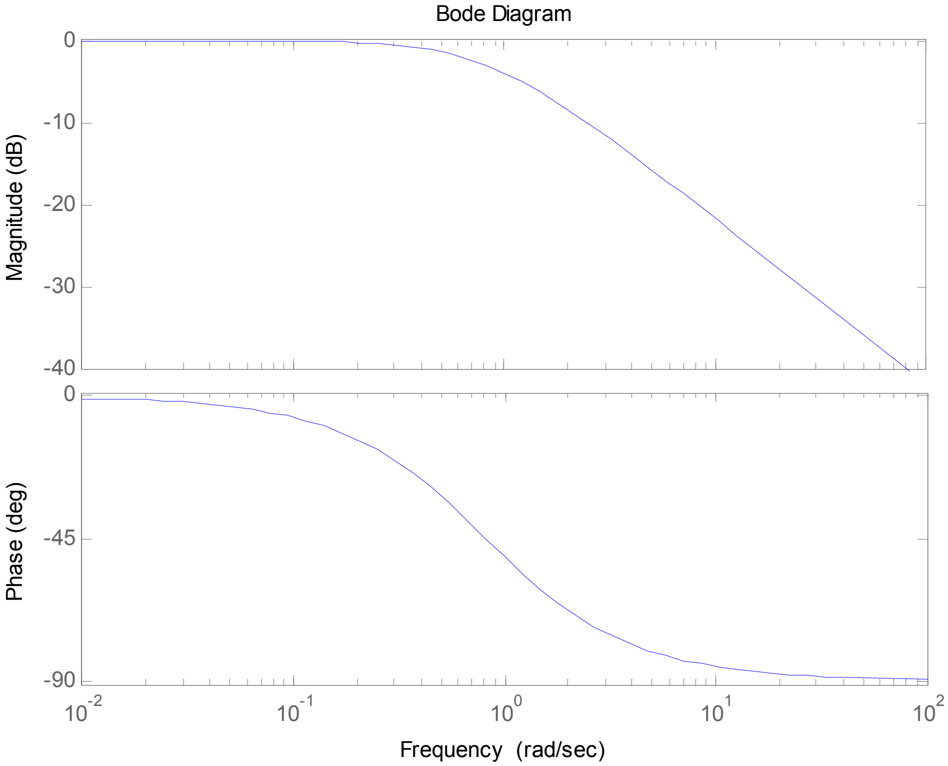

Figure 2.14 - Bode plot for a first order system with a time constant of 1.23 sec

The phase lag and attenuation increases in general with increasing frequency. This introduces some uncertainty to the measurement of the wind speed, especially on days where the wind speed was higher and with more high frequency content. Compensation for this was not implemented as it was expected that the aerostat system itself would act as a low-pass filter and so it would not respond to the high frequency portions of the wind speed.

Chapter 3 Results

This chapter is divided into two main sections. The first explains the manipulation of the experimental data in order to improve its interpretation and to derive other information from it. The second section presents and interprets the results obtained during the experimental program.

3.1 Experimental Data Processing

In general, very little post-processing or manipulation was performed on the raw data collected from the GPS, the instrumentation system, or the wind sensors beyond what was described in Chapter 2. However:

- The coordinate system for the position data was transformed in order to express the motion of the aerostat into the along-wind (longitudinal) and transverse (lateral) directions.
- The wind speed was extrapolated to estimate the wind speed at the aerostat's height.
- A sonic anemometer was used to evaluate the results obtained from the Young sensor and to obtain information about the vertical wind gusts.

Each of these procedures is described in more detail in the following sections.

3.1.1 Coordinate System Transformation

A differential GPS system was used to record the time history of the position of the aerostat. As explained in detail in Chapter 2, the system consisted of a base station GPS and a roving GPS on the aerostat. Three steps were performed to post-process the data into a form that was useful for analysis.

The first step was to process the differential data using GrafNav DGPS software from Waypoint Consulting Inc. This software provided multiple output formats for the position data including longitude/latitude coordinates and earth-fixed coordinates. For this analysis, a local coordinate system was chosen where the y-axis points true-north, the x-axis points true-east, and the z-axis is vertical upwards, parallel with the gravity vector. The output of the DGPS software gave a relative position vector from the base station GPS to the aerostat's GPS.

The second step was to rotate the local-coordinate system to be in line with the mean wind direction. This allowed the motion of the aerostat to be decomposed into longitudinal (in-line with the wind) and lateral (perpendicular to the wind) components. Decomposition into longitudinal and lateral motion simplified the interpretation of the motion of the aerostat and provided insight into its oscillatory nature.

To perform the decomposition it was assumed that the mean position of the aerostat relative to the wind was inline with the mean wind direction. This is reasonable because the symmetrical and streamlined shape of the aerostat and the resulting drag will naturally cause the aerostat to position itself downstream of the winch, inline with the wind. The mean heading of the aerostat obtained from the tilt sensor was not used because the heading data is not as precise or as accurate as the GPS position data, due to its reliance on magnetometer measurements. The mean wind direction measured by the wind sensors was also not used because of its location far from the aerostat. In general, the mean given by the wind sensors, the GPS, and the tilt sensor were with +/- 15 degrees of each other.

Figure 3.1 shows the rotation of the GPS coordinate system so that the x-axis is inline with the mean wind direction. The angle of the aerostat's mean position is given by:

$$\beta = \tan^{-1}\left(\frac{y_t}{x_t}\right) + \pi \tag{3.1}$$

Where x_t is the true-east position and y_t is the true-north position. To rotate the axes so that the x is in line with the wind, the position vector was rotated by β.

$$\begin{bmatrix} x \\ y \\ z \end{bmatrix} = \begin{bmatrix} \cos\beta & \sin\beta & 0 \\ -\sin\beta & \cos\beta & 0 \\ 0 & 0 & 1 \end{bmatrix} \begin{bmatrix} x_t \\ y_t \\ z_t \end{bmatrix} \tag{3.2}$$

Where x, y, and z are the rotated components of the position.

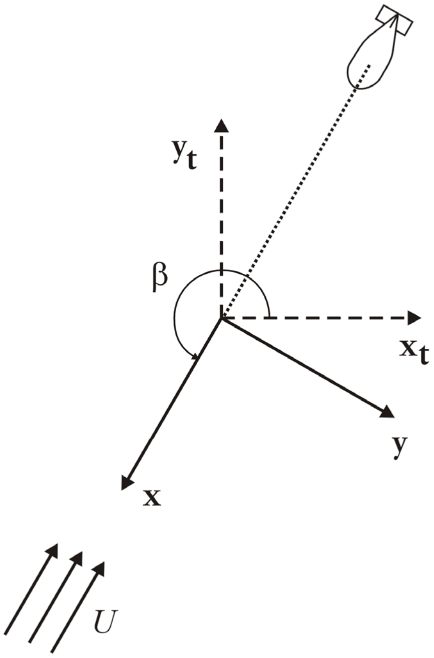

Figure 3.1 – Top view of the rotation of the GPS coordinate system (y_t, x_t) to be in line with the mean aerostat's position and wind direction.

The final step in the coordinate transformation was to calculate the vector from the winch to the aerostat GPS. This was performed by making a simple vector summation:

$$\vec{r}_{a/w} = \vec{r}_{a/b} - \vec{r}_{w/b} \tag{3.3}$$

Figure 3.2 shows the layout of the vectors in the experimental system. The winch and base station were installed in the same location for every flight. The $\vec{r}_{w/b}$ vector from the base station to the winch was determined by surveying the winch and base station locations using the DGPS system.

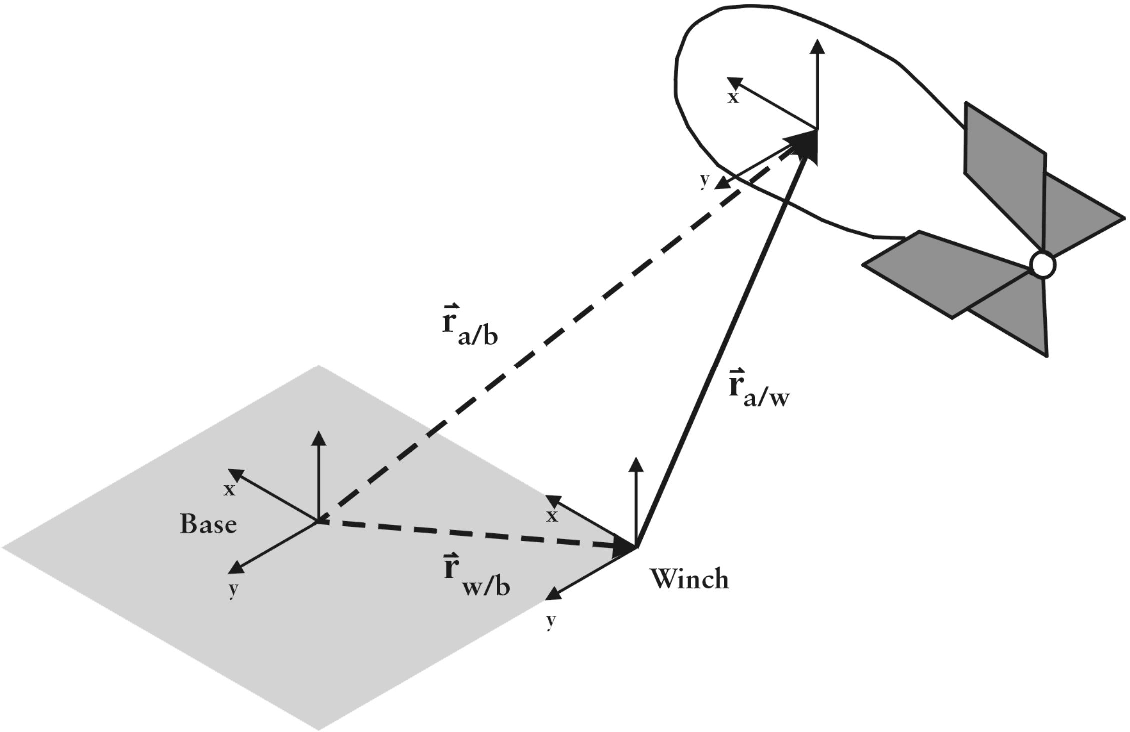

Figure 3.2 - Diagram showing the vector layout of the aerostat and base station system

The final result of the post-processing gave a vector from the winch to the aerostat's GPS expressed in a coordinate system in which the *x*-axis is in line with the mean wind speed and the *z*-axis is vertical.

3.1.2 Wind Extrapolation

The wind speed was measured by three wind sensors at 2.6 m, 6.1 m and 9.7 m above the ground. The wind speed at the aerostat's height was extrapolated from this data by using a power law given by:

$$\overline{U}_z = \overline{U}_{ref}\left(\frac{z}{z_{ref}}\right)^m \tag{3.4}$$

Where $\overline{U}_z$ is the mean wind speed at a height z, $\overline{U}_{ref}$ is the mean reference wind speed taken at z_{ref} = 9.7 m, and m is the power law exponent which varies as a function of the surface roughness [11].

For each flight day, the mean wind speed of the 2.6 m and the 9.7 m sensors were used to calculate the wind power law exponent m. The middle 6.1 m sensor is redundant; however it was used to validate the calculated exponent. Figure 3.3 shows a segment of the wind data recorded by the 2.6 m sensor and the 9.7 m sensor along with the means for both of these measurements on August 23rd, 2006.

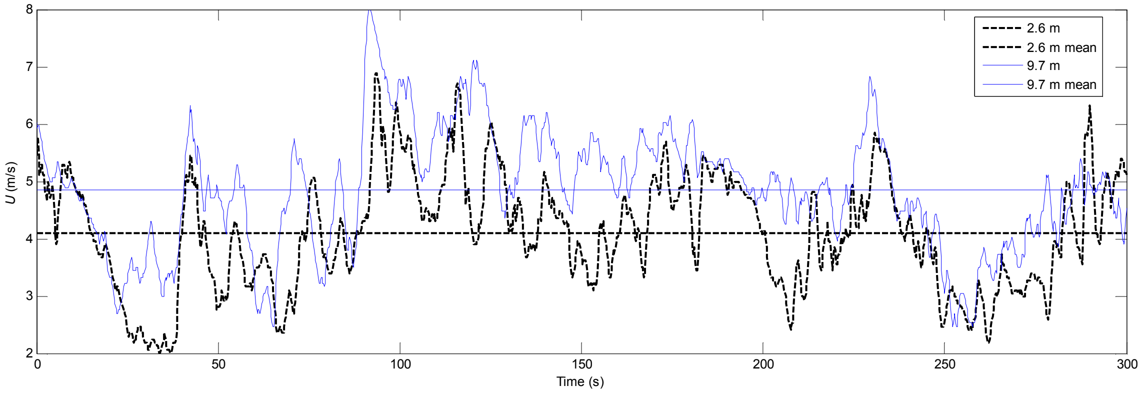

Figure 3.3 - Experimental wind measured at the 2.6 m tower and the 9.7 m tower, August 23rd, 2006

The mean wind speed values were used in equation (3.4) to calculate the power law exponent m. For the flight segment shown in Figure 3.3, the mean wind speeds were 4.10 m/s for the 2.6 m tower and 4.85 m/s for the 9.7 m tower, giving a power law-exponent m = 0.13. Figure 3.4 plots the experimental mean wind speeds for this segment along with the power law equation. This shows that the mean wind speed measured at the 6.1 m tower fits well with the power law.

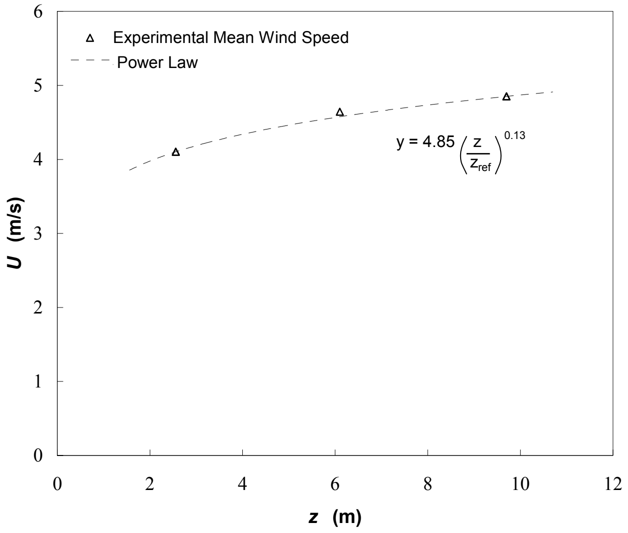

Figure 3.4 - Power law fit to the experimental data shown in Figure 3.3

The power law of equation (3.4) was also used to extrapolate the mean wind speed at the aerostat's average height, as determined by the GPS measurements.

3.1.3 Sonic Anemometer Data

To validate the wind data obtained from the Young sensors and to obtain information about the vertical wind gusts, a sonic anemometer was used to measure the three dimensional wind speeds on July 19th, 2006. The sonic anemometer was mounted on a tower 3 m above the ground, approximately 10 m from the 2.6 m high Young sensor. Table 5 gives the mean wind speeds and directions measured by both sensors along with the turbulence in the *u*, *v*, and *w* directions. The wind turbulence is defined as the standard deviation of the wind speed in the specified direction, divided by the mean overall wind speed.

Table 5 - Mean wind speed, mean direction data, and turbulence measured by the Young sensor and the Sonic Anemometer on July 19th, 2006.

	$\overline{U}_{3m}$ (m/s)	$\overline{\theta}_w$ (deg)	$\frac{\sigma_u}{\overline{U}_{3m}}$	$\frac{\sigma_v}{\overline{U}_{3m}}$	$\frac{\sigma_w}{\overline{U}_{3m}}$
Young	2.2	132.9	0.33	0.44	N/A
Sonic	2.3	133.3	0.34	0.47	0.15

Considering that the two sensors were spaced some distance apart, the similarity between the measurements made by each sensor is good. Note that the Young sensor only operates in the horizontal plane and provides no information about the vertical wind turbulence. The Young sensor may underestimate the wind turbulence due to its inertia causing a low pass filtering of the highest frequency components as discussed in Section 2.3.4.

Figure 3.5 shows the time histories of the wind speed recorded by each sensor. The first figure is the Young sensor data, recorded at 5 Hz. The second figure presents the data recorded during the same interval recorded at 10 Hz using the sonic anemometer. Because the sensors are located 10 m apart, they did not record the exact same wind field and therefore it is not possible to make direct comparisons between the two time histories. However, considering that distance, they show a strong similarity. As expected, the sonic anemometer shows a higher frequency content in the wind. This is due to the low-pass filter characteristics and the lower sampling rate of the Young sensor.

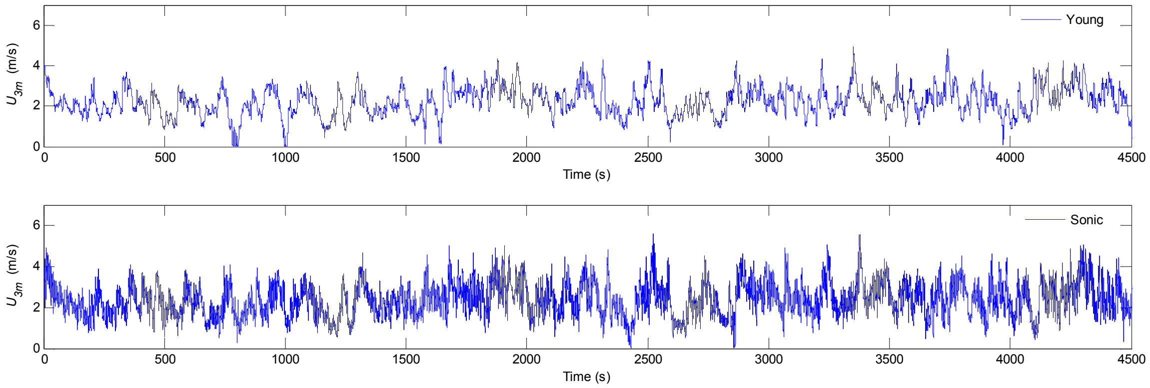

Figure 3.5 - Horizontal wind speed measured on July 19th, 2006. The first figure is the Young sensor mounted at 2.6 m above the ground. The second plot is the wind speed measured by the Sonic Anemometer mounted 10 m from the Young sensor at a height of 3 m.

Figure 3.6 shows the wind direction recorded by both sensors. The first plot is the direction data recorded by the Young sensor at 0.2 Hz. The second plot is from the sonic anemometer which was recorded at 10 Hz. The differences between the two plots are similar to the differences between the wind speed plots. Again, they are due to the low-pass filter characteristics and the lower sampling rate of the Young sensor.

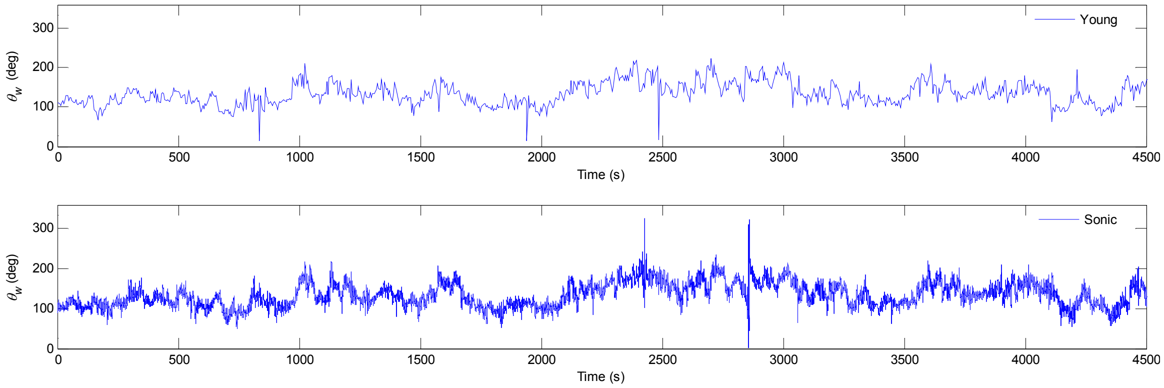

Figure 3.6 - Horizontal wind direction measured on July 19th, 2006. The first figure is the Young sensor mounted at 2.6 m above the ground. The second plot is the wind direction measured by the Sonic Anemometer mounted 10 m from the Young sensor at a height of 3 m.

The Young sensor only records the wind-speed and direction in the horizontal plane. The sonic anemometer records the three dimensional wind speeds and the vertical speed data recorded on July 19th, 2006 is shown in Figure 3.7.

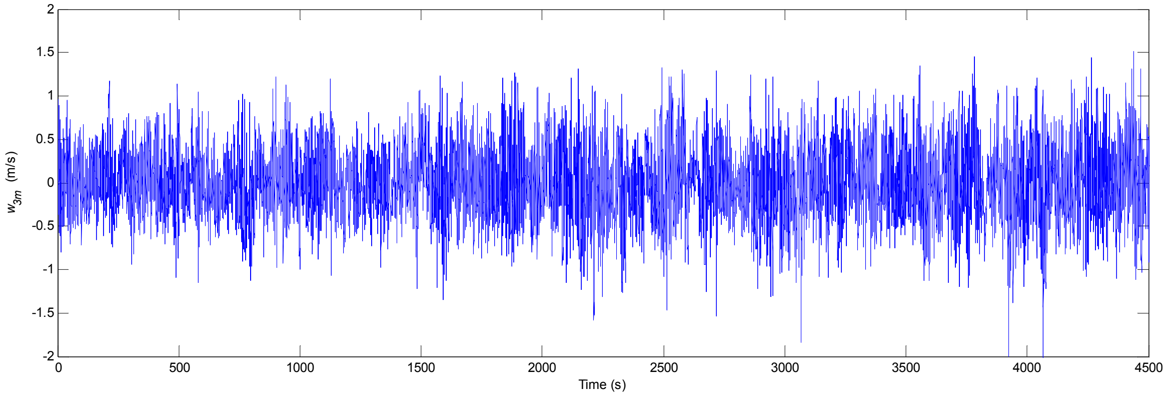

Figure 3.7 - Vertical wind gusts measured by the Sonic Anemometer on July 19th, 2006. The sensor was mounted approximately 3 m off the ground.

As expected, the mean vertical wind speed was 0 m/s; however there are vertical gusts in excess of 1 m/s. The mean wind speed in the horizontal plane at the same time was 2.3 m/s. This data indicates that the vertical wind gusts are significant relative to the horizontal component of the wind. Unfortunately, we only have data from a single day for the vertical wind speeds, but it still provides some valuable insight to the magnitude of the vertical wind gusts.

3.2 Experimental Results

An extensive flight test program was performed between July and October 2006 at the Lods Agronomy research facility at the west end of the Island of Montreal. Initial trial flights were performed without instrumentation and these progressed to fully instrumented and controlled flights. Nine flights with complete instrumentation were used for analysis and these are shown in Table 6. These included both controlled and uncontrolled periods of flight.

Table 6 – Flights used for analysis

Flight	Date (dd/mm/yy)	Temperature (^oC)	Inflation Pressure (inch-H_2O)	$\overline{F}_{lo}$ (N)	$\overline{U}_{ref}$ (m/s)	m
1	17/07/06	32	4.0	N/A	3.5	0.14
2	19/07/06	30	4.0	N/A	2.8	0.18
3	23/08/06	25	4.0	192.1	5.1	0.16
4	25/08/06	19	4.0	194.0	3.8	0.11
5	08/09/06	30	2.6	185.2	4.6	0.14
6	11/09/06	18	2.6	209.7	3.3	0.15
7	12/09/06	20	2.6	202.9	1.9	0.14
8	02/10/06	15	2.6	207.8	1.0	0.15
9	05/10/06	12	2.6	207.8	2.1	0.13

On August 25th, the aerostat suffered a complete envelope failure while being put into its garage. However, the aerostat was repaired quickly after this accident; and the standard inflation pressure was revised from 4.0 to 2.6 inch-H_2O.

3.2.1 Aerodynamic forces

When the aerostat is airborne, it is subject to two main categories of forces:

1. Free-lift forces: The buoyant forces of the aerostat and the gravitational force. The free-lift is the difference between the weight of the aerostat and the buoyancy force caused by the air displaced by the aerostat.
2. Aerodynamic forces: The forces caused by the wind speed. They are typically decomposed into lift and drag forces and are dependent on the wind speed.

While airborne, the tension in the main tether is equal to a summation of the free-lift forces and the aerodynamic forces. The free-lift forces can be determined either analytically by calculating the displacement volume of the aerostat, or experimentally by measuring the free lift of the aerostat. The proportion of the tension in the main tether due to the aerodynamic lift and drag can be expressed as:

$$X_A = \frac{\overline{F}_l - \overline{F}_{lo}}{\overline{F}_{lo}} \tag{3.5}$$

Where X_A is the proportion of the force, $\overline{F_l}$ is the mean tension in the tether during a flight, and $\overline{F_{lo}}$ is the free-lift of the aerostat. During the experimental testing, the free-lift of the aerostat was measured before the flight and after the flight while the balloon was in storage. The mean of the before and after measurements was used as the mean free-lift. Figure 3.8 plots the proportion of the forces due to aerodynamic lift and drag for various wind speeds. Not all the flights were included because measurements were not available for every day.

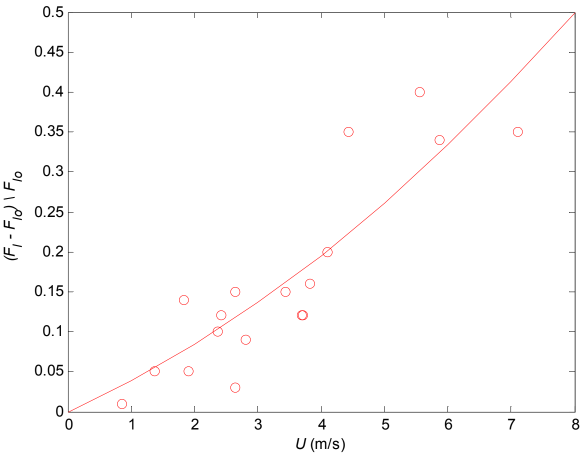

Figure 3.8 - Proportion of the forces on the aerostat caused by the aerodynamic lift and drag

The aerodynamic forces add between 2% to 40% to the free lift force of the aerostat. The aerodynamic forces also increase with the square of the wind speed which is logical because both the aerodynamic lift and drag forces are proportional to the square of the wind speed.

3.2.2 Comparison between Flights

The flights shown in Table 6 include a range of mean wind speeds from 1.0 m/s to 5.1 m/s. Each of these flights was divided into smaller five minute segments, tabulated in Table 7. This allowed a more precise estimate of the wind properties to be made than if a full flight (20 - 90 minutes) was used.

The mean wind speed alone is not adequate to describe the wind conditions during a particular segment. Figure 3.9 shows the peak gusts and the turbulence intensity for each segment from the nine flights. There is a large scatter in each of these plots. For example, at a mean wind speed of approximately 1.6 m/s, the peak gust in a five minute segment can be as much as three times the mean value, or as low as 1.4 times the mean value. This is due to the type of atmospheric conditions on a given day. When the weather is ‘unsettled’, large variations in the gusts tend to occur. This variability between flights and flight segments makes direct comparisons of flight results difficult.

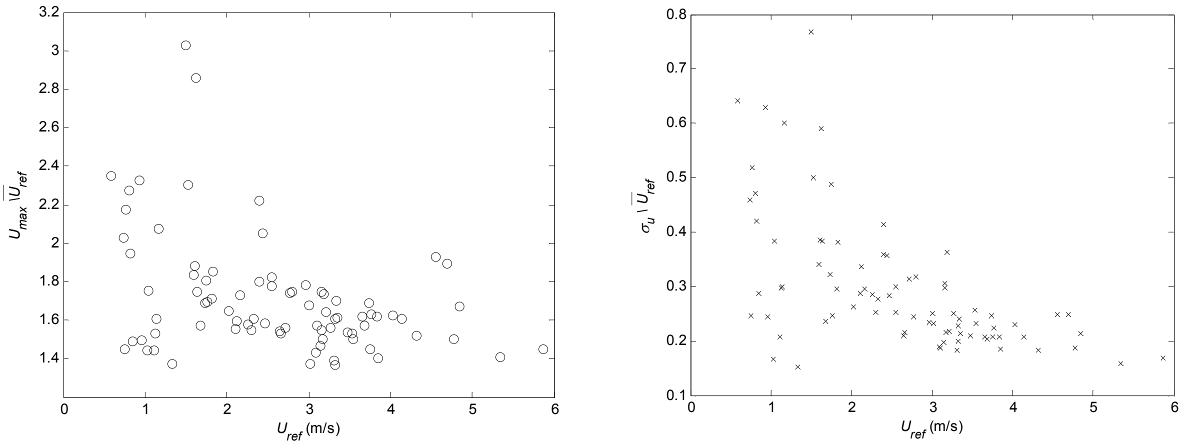

Figure 3.9 - Peak wind gusts at the aerostat’s altitude and the measured turbulence intensity at the top tower for various 5 minute means (including wind data from controlled and uncontrolled flight segments)

The wind sensors used in this experiment only measure the wind speed in the *x-y* plane. For the majority of flights the *z*-direction wind speed is unknown. However, as shown previously (3.1.3 Sonic Anemometer Data), the vertical gust component can be considerable, and would likely be a significant determinant of the aerostat’s motion.

When comparing the results from different flight segments, the mean wind speed extrapolated to the aerostat’s altitude was chosen. While this is a logical standard to use, it ignores the turbulence of the wind and the vertical gust intensities. Both of these have a large impact on the aerostat’s dynamics [9].

3.2.3 Uncontrolled results

The purpose of our tests is to evaluate the effectiveness of using the horizontal tailfins to control the aerostat's behaviour. To provide a baseline for statistical comparison, the aerostat was flown without the control system active. In this mode, the control surfaces were locked in the horizontal position. Figure 3.10 shows the data for an uncontrolled five minute segment from the August 23rd flight (# 9 in Table 7). The mean wind speed was 4.9 m/s; however the wind speed ranges from 3m/s to 8m/s during the segment. The pitch angle has perturbations about its mean greater than +/- 20 degrees. Large perturbations of as much as 20 m are also seen in the position variables.

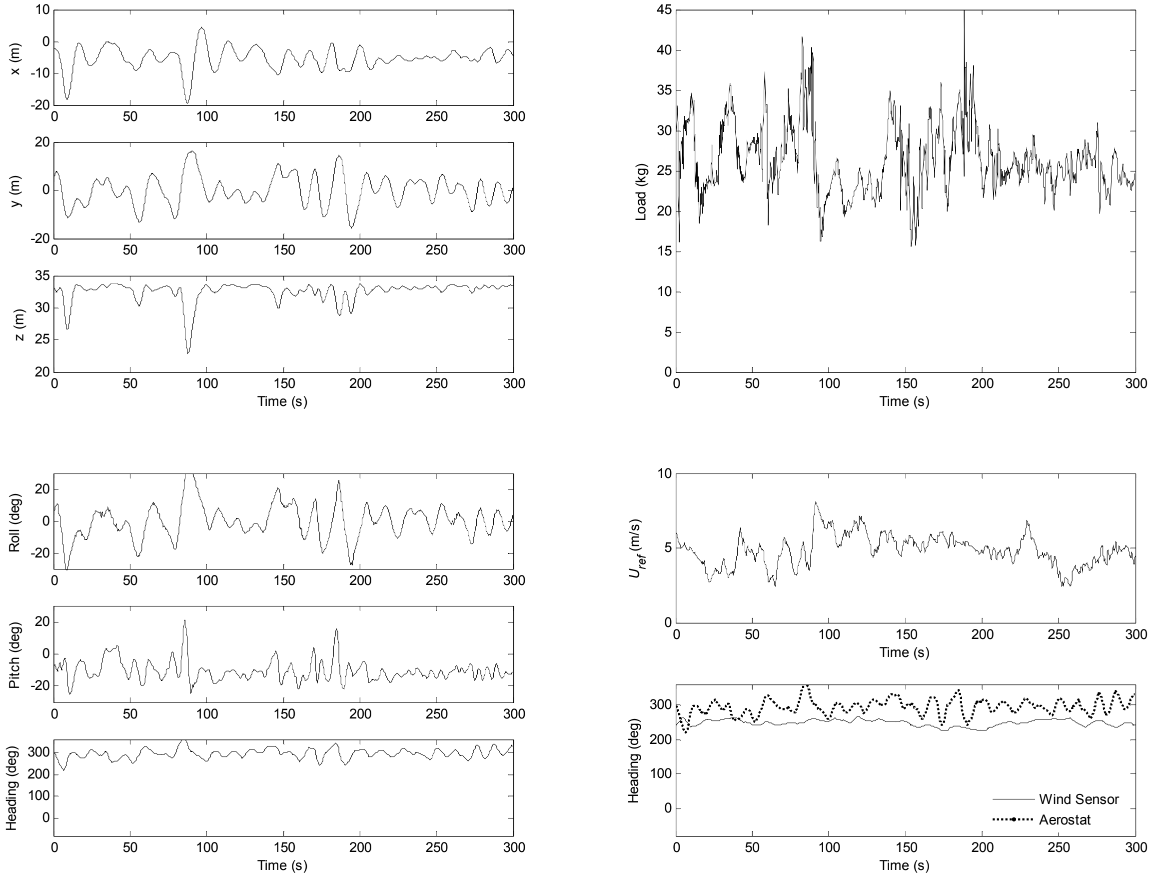

Figure 3.10 - Flight data for a segment of the August 23rd uncontrolled flight

Close examination of Figure 3.10 shows how wind events can affect the aerostat's motion and how the measured motion and load variables of the aerostat are related. At approximately 80 seconds, there is a large increase in the wind speed. This increase is reflected in the measured load and there are also corresponding changes in the *x* position, *y* position, *z* position, pitch, and roll. The aerostat responds to the increase in wind by moving back in the *x* direction and with an increase (nose down) in pitch and a dramatic downward motion. The aerostat also moves dramatically to the right, and there is a large increase in the roll (right wing down). This is likely because the aerostat is not aligned with the wind gust. This can be seen by comparing the heading of the aerostat with the measured heading of the wind shown in Figure 3.10. Note that the wind sensors are located approximately 50 m from the aerostat and they have a low sampling rate (0.2 Hz) which makes direct time and heading correlation difficult. The side wind gust coupled with the rapid increase in the wind speed cause the aerostat to move in the *x* and *y* directions as well as a large change in the pitch and in the roll. A second set of data at a milder wind-speed is shown in Appendix A.

Table 7 presents the mean values and standard deviations for the position variables and rotation variables as well as the load and the wind speed for each uncontrolled flight segment. In general, the standard deviation of each variable increases with increasing wind speed. For example, Figure 3.11 shows the standard deviation of the position variables for increasing wind speed. The linear trend lines show that the standard deviation increases in general with increasing wind speed; however, there is significant scatter in the data which is most likely explained by the variation in turbulence intensity and wind gusts. For example, the standard deviations for all three of the circled position variables of the segment at 1.63 m/s (#24 in Table 7) are larger than their respective trend lines. Examining the wind-turbulence and gust intensity plots (Figure 3.9), shows that the turbulence and wind gust intensity for this segment is far outside of the normal range. It is interesting to note that the motion perturbations are largest in the lateral (*y*) direction and least in the vertical (*z*) direction. This is largely because the lateral motion is the least constrained (by the tether and the wind), while the vertical motion is the most constrained (mainly by the tether).

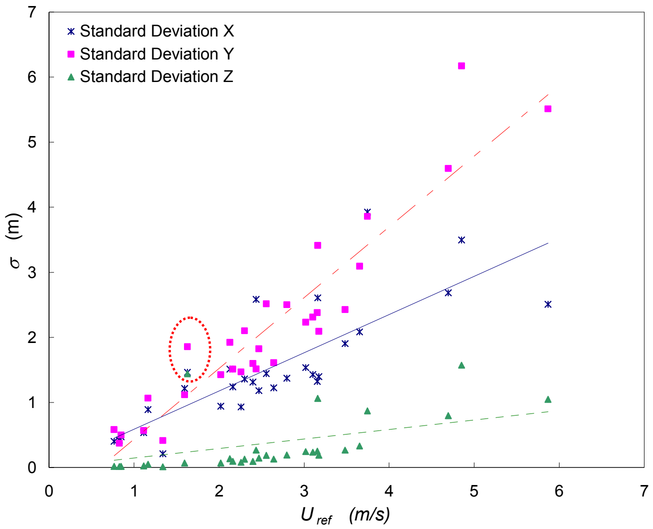

Figure 3.11 - Standard deviation of the position of the aerostat during different flight segments, with three variables at 1.63 m/s circled.

When conclusions are drawn using comparisons plotted against the mean wind speed, they must be weighted by considering that the vertical wind gusts, turbulence of the wind, and the gust intensities are ignored in such a plot.

Table 7 - Uncontrolled flight data for all flights separated into five minute segments

Date	#	$\overline{U}_{ref}$ (m/s)	$\frac{\sigma_U}{\overline{U}_{ref}}$	$\overline{F}_l$ (N)	σ_{F_l} (N)	$\bar{x}$ (m)	σ_x (m)	σ_y (m)	σ_z (m)	$\overline{\theta}$ (m)	σ_ϕ (deg)	σ_θ (deg)	σ_ψ (deg)
17/07/2006	1	3.10	0.19	207.8	1.8	-3.7	1.4	2.3	0.2	-14.9	6.3	3.6	20.2
17/07/2006	2	3.48	0.21	227.4	2.3	-3.4	1.9	2.4	0.3	-10.9	6.6	4.4	39.9
19/07/2006	3	2.64	0.21	210.7	1.1	-2.2	1.2	1.6	0.1	-15.0	2.7	1.9	14.6
19/07/2006	4	2.16	0.23	200.9	1.1	-1.7	1.2	1.5	0.1	-15.5	2.7	1.6	18.1
19/07/2006	5	2.47	0.25	208.7	1.4	-1.6	1.2	1.8	0.1	-14.5	3.0	2.5	22.1
19/07/2006	6	3.02	0.28	219.5	1.7	-2.4	1.5	2.2	0.2	-12.8	4.0	2.5	26.2
19/07/2006	7	2.56	0.30	201.9	1.2	-1.8	1.4	2.5	0.2	-14.2	4.1	2.3	28.0
23/08/2006	8	5.87	0.17	258.7	3.8	-5.3	2.5	5.5	1.0	-10.2	8.8	5.3	21.5
23/08/2006	9	4.85	0.21	257.7	4.2	-5.3	3.5	6.2	1.6	-10.5	10.9	6.1	22.7
25/08/2006	10	3.65	0.21	233.2	1.9	-3.8	2.1	3.1	0.3	-11.6	5.9	2.9	20.9
08/09/2006	11	4.70	0.25	259.7	3.7	-4.0	2.7	4.6	0.8	-12.5	7.2	5.2	25.3
08/09/2006	12	3.74	0.25	249.9	3.3	-3.9	3.9	3.9	0.9	-11.8	8.1	5.5	35.3
11/09/2006	13	2.80	0.32	241.1	1.8	-3.1	1.4	2.5	0.2	-10.9	3.7	2.2	18.1
11/09/2006	14	3.16	0.30	244.0	1.8	-3.1	2.6	3.4	1.1	-11.6	5.2	3.0	20.3
12/09/2006	15	1.60	0.25	232.3	1.1	-1.6	1.2	1.1	0.1	-10.5	2.1	2.0	22.3
12/09/2006	16	2.30	0.34	234.2	1.7	-2.3	1.4	2.1	0.1	-11.1	3.3	2.4	25.7
12/09/2006	17	2.13	0.34	227.4	1.7	-0.9	1.5	1.9	0.1	-11.7	3.2	2.6	21.3
12/09/2006	18	2.44	0.36	N/A	N/A	-2.0	2.6	1.5	0.3	-11.6	3.8	2.6	36.0
02/10/2006	19	1.34	0.15	191.1	0.4	-2.3	0.2	0.4	0.0	-13.7	0.7	0.3	11.4
02/10/2006	20	0.77	0.21	190.1	0.8	-2.2	0.4	0.6	0.0	-13.2	1.0	0.8	14.5
02/10/2006	21	0.83	0.29	193.1	0.6	-2.2	0.4	0.4	0.0	-13.5	0.8	0.6	12.7
02/10/2006	22	0.85	0.42	195.0	0.6	-1.9	0.5	0.5	0.0	-13.3	1.0	0.6	13.6
02/10/2006	23	1.11	0.52	197.0	0.5	-2.2	0.5	0.6	0.0	-13.3	1.0	0.8	14.6
05/10/2006	24	1.63	0.22	217.6	1.4	-2.8	1.5	1.9	1.4	-10.7	3.1	2.0	16.2
05/10/2006	25	3.15	0.26	232.3	2.1	-3.4	1.3	2.4	0.3	-10.4	3.8	2.5	22.0
05/10/2006	26	2.40	0.29	226.4	1.6	-2.9	1.3	1.6	0.1	-10.2	2.6	2.0	19.0
05/10/2006	27	3.17	0.31	233.2	2.4	-3.4	1.4	2.1	0.2	-10.0	3.5	2.6	16.9
05/10/2006	28	2.26	0.36	214.6	1.4	-2.5	0.9	1.5	0.1	-11.2	2.6	1.5	14.1
05/10/2006	29	2.02	0.59	228.3	1.1	-2.9	0.9	1.4	0.1	-9.5	2.5	2.0	17.9
05/10/2006	30	1.16	0.60	218.5	1.2	-2.4	0.9	1.1	0.0	-10.5	1.7	1.5	31.3

3.2.4 Open Loop Results

In order to determine the effectiveness of the control surfaces, the open-loop response of the aerostat to a step change in the control surface deflection was studied. The aerostat was flown outdoors, multiple times, under turbulent wind conditions, at an altitude of 30 m. This makes analysis of the response of the aerostat to a control surface deflection difficult. Figure 3.12 shows the load, pitch angle, and *x*- and *z*-position responses of the aerostat to a neutral, positive, and a negative control surface deflection.

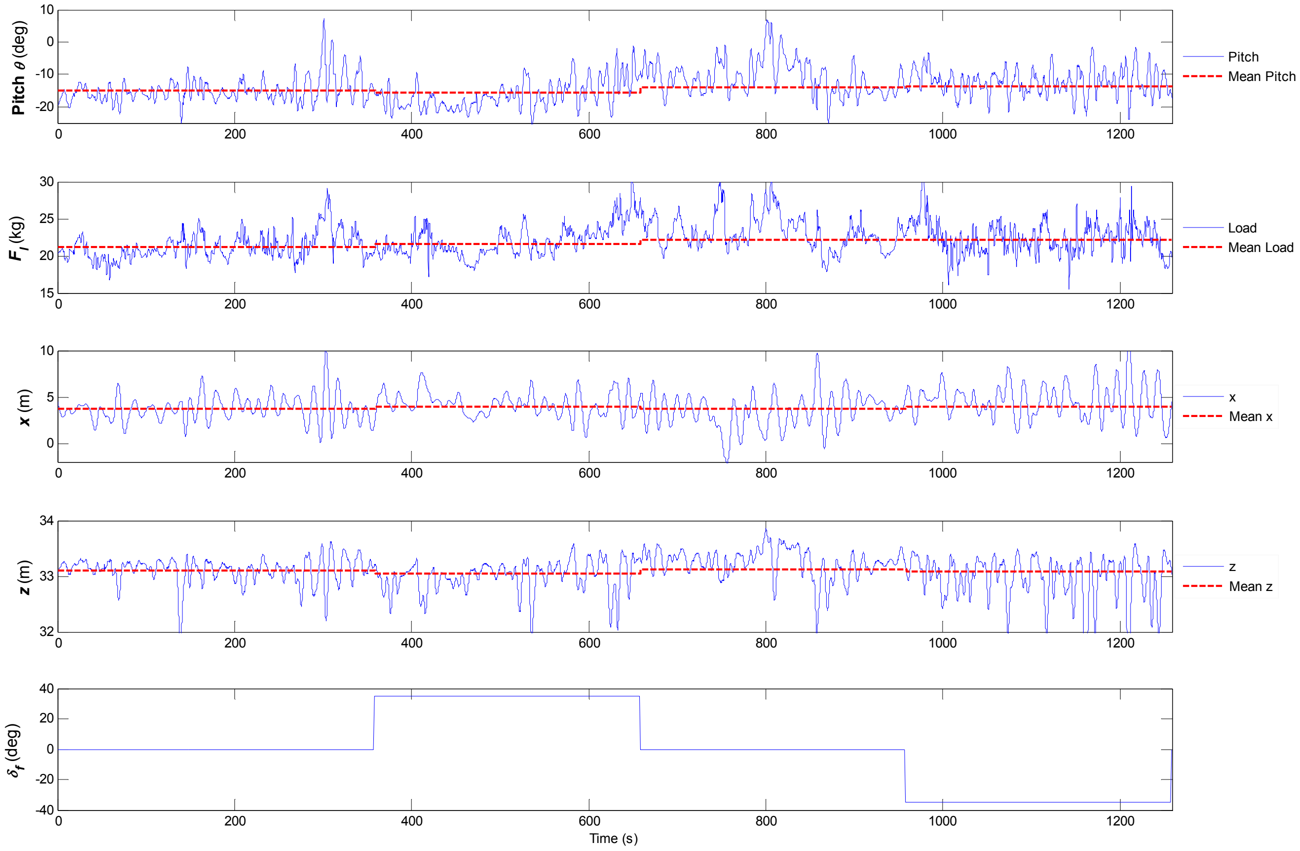

Figure 3.12 - Open loop pitch, load, and position, response of the aerostat to positive and negative step inputs of the control surface deflection during July 17th flight.

The effect of the wind turbulence dominates the response of the aerostat in all these variables making it difficult to perceive the effectiveness of the control surfaces. The mean values also shown in Figure 3.12 were calculated by averaging each variable over the period of each control surface deflection segment. This makes it possible to determine the effect that the control surfaces are having. Table 8 presents the mean pitch and mean load response of the aerostat averaged over the open-loop flights with different wind conditions. These averages represent flights with wind speed ranging from 2 to 3.5 m/s with variable turbulence intensity.

Table 8 - Mean pitch response to a step input control surface deflection

δ_f (deg)	$\bar{\theta}$ (deg)	$\bar{F}_l$ (kg)	$\bar{x}$ (m)	$\bar{z}$ (m)
0	-13.85	21.78	2.98	33.18
35	-16.52	21.70	3.56	33.08
-35	-12.48	21.93	3.53	33.07

A negative control surface deflection has the effect of changing the mean pitch of the aerostat by approximately -1.4 degrees and a positive deflection has an effect of +2.7 degrees. The effect on the load due to changing the control surface deflection is negligible.

Both the positive and negative control surface deflections cause the mean *x* position to increase by approximately 0.5 m. This is due to the increase in drag caused by the control surface deflection. The mean *z*-position of the aerostat decreases slightly for both deflections compared to the neutral control surface. This is related to the mean *x*-position. Because the tether length is constant, if the *x*-position increases, the *z*-position must decrease.

The results shown in Table 8 indicate that a controller intended to reduce the pitch perturbations might have the most promise.

3.2.5 Closed Loop Control

The results from the uncontrolled and open-loop tests were used to develop closed loop control of the aerostat using the horizontal control surfaces. The main focus was to reduce the pitch perturbations of the aerostat. Ranges of useful gains for a PID controller were determined and then tested experimentally. These were refined and iterated on until a satisfactory controller was achieved.

3.2.5.1 Pitch-Feedback Closed Loop Control Design

A control system to reduce pitch perturbations requires a set-point about which the perturbations are to be minimized. During a normal flight, while subject to wind turbulence, the pitch of the aerostat fluctuates about some mean. This mean is a function of the mean wind speed which varies with time. Figure 3.13 shows how the mean pitch varies with mean wind speed, at balloon altitude, using data extracted from uncontrolled flights.

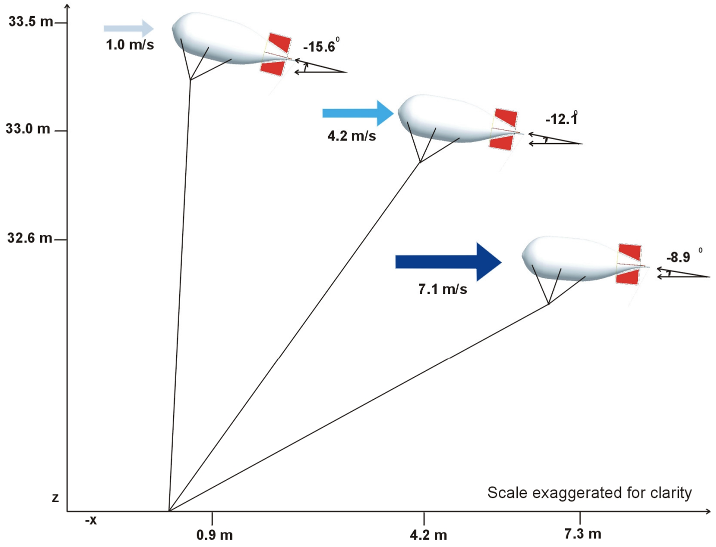

Figure 3.13 - Mean pitch of the aerostat as a function of the mean wind speed

The goal of the control system is to reduce the high frequency pitch perturbations which are caused by the turbulence, and not the low frequency change in the mean pitch, caused by the slowly changing mean wind speed. Because the mean pitch angle is changing as function of wind speed, it does not make sense to use a static set-point. Therefore, a method of determining a dynamic set-point was implemented.

One way to determine the mean pitch angle is to pass the measured pitch angle through a low-pass filter. Both finite response (FIR) and infinite response (IIR) filters [32] were tested to determine the best filter for implementation in the simulation and in the experimental control system. It was found that a first order IIR filter gave very satisfactory results and that similar performance could only be obtained with an FIR filter of much higher order.

The transfer function of a first order filter with time constant τ_f is given by:

$$\frac{\bar{\theta}(s)}{\theta(s)} = \frac{1}{1+\tau_f s} \tag{3.6}$$

Its IIR implementation in the time-domain can be written as:

$$\bar{\theta}_k = \eta\bar{\theta}_{k-1} + (1-\eta)\theta_k \tag{3.7}$$

Where $\bar{\theta}$ is the filtered signal, θ is the measured signal and η is given by:

$$\eta = \left(\frac{\tau_f}{\tau_f + T_s}\right) \tag{3.8}$$

Where T_S is the sampling time. At the break frequency, f_B, the magnitude of the filter's output is $1/\sqrt{2}$ times the magnitude of the input. The break-frequency is related to the time constant by:

$$f_B = \frac{1}{2\pi\tau_f} \tag{3.9}$$

A drawback of using a filtered set-point is that the output of the filter has a phase lag compared to the input. Figure 3.14 shows the magnitude and phase response of a first order IIR filter with a time constant of 20 seconds. Because we are only interested in preserving the low frequency content of the pitch, the performance of this filter is adequate.

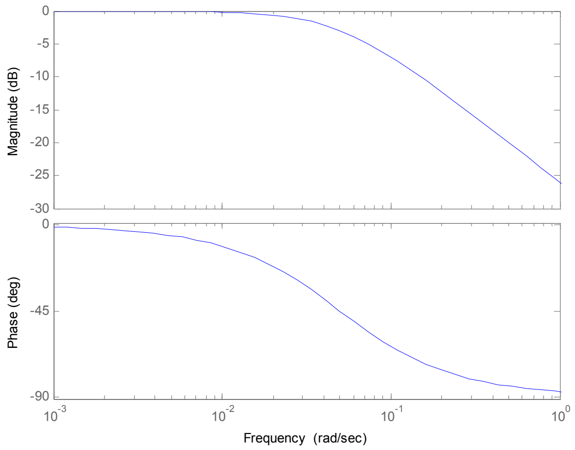

Figure 3.14 - Magnitude and phase plots for a first order IIR filter with a time constant of 20 seconds.

Figure 3.15 shows the experimental pitch response of the aerostat with control, along with a filtered set point using a time constant of 20 seconds. This figure shows how the set-point reacts to the changing mean. As predicted by Figure 3.14 there is a time lag in the response, however the effect is minor and should not affect the performance of the control system. The filtered pitch sufficiently approximates the slowly changing mean pitch.

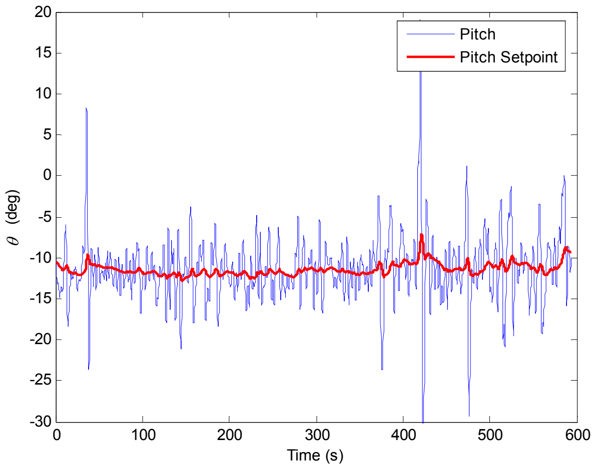

Figure 3.15 - Pitch and pitch set-point used to determine error for control system. The set-point was determined by filtering the pitch using a first order IIR filter with a time constant of 20s.

The difference between the filtered set point and the pitch was used as the error term for a PID controller of the form:

$$\delta_f = a(\delta_{servo}) = a\left(k_p e + k_d \dot{e} + k_i \int e dt\right) \tag{3.10}$$

Where δ_f is the control flap deflection, δ_{servo} is the command to the servo, e is the error term, and k_p, k_d and k_i are the proportional, derivative, and integral gains respectively. As outlined in Section 2.2.6, we know that the flap deflection is reduced by the factor *a,* estimated as 0.43, an average value from Figure 2.10.

In physical terms, the effect of the controller is to deflect the control surfaces to create lift on the tail which opposes the change in pitch. If the aerostat has a pitch less than the set-point (aerostat is nose up) then the error term is negative. This causes a negative control surface deflection (trailing edge down) which increases the lift on the tail, causing the aerostat to rotate nose down. This is shown in Figure 3.16.

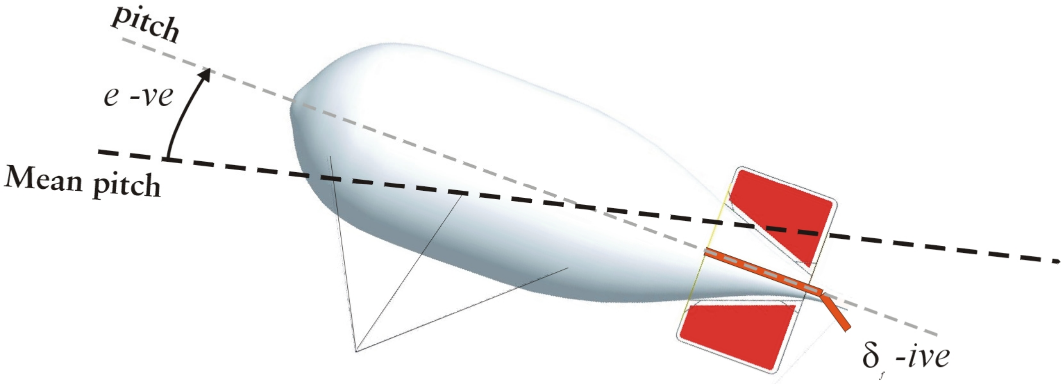

Figure 3.16 - Diagram showing the response of the pitch controller. In this scenario, the aerostat is pitching nose up, causing a negative error and a negative control surface deflection

3.2.6 Closed Loop Pitch Control Results

The PID controller was field tested with various gains. After each flight the results were analyzed and the gains were optimized through iteration. To judge the controller results, the standard deviation about the controller set-point was used. This is defined as:

$$\sigma_\theta = \sqrt{\frac{\sum_{i=1}^{N}\left(\theta_i - \bar{\theta}_i\right)^2}{N}} \tag{3.11}$$

Where σ_θ is the standard deviation about the set-point, θ_i is the pitch angle, $\overline{\theta_i}$ is the pitch set-point, and N is the number of samples during the period of interest.

Initial settings for the controller gains were estimated using pitch data from uncontrolled flights. From this data, the maximum and minimum useable gains were calculated. Initial flights with ranges of gains were performed to determine the best gains. The range of gains tested is presented in Table 9.

Table 9 - Range of gains used during experimental testing.

	k_p **(rad/deg)**	**k_d** **(rad s/deg)**	**k_i** **(rad/deg s)**
Range of gains tested	0.10 – 0.20	0.01 – 0.10	0.01 – 0.02

From these preliminary tests, four sets of gains shown in Table 10 were identified for further examination. These final control gains were determined by observing the response of the fins and also by analyzing the results of the initial flights. From the first tests it was found that only a small derivative gain could be used. A large derivative gain caused erratic behaviour in the fins, due to a number of factors including lag in the control system. From the initial tests it became apparent that the aerostat responded slowly to a control surface deflection, presumably due to its inertia. With a large derivative gain, the control surfaces moved too quickly for the aerostat to respond.

Table 10 – Final control gains used in testing

Controller	**k_p** **(rad/deg)**	**k_d** **(rad s/deg)**	**k_i** **(rad/deg s)**
P	0.20	0.00	0.00
PD	0.20	0.01	0.00
PI	0.20	0.00	0.01
PID	0.20	0.01	0.01

Figure 3.17 shows the initial results for controllers with various gains at different wind speeds. It should be noted that Figure 3.17 only compares σ_θ using the mean-wind speed at the balloon's height. As discussed earlier, this is not the only wind characteristic that should be taken into account when comparing controllers. From these initial results it was decided that a proportional controller gave the best performance.

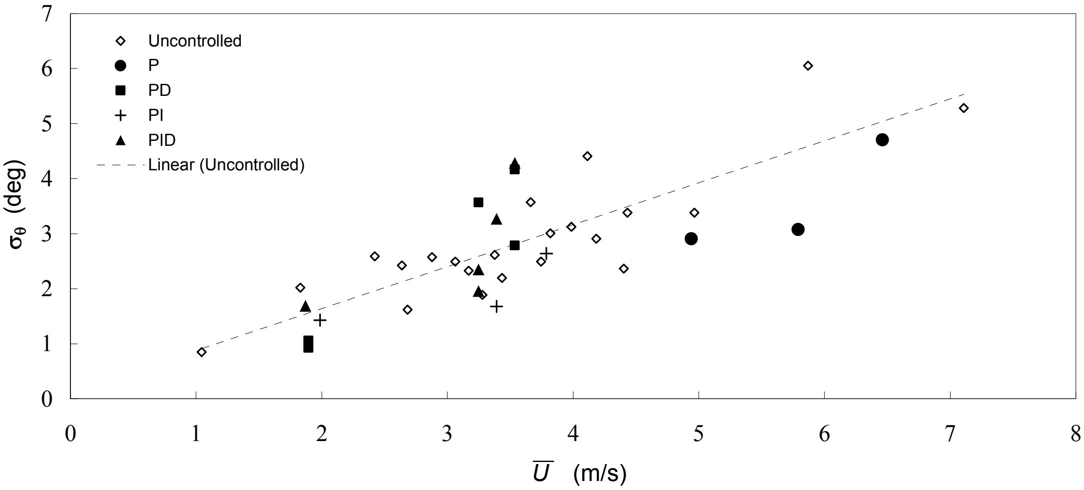

Figure 3.17 - Standard deviation of the pitch about the set-point for various initial controllers and for the uncontrolled flights

It was found that the integral term had little effect due, in part to the presence of the dynamic set-point. The integral term is intended to reduce the steady state error of the system; however, the implementation of a dynamic set-point in the control system eliminates the possibility of a steady state error. The dynamic set-point will adjust to match the mean pitch of the aerostat, which, by definition reduces the steady state error to zero.

Based on the results shown in Figure 3.17, further tests were performed using the P-controller from Table 10. Figure 3.18 shows the pitch response during a controlled segment of flight and an uncontrolled segment.

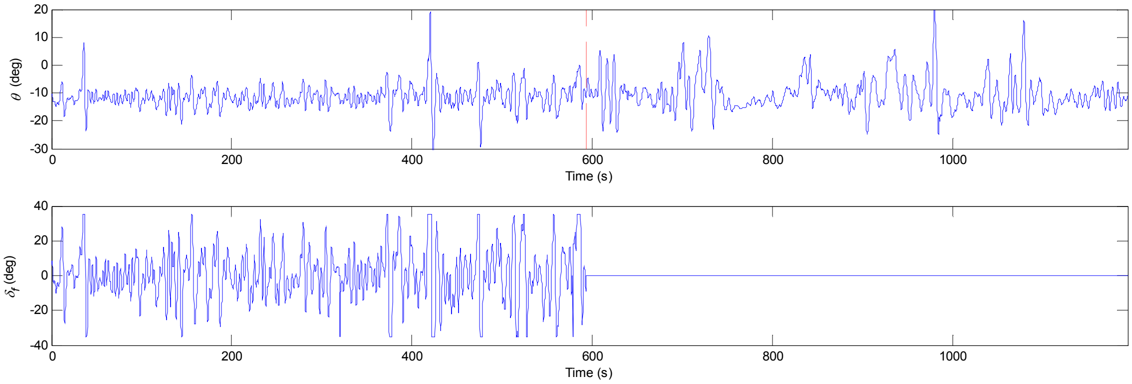

Figure 3.18 - Pitch response and fin deflection for a controlled and uncontrolled section of August 23rd flight with a mean wind speed of 5.1 m/s.

The effectiveness of the control system is apparent from Figure 3.18 as a reduction in the mid- and low-frequency pitch perturbation. The controller is not able to eliminate the large magnitude perturbations. This could be because these events are sometimes coupled with large position or roll perturbations. The controller may also be saturated during these events. The saturation of the controller can be seen at approximately 420 seconds in Figure 3.18 as plateaus in the control surface deflection plateaus because it has reached its maximum output.

Plotting the results in the frequency domain shows the effectiveness of the controller more clearly. Figure 3.19 shows the power spectral density (PSD) of the pitch angle for the two flight segments. The controller appears to be effectively reducing the pitch perturbations up to 0.2 Hz. That the control is not effective up to the 1Hz control bandwidth at which we found the servos could respond is likely due to the inertia of the aerostat. The lowest frequency perturbations are also not reduced because the dynamic set-point allows these changes to occur.

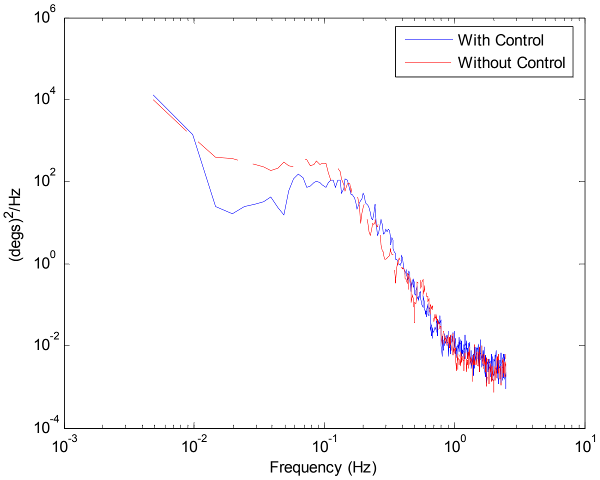

Figure 3.19 - PSD of a five minute segment of August 23rd flight with P-control and uncontrolled with a mean wind speed of 5.1 m/s.

The time history of a second P-controlled flight at a lower wind speed is shown in Figure 3.20. The controller reduces the low to mid frequency pitch perturbations but it is not as effective as the same controller at a higher wind speed as is apparent when comparing Figure 3.19 with Figure 3.21. This is most likely due to the decreased effectiveness of the control surfaces at lower wind speeds. Since the control surfaces derive their lift aerodynamically and the force they exert is proportional to the square of the wind speed, their effectiveness will be much reduced when the wind speed is low.

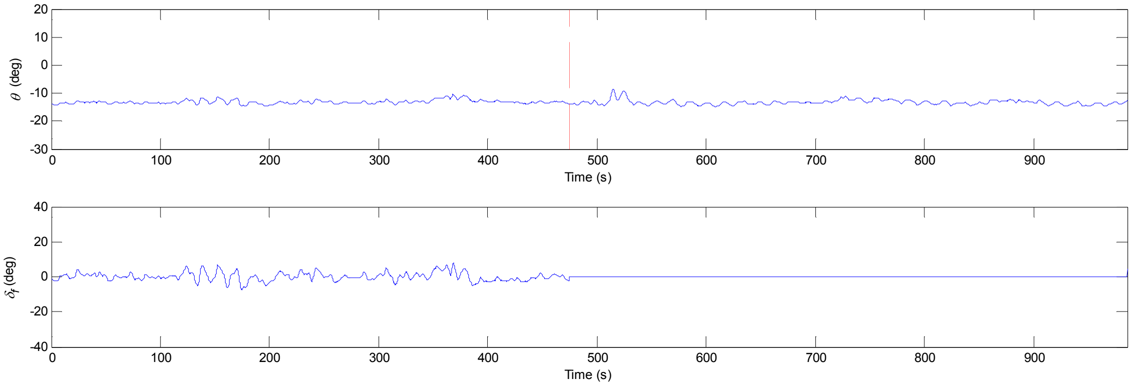

Figure 3.20 - Pitch response and fin deflection for a controlled and uncontrolled section of October 2nd flight with a mean wind speed of 1.0 m/s.

It is also apparent that the control surfaces are not being used to their full capability. Figure 3.20 also shows the control surface deflection which rarely exceeds 25% of its maximum capability ($\pm 35^0$). This suggests that a gain-scheduled controller in which gains are higher at lower wind speeds would improve performance at lower wind speeds. The gains could be selected to be inversely proportional to the mean wind speed so that the controller could take advantage of the maximum control surface deflection at all wind speeds.

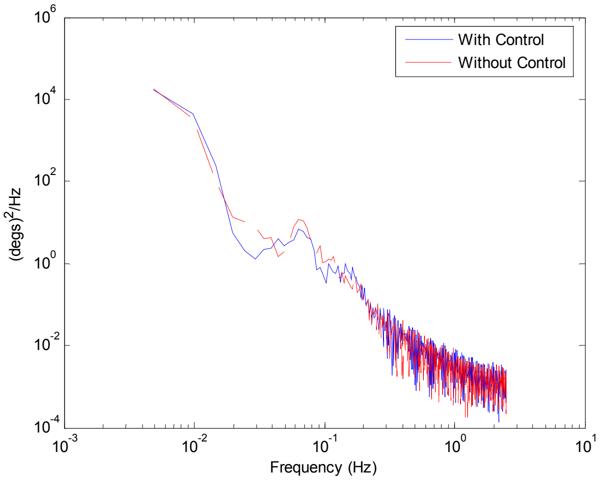

Figure 3.21 - PSD of a five minute segment of Oct 2nd flight with P-control and uncontrolled and a mean wind speed of 1.0 m/s.

Figure 3.22 shows the standard deviation about the set-point from multiple flights using the P-controller with a gain of 0.2 rad/deg over a variety of wind speeds. The linear-fit though the points shows a moderate improvement over the uncontrolled flight. This improvement appears to be proportional to wind speed. This is likely because the P-controller with a gain of 0.2 rad/deg does not take advantage of the full range of motion of the control surfaces at lower wind speeds.

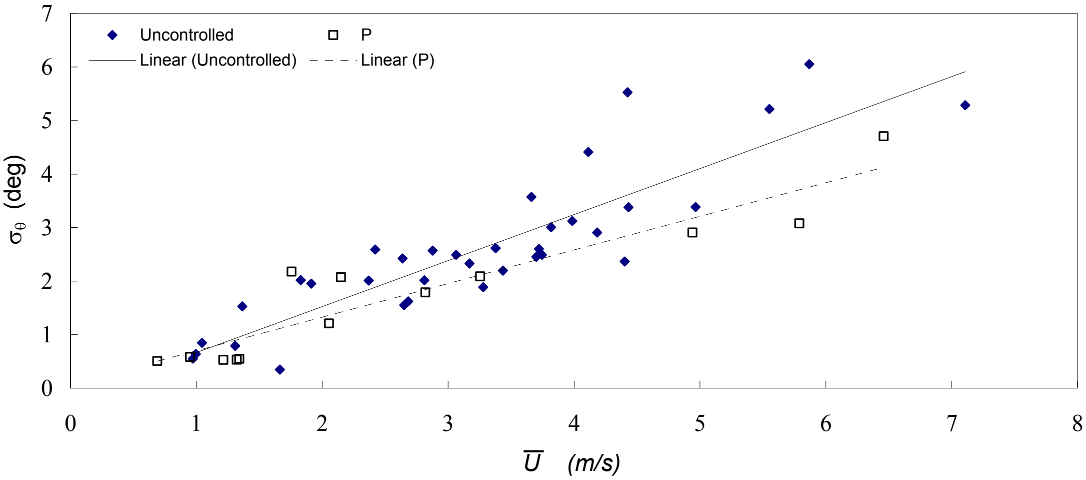

Figure 3.22 - Standard deviation of the pitch about the set-point for P-control compared to uncontrolled flight

It appears from Figure 3.22 that the effectiveness of the controller is inconsistent at certain wind speeds. This is evident in the 2 m/s range where a pair of P-controlled results appears outside their range of normal values. This is likely due to an unusually high level of turbulence for these segments compared to the uncontrolled segments. The controller may also not be as effective at lower wind speeds due to the reduced effectiveness of the control-surfaces at those speeds. Their effectiveness might also be improved if gain scheduling was incorporated into the control system.

Chapter 4 Simulation

This chapter presents the work done on a non-linear, dynamic simulation of the aerostat. The model used for this study is based on work done by Lambert [16] on a much larger streamlined aerostat. A description of the methods used to determine the various physical and aerodynamic parameters of the aerostat used in this study is given, as well as a series of improvements to the wind-model. Finally, a brief comparison between the results from simulated aerostat and the experimental aerostat is made.

4.1 Dynamics Model

The dynamics model used in the simulation was developed by Lambert [16] and originated from work done by Nahon [17]. Figure 4.1 shows a general schematic of the dynamic model used for the simulation. The aerostat is modelled as a single body at the end of a tether. The aerostat is subject to gravity, buoyancy, aerodynamic drag, and forces created by the tether. The tether is discretized into elements and the wind is modelled based on the statistical properties of experimentally measured wind.

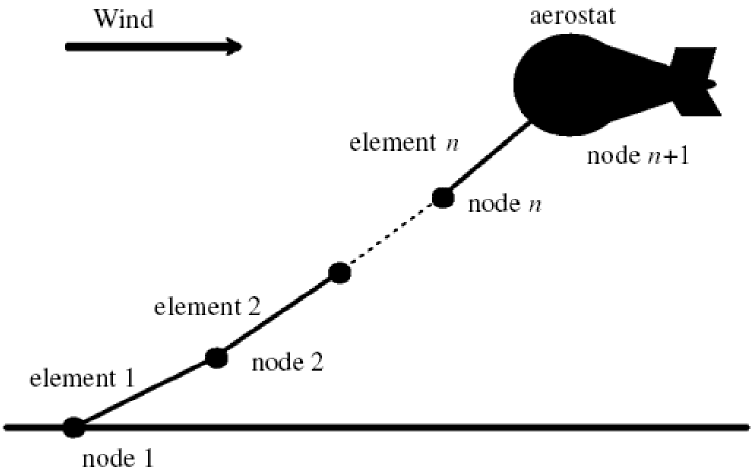

Figure 4.1 - Schematic of the dynamic model of the aerostat and tether system [33]

The aerostat is considered to be rigid and capable of motion with six degrees of freedom in three-dimensional space [33]. This section will give an overview of the theory behind the equations of motion, aerodynamics, and the tether model.

4.1.1 Aerostat Equations of Motion

In the simulation, the aerostat is considered as a rigid body. The translational equations of motion are derived from Newton's 2nd law:

$$\boldsymbol{F} = m\boldsymbol{a} \tag{4.1}$$

where $\boldsymbol{F}$ is the net force on the aerostat with respect to the inertial frame, m is the total mass of the aerostat, and $\boldsymbol{a}$ is the acceleration of the center of mass of the aerostat with respect to the inertial reference frame. It should be noted that the reference frames used in the present work used an upward-pointing z-axis, rather than the more usual downward-pointing axis used in standard aeronautical convention.

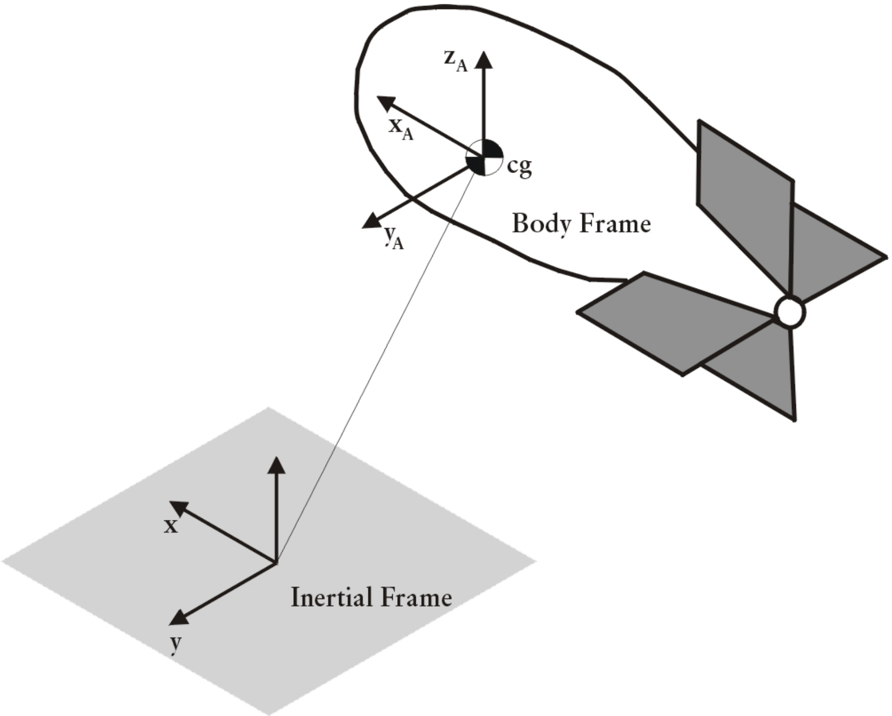

Figure 4.2 - Inertial and body-fixed coordinate frames for the aerostat system

It is most convenient to calculate the forces acting on the aerostat in a body-fixed frame (shown in Figure 4.2) and so it is easier to solve the equations of motion of the aerostat with respect to the body frame. Equation (4.1) can be written with respect to the aerostat's body frame as:

$$\boldsymbol{F} = m\left(\frac{\partial \boldsymbol{V_A}}{\partial t}\right) + \boldsymbol{\omega} \times \boldsymbol{V_A} \qquad (4.2)$$

where $\boldsymbol{V}_A = [u \quad v \quad w]^T$ is the velocity of the aerostat's center of mass, and $\boldsymbol{\omega} = [p \quad q \quad r]^T$ is the angular velocity of the aerostat. Both vectors are expressed as components in the body frame. The quantity $\frac{\partial \boldsymbol{V_A}}{\partial t}$ refers to the time derivative of $\boldsymbol{V_A}$, as seen in the body frame.

The rotational equations of motion are derived using Euler's equation:

$$\boldsymbol{M}_{cm} = \boldsymbol{I}_{cm}\dot{\boldsymbol{\omega}} + \boldsymbol{\omega} \times \boldsymbol{I}_{cm}\boldsymbol{\omega} \tag{4.3}$$

where $\boldsymbol{I}_{cm}$ is the inertia tensor about the center of mass, $\boldsymbol{M}_{cm}$ is the net moment acting about the aerostat's center of mass. The forces $\boldsymbol{F}$ and moments $\boldsymbol{M}_{cm}$ are the net forces and moments acting on the aerostat from the following sources:

- gravity
- buoyancy
- aerodynamic
- tether tension

Expanding equation (4.2) and separating into component form gives the three translational equations of motion:

$$\begin{gathered}
(mg - F_B)\sin\theta + F_{Hx} + F_{Px} + F_{Sx} + F_{Ux} + F_{Lx} + F_{Tx} = m_x(\dot{u} + qw - rv) \\
-(mg - F_B)\sin\phi\cos\theta + F_{Hy} + F_{Py} + F_{Sy} + F_{Uy} + F_{Ly} + F_{Tx} = m_y(\dot{v} + ru - pw) \qquad (4.4) \\
-(mg - F_B)\cos\phi\cos\theta + F_{Hz} + F_{Pz} + F_{Sz} + F_{Uz} + F_{Lz} + F_{Tx} = m_z(\dot{w} + pv - qu)
\end{gathered}$$

where:

F_H is the aerodynamic force on the hull,

F_P, F_S, F_U, and F_L, are the forces from the port, starboard, upper, and lower tails fins

F_T is the force due to the tether

F_B is the buoyant force of the aerostat

m_x, m_y, and m_z are the diagonal terms of the mass matrix

m is the total mass of the aerostat including the gases

ϕ, θ, and ψ are the roll, pitch and yaw of the aerostat [16]

Similarly, by expanding equation (4.3), and assuming that the aerostat has an *x-z* plane of symmetry, the three rotational equations of motion are given by:

$$
\begin{gathered}
-z_B F_B \sin\phi\cos\theta + M_{Hx} + M_{Px} + M_{Sx} + M_{Ux} + M_{Lx} + M_{Tx} = I_{xx}\dot{p} - \left(I_{yy} - I_{zz}\right)qr - I_{xz}\left(\dot{r} + pq\right) \\
-x_B F_B \cos\phi\cos\theta - z_B F_B \sin\theta + M_{Hy} + M_{Py} + M_{Sy} + M_{Uy} + M_{Ly} + M_{Ty} = \\
I_{yy}\dot{q} - \left(I_{zz} - I_{xx}\right)pr - I_{xz}\left(r^2 - p^2\right) \\
-x_B F_B \sin\phi\cos\theta + M_{Hz} + M_{Pz} + M_{Sz} + M_{Uz} + M_{Lz} + M_{Tz} = I_{zz}\dot{r} - \left(I_{xx} - I_{yy}\right)pq - I_{xz}\left(\dot{p} - qr\right)
\end{gathered}
\tag{4.5}
$$

where:

M_H is the aerodynamic moment on the hull,

M_P, M_S, M_U, and M_L, are the moments caused by the port, starboard, upper, and lower tails fins

M_T is the moment due to the tether

I_{xx}, I_{yy}, I_{zz}, and I_{xz}, are the moments and products of inertia ($I_{XY} = I_{YZ} = 0$)

x_B, and z_B are the positions of the aerostat's center of buoyancy in the x and z directions of the body frame (y_B is assumed to be zero)

Each of the forces and moments from equations (4.4) and (4.5) are calculated by breaking down the aerostat into individual components with known aerodynamic characteristics. This approach has been used previously and is detailed in [17] and [16]. In the present work, the aerostat is separated into the hull and four tail fins, and the aerodynamics forces and moments on each component are calculated.

4.1.2 Aerodynamics of the Hull

As presented in [16], the aerodynamic forces on the hull are based on work by Jones and Delaurier [13]. Jones and Delaurier developed equations for the lift, drag, and moment about the nose of an aerostat in steady flow. Considering only the terms pertaining to the aerodynamics of the hull of the aerostat, and ignoring the tail-fin terms, these equations are:

$$L_h = q_0\left[(k_3 - k_1)\eta_k I_1 \sin(2\alpha)\cos(\alpha/2) + (Cd_c)_h J_1 \sin\alpha \sin|\alpha|\right]$$

$$D_h = q_0\left[(Cd_c)_0 S_h \cos^2\alpha - (k_3 - k_1)\eta_k I_1 \sin(2\alpha)\cos(\alpha/2)\right] \tag{4.6}$$

$$M_{nose} = -q_0\left[(k_3 - k_1)\eta_k I_3 \sin(2\alpha)\cos(\alpha/2) + (Cd_c)_h J_2 \sin\alpha \sin|\alpha|\right]$$

where:

$q_0 = 1/2\rho V_A^2$ is the dynamic pressure

α is the angle of attack

k_1 and k_3 are the axial and lateral added mass coefficients

η_k is the hull efficiency factor

$(Cd_C)_h$ is the hull's cross flow drag coefficient

$(Cd_C)_0$ is the hull's zero-angle axial drag coefficient

S_h is the hull's reference area ($=V^{2/3}$ where V is the hull volume)

And the parameters I_1, I_3, J_1, and J_2 are based on the geometry of the body:

$$I_1 = \int_0^{l_h} \frac{dA}{d\xi} d\xi \qquad I_3 = \xi \int_0^{l_h} \frac{dA}{d\xi} d\xi$$

$$J_1 = \int_0^{l_h} 2r d\xi \qquad J_2 = \int_0^{l_h} 2r\xi d\xi \tag{4.7}$$

where:

A is the local cross-sectional area of the hull

ξ is the axial distance along the hull from the nose, shown in Figure 4.3

r is the local hull radius

l_h is the distance from the nose to the leading edge of the fins, shown in Figure 4.3

The values for I_1, I_3, J_1, and J_2, are determined from the geometry of the aerostat. The calculation of these terms is outlined in section 4.4.

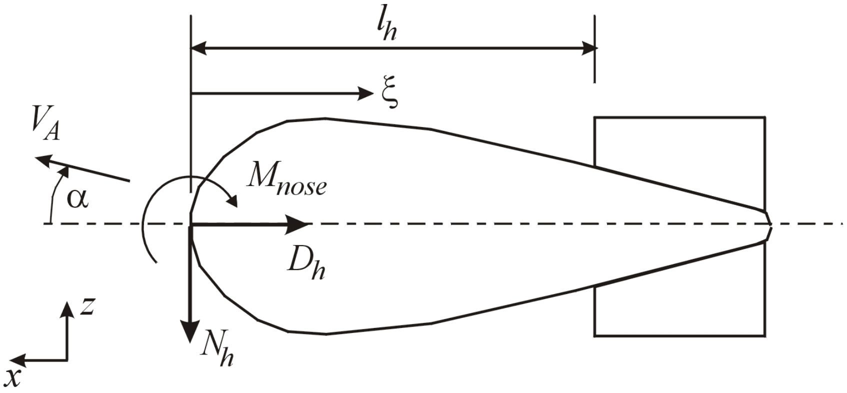

Figure 4.3 - Schematic of the aerostat with aerodynamic parameters

The pitch moment from equation (4.6) cannot be used directly in the equations of motion as it is calculated about the nose of the aerostat. To compensate for this, the lift force is applied at a distance from the nose to create the desired moment:

$$x_L = \frac{M_{nose}}{L_h} \tag{4.8}$$

4.1.3 Aerodynamics of the Tail Fins

The aerodynamic forces caused by the four tail fins are estimated using the standard aeronautical relationships for lift and drag:

$$L_i = \frac{1}{2}\rho A_f V_i^2 C_L$$
$$D_i = \frac{1}{2}\rho A_f V_i^2 C_D \tag{4.9}$$

where A_f is the planform area of the fin, and V_i is the local velocity of the fin. The center of pressure was taken at the quarter-chord and the span wise midpoint. The method of estimating lift and drag coefficients (C_L and C_D) is outlined in detail in section 4.4.2.

The four fins on the aerostat are configured in a cross shape, with two fins oriented horizontally (port and starboard) and two fins oriented vertically (upper and lower) as shown in Figure 4.4. The orientation of the drag calculated from equations (4.9) is identical for all four fins and is directed along the aerostat's *x*-axis. However, the lift calculated for the vertical fins is along the aerostat's *z*-direction, while the lift of the vertical fins is directed in the *y*-direction.

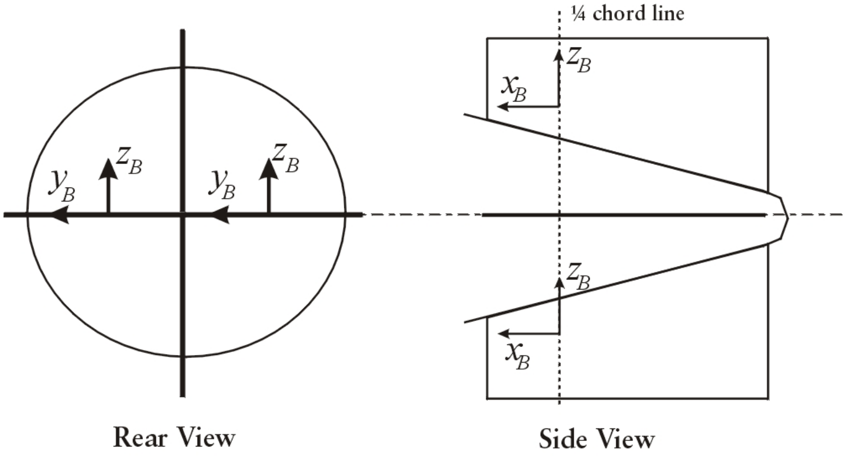

Figure 4.4 - Diagram showing the layout of the fin section of the aerostat from the rear and from the side

4.1.4 Tether Model

The simulation uses a lumped mass model for the tether where the tether is discretized into a series of elements with the mass of each element concentrated at its end nodes.

This model is described in detail in [16] and [18] and has been validated experimentally. Figure 4.5 shows how each element is modelled with a spring element and a damping element.

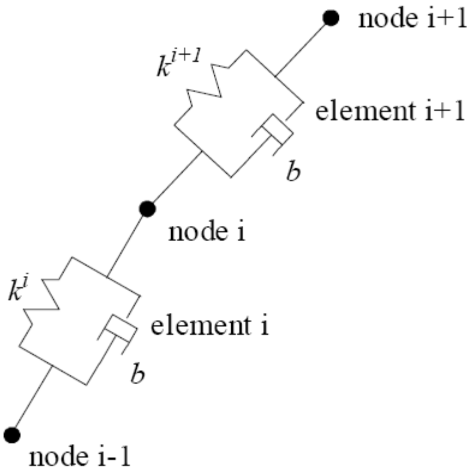

Figure 4.5 - Diagram of the lumped-mass discretization of the tether

The tether is considered to have negligible bending stiffness and torsion is not taken into account. The external forces on the tether are caused by gravity and aerodynamic drag. The equation of motion for a single node is given by:

$$\boldsymbol{F}_i = \frac{1}{2}(m_i + m_{i+1})\boldsymbol{a}_i \tag{4.10}$$

which can be expanded and written in vector form as:

$$\frac{1}{2}(m_i + m_{i+1})\boldsymbol{a}_i = \left(\boldsymbol{F}_{t(i+1)} + \boldsymbol{F}_{b(i+1)}\right) - \left(\boldsymbol{F}_{t(i)} + \boldsymbol{F}_{b(i)}\right) + \frac{1}{2}\left(\boldsymbol{F}_{d(i)} + \boldsymbol{F}_{d(i+1)} + m_i\boldsymbol{g} + m_{i+1}\boldsymbol{g}\right) \tag{4.11}$$

where:

i denotes the element

m_i is the mass of the i 'th tether element

$\boldsymbol{F_t}$ is the tension force

$\boldsymbol{F_b}$ is the damping force

$\boldsymbol{F_d}$ is the drag

$\boldsymbol{g}$ is the gravitational constant

The expansion of each of these forces is described in detail in [10].

4.2 Complete Dynamic System

The complete system consists of equations (4.4) and (4.5) for the aerostat combined with equations (4.11) for the tether nodes. This gives a system of 6 + 3n second-order, ordinary differential equations (ODEs) describing the translation and rotation of the aerostat and the tether nodes. These ODEs are resolved rewritten in first-order form, giving 12 + 6n ODEs for the acceleration and velocity of each node [10]. The ODEs are integrated at each time step using a fourth-order Runge-Kutta numerical integration routine giving the complete motion of the system. The number of nodes in the tether, n, is determined at run-time. It was typically found that for a tether length of 30 m, four nodes was a sufficient number to reasonably capture the tether profile.

In addition, two geometric constraints are applied to the system:

1. Node 0 of the tether is fixed to the ground. This is enforced by ensuring that the position and velocity of the first node are set to zero.
2. Node n is coincident with the confluence point. As the aerostat and its harness are considered as a single rigid body, it is possible to describe the motion of the confluence point with respect to the center of mass of the aerostat [11]:

$$\begin{aligned} \boldsymbol{r_{CP}} &= \boldsymbol{r_{CM}} + \boldsymbol{r_T} \\ \boldsymbol{V_{CP}} &= \boldsymbol{V_{CM}} + \boldsymbol{\omega} \times \boldsymbol{r_T} \end{aligned} \tag{4.12}$$

where

$\boldsymbol{r_{CP}}$ is the position of the confluence point
$\boldsymbol{r_{CM}}$ is the position of the center of mass
$\boldsymbol{V_{CP}}$ is the velocity of the confluence point
$\boldsymbol{V_{CM}}$ is the velocity of the center of mass
$\boldsymbol{r_T}$ is a vector from the center of mass to the confluence point

Both of the conditions are imposed during the integration at each time step.

4.3 Physical Parameters

The goal of the simulation was to replicate, as well as possible, the behaviour of the aerostat used experimentally. To reach this objective, an effort was made to accurately measure the geometric and mass properties of the physical aerostat. The shape of the inflated hull was measured and the mass of each component was weighed in the lab. From these measurements, a three-dimensional CAD model was created using Pro-Engineer. The CAD model gave an accurate estimate for the inertia properties of the aerostat as well as the center of buoyancy and mass.

4.3.1 Hull Geometric Measurements

In order to determine an accurate shape for the body, the hull was inflated and measured in a barn at the Lods research facility. A grid was set up on the floor and the balloon's profile was measured. The measured points were plotted, giving a profile of the actual balloon which is shown in Figure 4.6. A sixth order polynomial was fitted to these points giving a good approximation of the shape of the balloon. In addition to the profile, the positions of the six load-patches to which the flying harness was attached, were also measured.

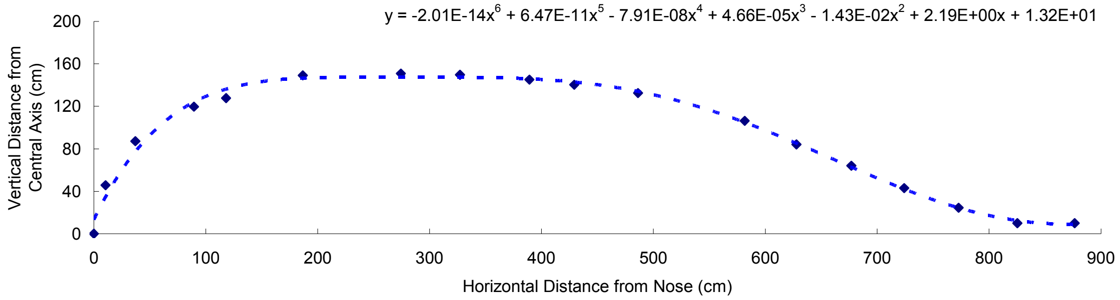

Figure 4.6 - Measured profile of the balloon with a sixth-order polynomial fit

The polynomial obtained from these measurements provided a method to create a CAD model of the hull and also provided an equation with a form suitable for use in the integrals of equations (4.7).

Table 11 - Length and mass measurements of the flying harness elements

Tether	Length (m)	Mass (kg)
Front	3.14	0.067
Middle	2.96	0.062
Rear	4.18	0.089

The masses and lengths of each of the flying harness tether elements were also measured (Table 11). The load-patch locations and tether lengths allowed for the confluence point of the six tethers to be determined accurately. Table 12 shows the location of the confluence point from a reference frame centered at nose of the aerostat

Table 12 - Confluence point position from reference frame centered at nose of the aerostat

x (m)	y (m)	z (m)
-2.14	0.00	-3.17

4.3.2 CAD model of TRF

Pro-Engineer Wildfire 2.0 was chosen as the CAD program to model the aerostat. It was selected because it has the ability to determine the mass and inertial properties of a 3-

dimensional model. The author and others ([16], [11]) have also successfully used the software to model other inflatable balloons.

The sixth-order polynomial shown in Figure 4.6 was used to create the main hull shape in Pro-Engineer. To model the tail, physical measurements of the tail fins were used. The balloon was initially modeled as a solid body to represent the Helium gas. This model was used to determine the center of buoyancy of the balloon (COB) and the moments of inertia of the Helium. The solid model was then converted to a shell with a finite thickness. This model was used to determine the center of mass (COM) of the balloon.

The smallest thickness that Pro-Engineer is capable of producing is 0.001m. This is significantly larger than the thickness of the nylon used to construct the balloon envelope (measured using digital calipers to be approximately 0.0001m). Because of the limits imposed by Pro-Engineer, the balloon was modeled with a shell thickness from 0.001m to 0.0012m.

A sample of nylon was measured and weighed to determine its density per unit area (0.1329 kg/m^2). To uniformly distribute the nylon material in the CAD model shell, the density per unit area was converted to a conventional density (per unit volume) using the thickness of the model shell. This ensures that the model maintains the same real density as the real aerostat. Further, because the shell thickness is trivial relative to the balloon dimensions (2.95 m diameter, 8.76 m length), using a shell thickness one order of magnitude larger than the true material thickness should have no appreciable impact on the validity of the calculated moments and products of inertia.

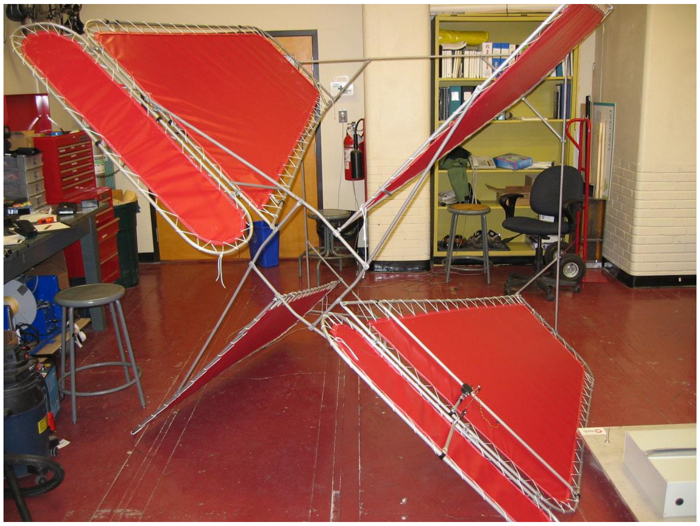

Figure 4.7 - Assembled tail section in the lab for measurements

The tail fins were measured in detail in the lab (Figure 4.7). They were constructed of hollow aluminium tubing with nylon covering. The aluminium tubing had an outside diameter of 1.27 cm and an inside diameter of 1.09 cm. Its mass properties were estimated using standard aluminium density of 2700 kg/m^3. The nylon covering used for the tail was thicker than the nylon used for the hull. The mass of each tail piece was known and the density of the nylon was estimated from this. The small strings used to attach the nylon pieces were not modelled but their mass is effectively included in the nylon's density.

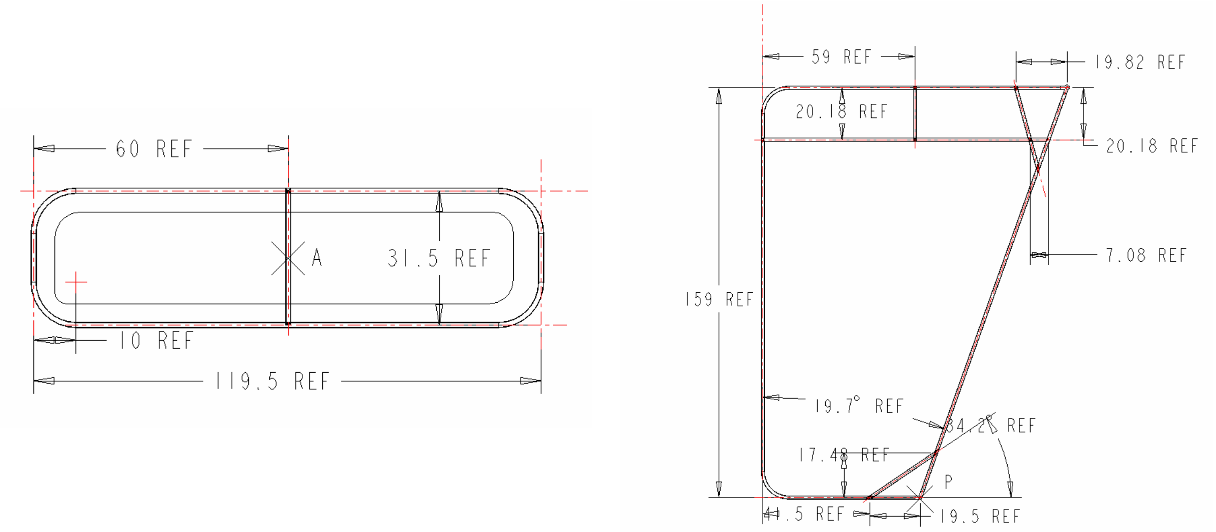

Figure 4.8 - Pieces of tail fin modeled in CAD with units in centimeters

In order to make the model more accurate, load patches and tethers were added to the balloon. The load patches were modeled using the same material as the shell. The confluence point tethers and handling lines were also modeled using the measured lengths and weights. Carabineers at the nose and tail were also included in the model of the shell, as well as servo motors and the appropriate linkages. Figure 4.9 shows the final rendered model.

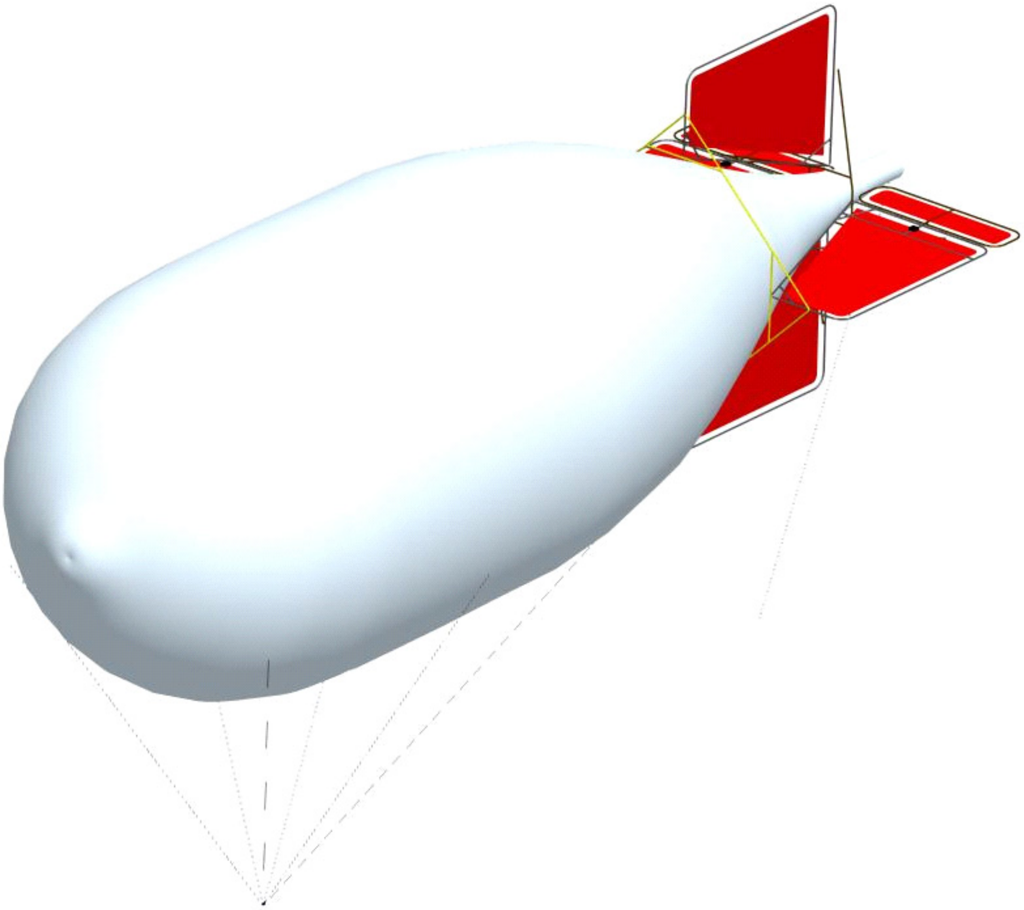

Figure 4.9 - Final rendered Pro-Engineer model of the aerostat

4.3.3 Summary of the Physical Parameters

As outlined earlier, Pro-Engineer was used to determine the center of buoyancy, center of mass, and inertia properties of the aerostat. It was also used to estimate the total volume of the aerostat. The rotational inertia of the Helium gas was not included in the dynamics model because the Helium is not a solid mass. It may not be compelled to rotate by rotations of the balloon, and therefore, its effect is small and can be neglected. All of the physical parameters for the aerostat are given in Table 13.

Table 13 - Summary of the physical parameters of the aerostat

Parameter	Variable	Value
Maximum diameter	D	2.95 m
Total hull length	L	8.76 m
Length (nose to fin leading edge)	l_H	6.50 m
Total volume	V	35.15 m^3
Hull volume	V_H	35.15 m^3
Hull ref area $(V_H)^{2/3}$	S_H	10.73 m^2
Hull fineness ratio	f	2.97
Total Mass (includes mass of helium)	m	19.77 kg
Buoyancy (mass of displaced air only)	F_B	437.2 N
Free Lift $(F_B - mg)$		243.4 N
Center of Mass (from nose)		
– includes mass of helium	x_{CMN}	-4.85 m
– no instruments	y_{CMN}	0 m
	z_{CMN}	-0.18 m
Center of Buoyancy (from center of mass)		
	x_B	1.512 m
	y_B	0 m
	z_B	0.18 m
Confluence point (from center of mass)		
	x_T	2.71 m
	y_T	0 m
	z_T	-2.99 m
Moments of inertia		
– solid parts only, does not include helium	I_{xx}	17.72 kg m^2
	I_{yy}	95.21 kg m^2
– does not include instruments	I_{zz}	94.64 kg m^2
	$I_{xz}=I_{zx}$	-2.80 kg m^2

*density of air = 1.269 kg/m^3
*density of helium = 0.1753 kg/m^3

Table 13 shows the calculated gross free-lift of the aerostat. As a partial validation of the Pro-Engineer model this can be compared to the actual measured lift of the balloon. Beginning in August, the gross lift of the aerostat was measured before and after each flight. Table 14 presents the average lift recorded on these days and compares it to the lift calculated using the Pro-Engineer model.

Table 14 - Comparison of the measured gross lift from the experiment to the gross lift calculated by the simulation

Date	Measured Gross Lift (N)	% Deviation from Model (243.4 N)
August 23	237.6	-2.4
August 25	239.4	-1.6
September 8	231.0	-5.1
September 11	255.5	-5.0
September 12	248.1	+1.9
October 2	253.5	+4.1
October 5	253.1	+4.0

The values in Table 14 show that the gross-lift estimated by the CAD model is within 5.1% of the gross lift measured in the field. This is a very good correlation as the CAD model uses a constant value for the densities of air and helium and does not account for temperature differences (between August 23rd and October 5th, the temperature varied from 12 °C to 30 °C). It should be noted that the CAD model presumes that the balloon contains 100% pure Helium, whereas, in reality the Helium purity tends to degrade with time.

4.4 Aerodynamic Parameters

To determine accurate aerodynamic parameters such as drag coefficients for the aerostat, equations based on empirical evidence were used. Equations (4.6) and (4.7) require the computation of integrals calculated from the hull geometry. To compute these integrals, the polynomial describing the shape of the hull (section 4.3.1) was used.

4.4.1 Hull Drag Coefficients

The hull of the aerostat has a streamlined shape for which we can accurately estimate the drag using conventional empirical methods. Blevins presents the drag of a streamlined body of revolution at zero angle of attack, based on the total wetted surface area [34]:

$$C_D = C_{D_{plate}} \left[1 + 1.5 \left(\frac{t}{L} \right)^{3/2} + 7 \left(\frac{t}{L} \right)^3 \right] \tag{4.13}$$

Where t = 2.95 m is the diameter of the body, L =8.76 m is the length, and

$$C_{D_{plate}} = \frac{0.0303}{\mathrm{Re}^{1/7}} \tag{4.14}$$

where $\mathrm{Re} = UL/\nu$, U is the wind speed, and ν is the kinematic viscosity of air. The drag coefficient used in the simulation is referenced to $V^{2/3}$ where V is the hull volume. Therefore the coefficient found in equation (4.13) must be scaled by the wetted area:

$$\left(Cd_c\right)_o = C_D \frac{A_{wetted}}{V^{2/3}} \tag{4.15}$$

For the TRF aerostat with a wind velocity of U = 5 m/s, with A_{wetted} = 59.8 m^2, and V = 35.2 m^2, this gives a $(Cd_c)_o$ of 0.0314.

Previous research [33] has estimated the cross flow drag coefficient for the hull $(Cd_c)_h$ using the drag coefficient for a cylinder. Other research [13] has used experimental data and curve fitting techniques to approximate this coefficient. The method of using a cylinder to estimate $(Cd_c)_h$ is a rough approximation. It will generally overestimate the value unless the end effects of the cylinder are taken into account. As well, generalizing the shape of the aerostat as a cylinder is a crude approximation. Therefore the cross flow drag coefficient, $(Cd_c)_h$, was found by averaging the values for three different aerostats given by Jones and Delaurier [13] giving a cross flow drag coefficient of $(Cd_c)_h$ = 0.191

The hull efficiency factor η_k, was determined by the method shown in Jones and Delaurier [35], and was found to be η_k = 1.1.

4.4.2 Tail Fins

Blevins [34] gives a table of values for the normal-force coefficient as a function of angle-of-attack for various finite flat plates with different aspect-ratios. Figure 4.10

shows the normal-force coefficient for three of these plates with interpolated values for a plate with the TRF tail-fin aspect ratio (1.34).

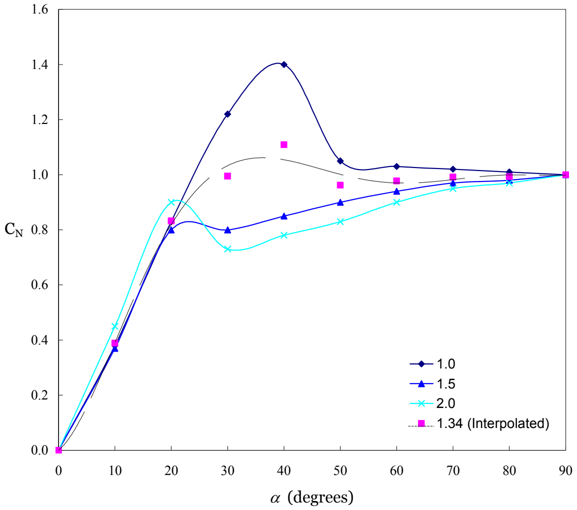

Figure 4.10 - The normal force coefficient for a finite flat plate with various aspect ratios [34].

A sixth order polynomial was calculated to fit the interpolated points for the aspect ratio of 1.34.

$$C_N = 9\times10^{-11}\alpha^6 - 3\times10^{-8}\alpha^5 + 3\times10^{-6}\alpha^4 - 0.0002\alpha^3 + 0.0037\alpha^2 + 0.017\alpha + 0.0001 \tag{4.16}$$

Where α is the angle-of-attack of the flat plate. The normal-force can be decomposed into components in line with the wind and perpendicular to the wind. These components are effectively the lift and drag, which can therefore be calculated from:

$$C_L = C_N \cos\alpha \tag{4.17}$$

$$C_D = C_{DO} + C_N \sin\alpha \tag{4.18}$$

Where C_{DO} is the zero-angle drag coefficient, C_L is the 3-D lift coefficient, and C_D is the 3-D drag coefficient.

The horizontal fins on the TRF are equipped with trailing edge control surfaces. In order to calculate the lift and drag of a flat-plate with a control surface deflection, a modified angle of attack was calculated. This angle of attack assumes that a flat-plate with deflected flap can be considered as a flat plate with a chord line from the leading edge to the tip of the trailing edge. This assumption ignores any effect that the camber of the fin may have on the lift. This modified angle of attack is shown in Figure 4.11 as α'.

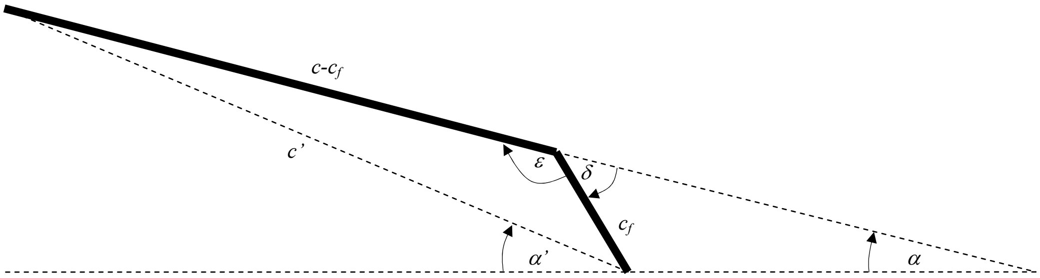

Figure 4.11 - Diagram of a flap plate with a deflected flap showing the definition of α'

We know the angle of attack α, the flap deflection δ, the total fin chord c, and the flap chord c_f. To calculate α' from Figure 4.11:

$$\varepsilon = \pi - \delta$$

$$c' = \sqrt{c_f^2 + (c - c_f)^2 - 2c_f(c - c_f)\cos\varepsilon} \tag{4.19}$$

$$\alpha' = \delta + \alpha - \cos^{-1}\left(\frac{c_f^2 + c'^2 - (c - c_f)^2}{2c'c_f}\right)$$

The new α' was calculated using equation (4.19) and then used in equation (4.16) to calculate the normal force coefficient. Equations (4.17) and (4.18) were then used with α' to calculate the lift and drag force coefficients.

McCormick [36] presents an alternative method for calculating the lift and drag coefficient for a control surface deflection:

$$C_L = C_{l\alpha}(\alpha + \tau\eta\delta)AR_{cor} \tag{4.20}$$

$$C_D = C_{Do} + C_L \tan\alpha \tag{4.21}$$

Where $C_{l\alpha}$ is the 2-D lift coefficient (taken as 2π), and δ is the flap deflection. The constant τ is determined from flap geometry and η is a function of the flap deflection and flap geometry. They can both be found from figures 3.35 and 3.36 of McCormick [36].

AR_{cor} *is* the correction for the aspect ratio. From [36], the correction is given as:

$$AR_{cor} = \frac{A}{A + 2\left(\frac{A+4}{A+2}\right)} \tag{4.22}$$

where A is the aspect ratio of the fin.

Equations (4.20) and (4.21) are only valid for the linear portion of the 2-D lift curve. Beyond 20 degrees the equation is no longer valid and the lift coefficient is modelled as a flat-stall (not increasing).

Figure 4.12 shows the calculated lift and drag coefficients for a flat plate with aspect ratio 1.34 and a chord ratio c_f/c = 0.16. This figure also shows, for comparison, the linear section of the lift coefficient and corresponding drag coefficient that is calculated using the method from McCormick [36].

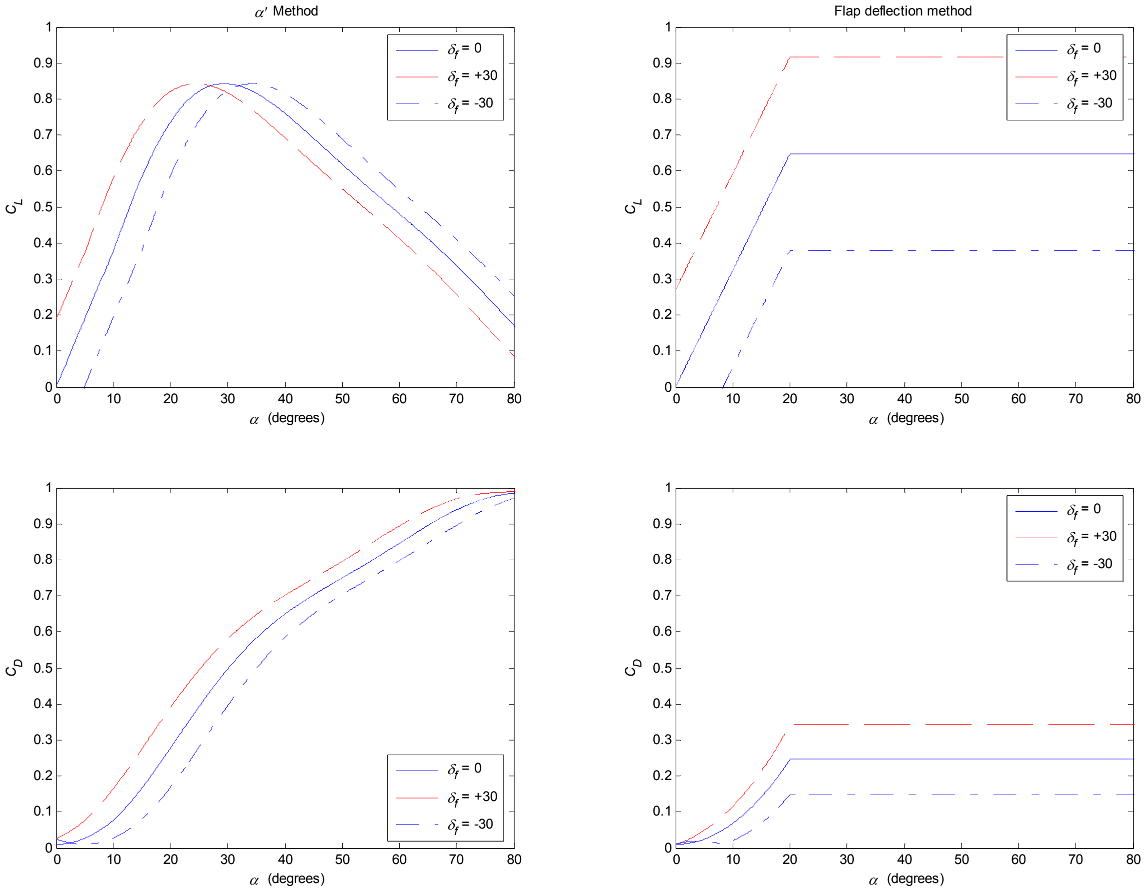

Figure 4.12 - 3-D lift and drag coefficients calculated using α' and calculated using McCormick's flap deflection method

Comparing the two methods shown in Figure 4.12, it appears that the α’ method results in a smaller change in lift due to a flap deflection than is calculated by McCormick. This is likely due to the fact that it does not consider the camber of the plate with a deflected flap. However this method has the advantage that it is valid beyond the stall angle, while McCormick’s method is only valid for the linear portion of the lift coefficient and the behaviour at high angles of attack is likely incorrect. Because the aerostat spends a large amount of time near or beyond the stall angle, it is important that this area is well modelled. Therefore, the α’ method was chosen to determine the lift and drag coefficient.

4.4.2.1 Zero Angle Drag Coefficient

The tail fins of the TRF aerostat can be described as flat plates framed by 12 mm diameter aluminium tubing. Figure 4.13 shows the tail section of the aerostat and the horizontal fins are visible. The aluminium tubing is the first part of the fin to contact the air flow.

Figure 4.13 - Rear section of the TRF aerostat showing fin construction. Note that the control surfaces have not been installed.

The zero-angle drag coefficient of the fins was modelled as a flat plate compensated with the drag induced by the leading edge aluminium tubing. The drag coefficient for a 2-D cylinder with a long splitter plate is given by [37] referenced to the diameter:

$$C_{D,cyl} = 0.59 \tag{4.23}$$

The drag coefficient of a one-sided flat plate is given by [34] referenced to the surface area:

$$C_{D,plate} = \frac{0.0303}{\left(Uc/\upsilon\right)^{1/7}} \tag{4.24}$$

where U is the wind speed, c is the total chord, and υ is the kinematic viscosity of air. To apply this as the zero-angle drag coefficient in equation (4.18) it must be doubled to take into account both sides of the plate. Furthermore, equation (4.23) must be compensated so that it is referenced to the total fin area. The zero angle drag coefficient is found by combining the values from (4.23) and (4.24).

$$C_{D0} = 2 \cdot C_{D,plate} + \frac{D}{cb} C_{D,cyl} \tag{4.25}$$

Where D is the diameter of the tubing (12.1 mm), U is taken as 5 m/s and ν is 1.56×10^{-5} m^2/s.

4.4.3 Summary of Aerodynamic Parameters

Table 15 summarizes each of the aerodynamic parameters for the TRF aerostat which are found as described in the preceding sections. The added mass was determined by using the hull's fineness ratio (total hull length/hull maximum diameter) to estimate the added mass coefficients (described by Jones in [35]). The added mass of the fins was ignored in these caculations.

Table 15 - Summary of the aerodynamic parameters calculated for the TRF aerostat

Parameter	Variable	Value
Hull efficiency factor	η_k	1.1
Hull cross flow drag coefficient	$(Cd_c)_h$	0.191
Zero angle drag hull drag coefficient (referenced to S_H)	$(Cd_h)_o$	0.0314
Hull integrals	I_1	1.718 m^2
	I_3	-22.598 m^3
	J_1	16.407 m^2
	J_2	53.609 m^3
Added mass coefficient	k_1	0.1237
Added mass coefficient	k_3	0.8017

4.4.3.1 TRF Modified Tail Fins

The dimensions of the tail fins and flaps are given in Table 16. Due to the flap on the horizontal fins, some parameters of the vertical fins are different. All calculations for the vertical fins were performed as described above, assuming a zero flap chord and zero fin deflection.

Table 16 – Tail Fin dimensions and parameters for the TRF aerostat

Parameter	Variable	Value
Vertical Fins		
Aspect Ratio	A_v	1.61
Vertical Fin Area	S_{fv}	4.07 m^2
Vertical Fin Chord	$\bar{c}_v$	1.59 m
Horizontal Fins		
Aspect ratio	A_h	1.34
Horizontal Fin Area	S_{fh}	4.89 m^2
Horizontal Flap chord	c_{fh}	0.32 m
Horizontal Fin Chord	$\bar{c}_h$	1.91 m
All Fins		
Span	b	2.56 m
2D Lift coefficient	$C_{l\alpha}$	2π /rad
Drag coefficient	C_{D0}	0.01049
Area of fin covered by hull	S_{fh}	1.22 m^2
Fin Span (tip to tip)	b	2.56 m
Center of Pressure (from c.g.)		
Top Fin		
		$x = -2.53$ m
		$y = 0.00$ m
		$z = 1.09$ m
Bottom Fin		
		$x = -2.53$m
		$y = 0.00$ m
		$z = -0.73$ m
Starboard Fin		
		$x = -2.53$ m
		$y = -0.91$ m
		$z = 0.00$ m
Port Fin		
		$x = -2.53$ m
		$y = 0.91$ m
		$z = 0.00$ m

4.5 Wind Model

The wind model is the only input to the simulated dynamics model of the aerostat. Therefore, it is important that the wind model be an accurate representation of the wind experienced by the aerostat in the field. The wind model used by Coulombe-Pontbriand

[11] and Lambert [16] was modified here in order to improve the representation of actual experimental flights. The method of collection and analysis of the experimental data was outlined in section 3.1.

Several characteristics of the experimentally measured wind were used to ensure the model used in the simulation provided good correspondence:

- The power-law exponent calculated from the experimental data was used to generate a height dependent mean wind-profile.
- Low-order polynomials were fitted to the wind speed and the wind direction. This improved the low-frequency similarity of the wind model.
- The turbulence of the experimental wind was approximated using a Von Karman spectrum [11]. The intensities of the turbulence in each direction were adjusted to match the experimentally measured wind turbulence.

4.5.1 Power Law

The simulation uses a height-dependent wind speed based on a power law profile. This allows the wind speed to be determined at any height using a reference wind speed and a calculated exponent variable.

$$\overline{U}_z = \overline{U}_g \left(\frac{z}{z_g} \right)^m \tag{4.26}$$

The exponent *m* is determined from experimental results for each flight (see section 3.1.2). $\overline{U}_g$ is the gradient wind speed which is chosen to be at a height of $z_g = 300$ m. Equation (3.4) is re-arranged to determine the gradient wind speed based on the experimentally measured mean wind speed at the reference height of 9.7m (the height of our uppermost wind sensor).

4.5.2 Mean Wind Speed

In order to better replicate the wind speed from each experimental flight, a sixth-order polynomial was fitted to the experimental data. This gives a good representation of the low-frequency characteristics of the wind speed. Figure 4.14 shows a calculated sixth-order polynomial, denoted by U^*_{ref}, with experimental data.

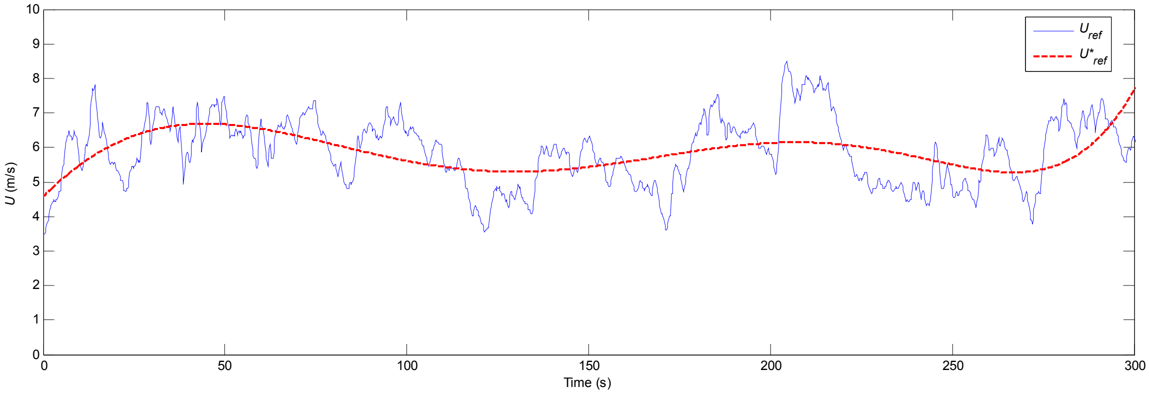

Figure 4.14 - Experimentally measured wind speed at the reference height with calculated sixth-order polynomial

The calculated polynomial is then used in place of $\overline{U}_z$ in Equation (3.4) giving:

$$\overline{U}_g = \overline{U}^*_{ref}\left(\frac{300}{9.7}\right)^m \tag{4.27}$$

$\overline{U}_g$ is then calculated at each time step of the simulation using the polynomial representation of the reference wind speed and the calculated exponent.

4.5.3 Wind Direction

The original wind model used by Lambert and Coulombe-Pontbriand does not account well for large, low frequency, changes in the wind-direction. It assumes that the mean-wind direction is constant and any changes in direction are accounted for by the superimposed turbulence. It was found that a better representation of the wind direction could be created by representing the mean wind-direction as a function of time. Figure

4.15 shows a segment of experimentally measured wind direction along with the corresponding calculated sixth-order polynomial.

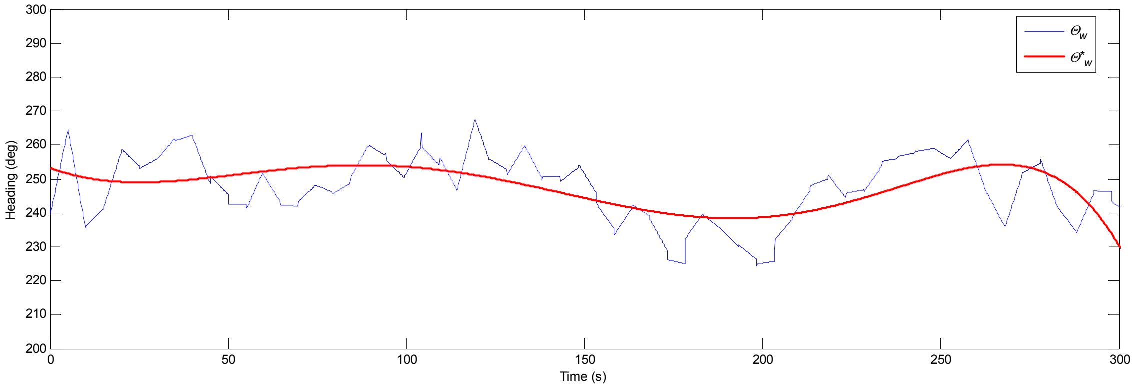

Figure 4.15 – Experimentally measured wind direction with a calculated sixth-order polynomial

A sixth-order polynomial was calculated for each experimental flight segment giving the wind direction as a function of time. This was implemented in the simulation to calculate the wind's direction.

4.5.4 Turbulence

The wind model functions by superimposing x, y, and z turbulent gusts onto the mean wind speed. The wind turbulence can be quantified by the turbulence intensity, which is the standard deviation of the wind speed in the direction of interest, normalized by the local mean wind speed ($\sigma_i / \overline{U}$). In order to determine the standard deviations σ_u, σ_v, and σ_w, the wind speed must be decomposed into x, y, and z directions.

The experimental data was decomposed into its component directions along a coordinate system aligned with the presumed mean wind. As noted in the preceding section, this direction varies with time. Figure 4.16 shows the vector representation of the decomposition of the mean wind speed.

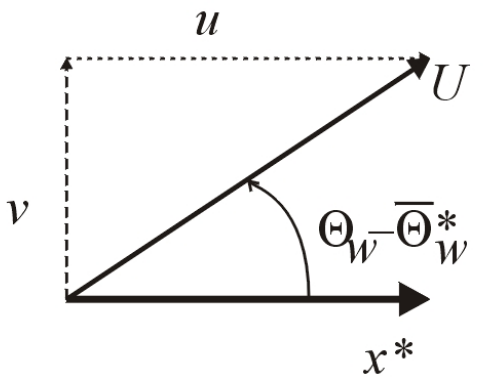

Figure 4.16 – Vector representation of the decomposition of the wind speed into *x* and *y* directions.

where

x^* is the direction of the polynomial fitted to the wind direction

U is the instantaneous wind speed

Θ_w is the instantaneous direction

$\overline{\Theta}_w^*$ is the direction from the polynomial fit,

u is the x^* component of the instantaneous wind speed

v is the y^* component of the instantaneous wind speed.

The *z* component is not approximated using this method because no measurement of the *z* direction of the wind speed is available.

Figure 4.17 and Figure 4.18 show the results of decomposing a segment of experimental wind into the *u* and *v* components. The mean of the *v* component is approximately zero which demonstrates that the approximation with a low-order polynomial is a good representation of the mean wind direction.

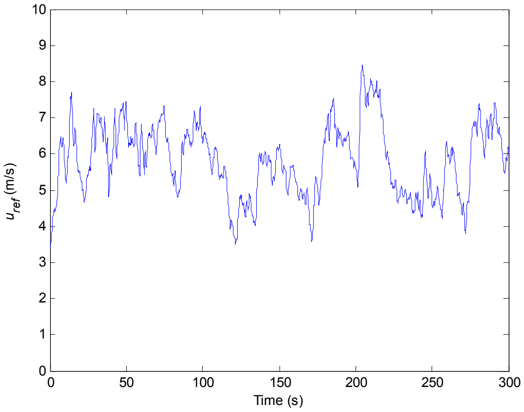

Figure 4.17 - Wind speed component the *x direction**

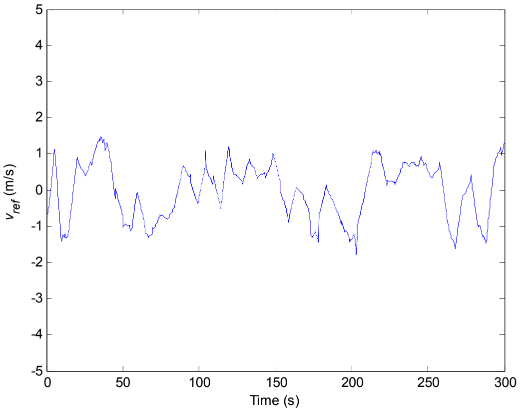

Figure 4.18 - Wind speed component in the *y direction**

Coulombe-Pontbriand used ESDU data curves as a method to estimate the turbulence intensities in the *x*, *y*, and *z* directions as functions of height [11]. The ESDU relationships for heights less than 300m are given by:

$$\frac{\sigma_u}{\overline{U}} = 3.51\left(\frac{1}{z}\right)^{0.01} - 3.23$$

$$\frac{\sigma_v}{\overline{U}} = 2.13\left(\frac{1}{z}\right)^{0.01} - 1.95 \qquad (4.28)$$

$$\frac{\sigma_w}{\overline{U}} = 1.17\left(\frac{1}{z}\right)^{0.01} - 1.06$$

Where σ_u, σ_v, and σ_w are the standard deviations of the wind speed in the component directions, and $\overline{U}$ is the local mean wind speed. For each experimental flight, the turbulence intensity was compared to the intensity generated by the ESDU curves and the simulation. Figure 4.19 shows the ESDU curves and experimental data from flight segment #8 on August 23rd. Note that no information is available with respect to the experimental *z* turbulence intensity

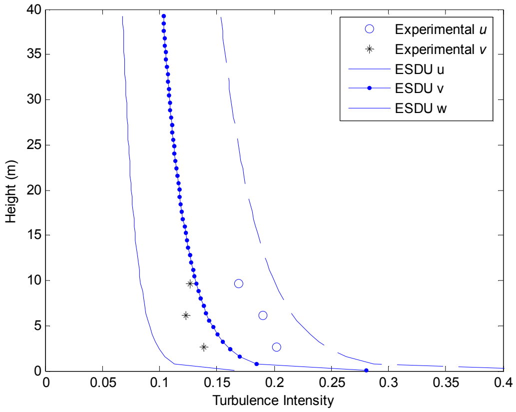

Figure 4.19 - Turbulence intensities from the experimental segment #8 on August 23rd, compared to the turbulence intensities generated by the ESDU equations

The ESDU equations represent turbulence intensity in nominal stable wind conditions. In reality, turbulence intensity changes from day to day and the ESDU equations were therefore adjusted to reflect the conditions on a particular day. For the simulation, the ESDU equations given by equation (4.28) were scaled so that they generated values of $\sigma_u/\bar{U}$ and $\sigma_v/\bar{U}$ corresponding to those measured at the 9.7m tower. The *z*-turbulence was scaled so that the vertical wind gusts were similar to those measured experimentally in section 3.1.3. Figure 4.20 and Figure 4.21 show the time history and the power spectra for flight segment #8 (August 23rd) with the simulated turbulence scaled to match the experimental data. Note that the experimental data is sampled at 5 Hz and the simulated data at 10 Hz.

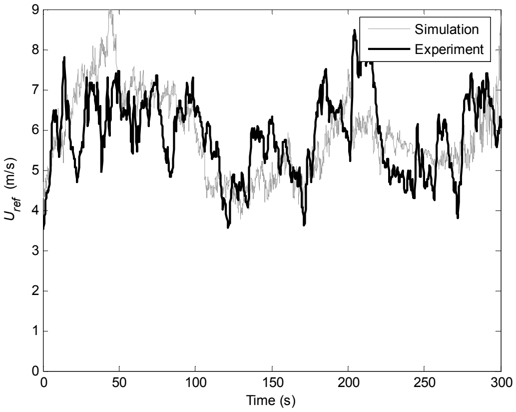

Figure 4.20 - Time history of the horizontal wind speed for flight segment #8 (August 23rd) compared to the wind data generated by the simulation

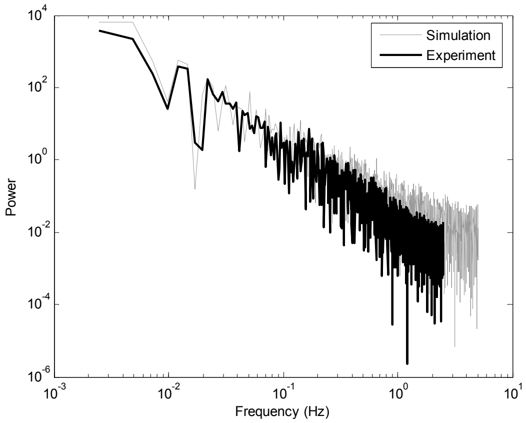

Figure 4.21 - Power spectrum of flight segment #8 (August 23rd) compared to the power spectrum generated by the simulation

The time history of the simulated wind speed is a reasonable representation of the experimental wind speed. It appears that the simulated wind has a more high frequency content but this is likely an artifact of the sampling rate or a limitation of the instrumentation. The power-spectra shown in Figure 4.21 shows a good match, especially at lower frequencies. It is known that the experimental sensor acts as a low pass filter (Section 2.3.4) and this would account for the reduced power at higher frequencies. In general, the wind model used in the simulation reproduces the general statistics of the in-field turbulence, but it was not intended to recreate the exact time history of the wind.

4.6 Simulation Results and Comparison

4.6.1 Comparison of Mean Values

As an initial comparison, the mean values of the tension, pitch angle, and aerostat *x*-position during experimental flights were compared to the mean values generated by the simulation. This allowed an initial evaluation of quality of the estimated parameters and provided a starting point for any necessary adjustments. The variation of each variable with respect to the mean wind speed was also evaluated. This provided a method to evaluate the general quality of the model over a range of wind-speeds. All of these comparisons were performed with zero tailfin deflection.

Figure 4.22 and Figure 4.23 show the experimental and simulation results for the tether tension, and the mean *x*-position of the aerostat, respectively. A trend-line has been plotted through the points to show the general behaviour with increasing wind-speed. The simulation results for both the tension and the mean *x*-position show a good match with the results from the experiment. The simulated tension appears to overestimate slightly the tension in the experiment; however the simulated values are within the range of values recorded during the experiment. The simulation also appears to overestimate the *x*-position and this difference becomes smaller with increasing wind speed. This combination of results indicates that the total drag may be overestimated and the lift of the aerostat may be underestimated, which could be caused by poor lift and drag coefficient estimates.

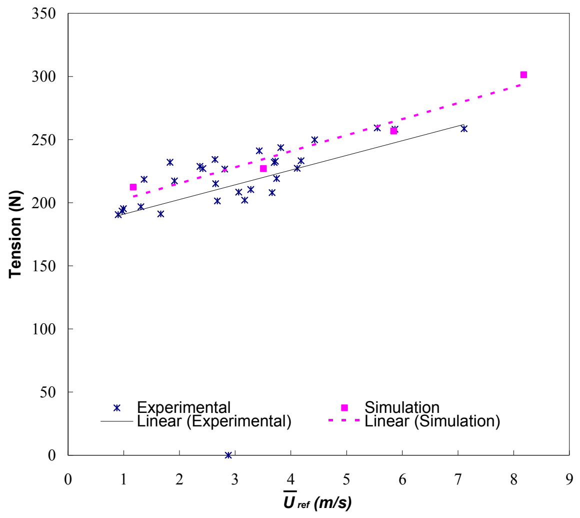

Figure 4.22 - Comparison of the mean tether tension recorded during experimental flights and the mean tension calculated by the simulation

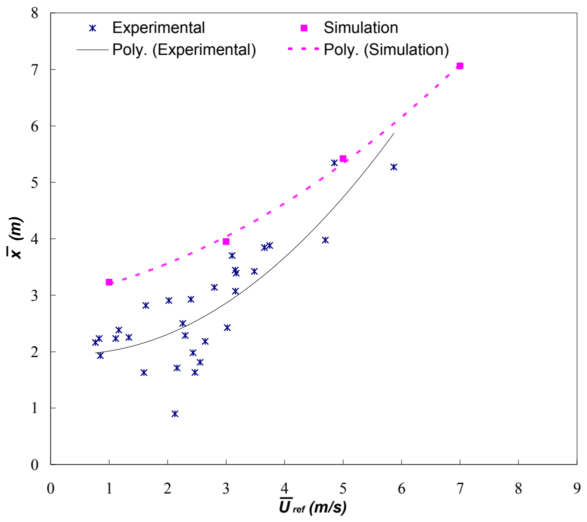

Figure 4.23 - Comparison of the mean *x*-position recorded during experimental flights and the mean *x*-position calculated by the simulation

Figure 4.24 compares the mean pitch angle from the simulation with the mean pitch measured experimentally. The pitch angle is also effectively the mean angle of attack of the aerostat, if we presume that the mean wind speed remains in the horizontal plane. The simulated results are well within the experimental values. The experimental results show a slight decrease in pitch (less negative) with increasing wind speed. The simulated results show a similar trend however the rate of increase in the simulation is slightly less than the rate indicated by the experiment.

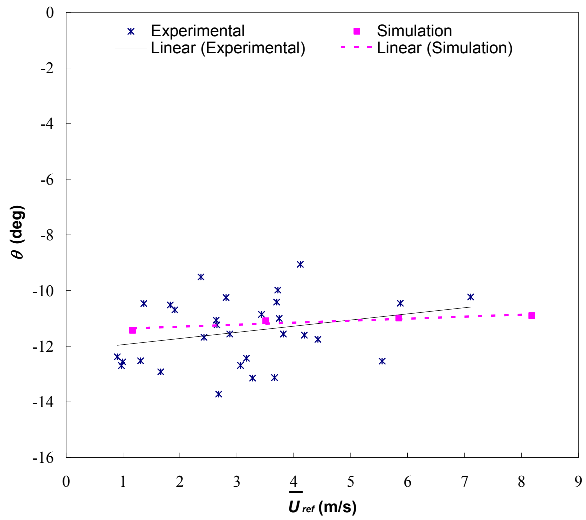

Figure 4.24 - Comparison of the mean pitch angle recorded during experimental flights and the mean pitch angle calculated by the simulation

4.6.2 Comparison of Dynamic Results

Three uncontrolled experimental flight segments with three different wind-speeds were chosen for validation and comparison with the simulation. For each flight segment, the wind-model was matched as outlined in section 4.5. Table 17 compares the experimental segments with the simulation on a statistical basis.

Table 17 - Comparison of statistical simulation results with three experimental flights

	$\overline{U}_{ref}$ (m/s)	$\frac{\sigma_u}{\overline{U}_{ref}}$	$\frac{\sigma_v}{\overline{U}_{ref}}$	$\frac{\sigma_w}{\overline{U}_{ref}}$	$\overline{F}_l$ (N)	σ_{F_l} (N)	$\overline{x}$ (m)	σ_x (m)	σ_y (m)	σ_z (m)	$\overline{\theta}$ (m)	σ_ϕ (deg)	σ_θ (deg)	σ_ψ (deg)
July 19 (#6)														
Simulation	3.07	0.23	0.13	0.11	230.7	12.3	-4.1	0.5	1.6	0.1	-10.9	2.5	0.6	4.3
Experiment	3.02	0.23	0.13	N/A	219.1	16.7	-2.4	1.5	2.2	0.2	-12.8	4.0	3.1	26.2
% diff	-1.8	0.0	0.5	N/A	-5.3	26.1	-68.4	65.0	30.1	65.3	14.6	36.6	79.6	83.5
Aug23 (#8)														
Simulation	5.86	0.17	0.13	0.10	274.4	38.8	-6.0	0.9	3.3	0.2	-10.5	5.3	1.1	5.4
Experiment	5.87	0.17	0.13	N/A	258.6	37.7	-5.3	2.5	5.5	1.0	-10.2	8.8	5.7	21.5
% diff	0.1	-2.1	-2.0	N/A	-6.1	-2.8	-13.2	65.4	40.8	78.2	-2.3	39.6	81.0	74.8
Aug23 (#9)														
Simulation	4.87	0.21	0.13	0.12	258.8	30.0	-5.3	0.9	2.8	0.2	-10.6	4.4	1.3	5.0
Experiment	4.85	0.21	0.13	N/A	258.2	41.5	-5.3	3.5	6.2	1.6	-10.5	10.9	6.4	22.7
% diff	0.4	0.9	5.2	N/A	0.2	27.7	1.0	74.5	55.2	88.9	1.0	59.9	78.9	78.2

In general, the 'non-dynamic' quantities show a good match. The mean tension, mean *x*-position, and mean pitch angle in the simulation are close to the values from the experiment. The dynamic variables (i.e the standard deviations) do not show nearly as good of match between the simulation and the experiment. The translational standard deviations are higher in the experiment by 30% to 89% and the rotational variables differ by 37% to 84%. This would suggest that the model does not correctly represent the dynamic behaviour of the aerostat.

Figure 4.25 shows the time-history of the translational variables of the simulation and the experiment. Even though the wind input in the simulation is based on the time history of the measured experimental wind, it is not intended to be temporally representative of the wind acting on the aerostat (which itself is not precisely known). Therefore, the time history of the aerostat motion cannot be directly compared between the simulation and the experiment. It is not expected that the two sets of results will match exactly; however the general motion and the amplitudes and frequencies should be similar. It is obvious from this figure that the experiment shows much larger fluctuations than the simulation, but the frequencies are comparable.

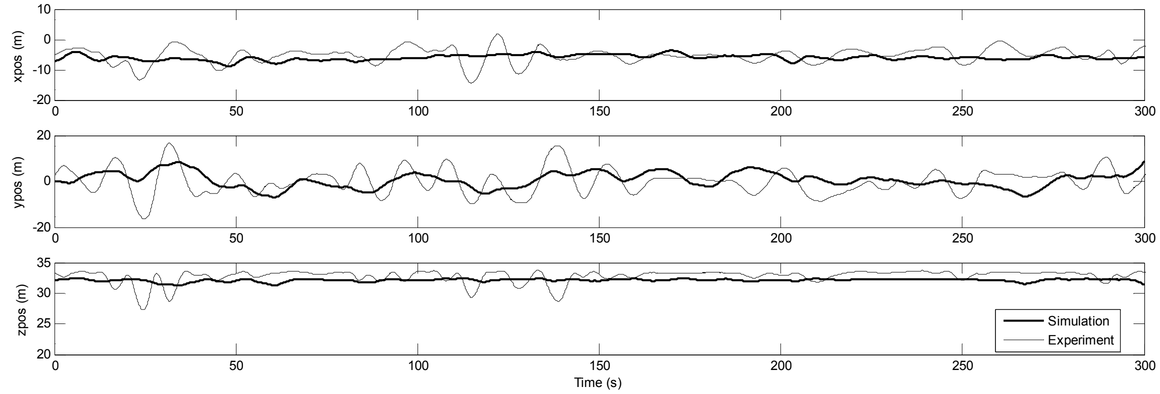

Figure 4.25 - Comparison of the translational results from the simulation with flight segment # 8 (August 23rd)

Similarly, Figure 4.26 shows the rotational variables. Again, the experiment shows much larger fluctuations than the simulation.

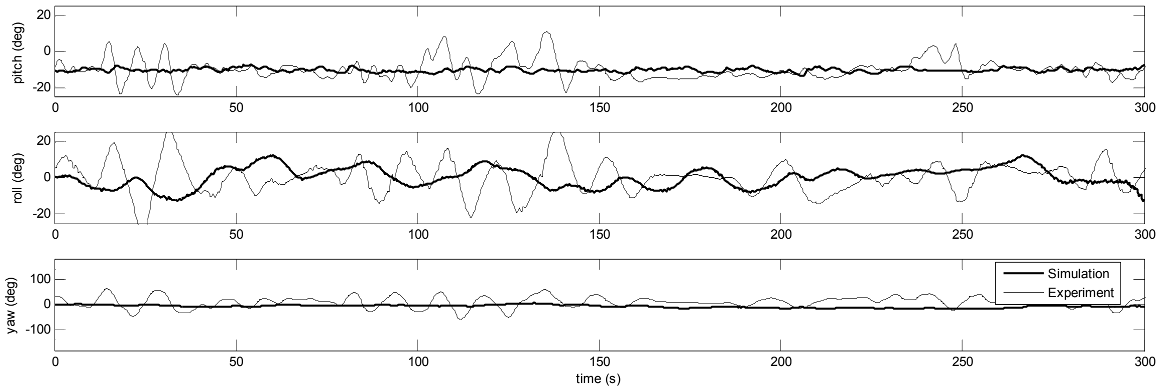

Figure 4.26 - Comparison of the rotational results from the simulation with flight segment # 8 (August 23rd)

Figure 4.27 compares the tension recorded experimentally, and the tension calculated by the simulation. This segment had the most similar results with the simulated standard-deviation being 2.8% larger than the experimental standard deviation. As noted in Table 17, the standard deviation of the tension was approximately 27 % higher in the experiment than that in the simulation for flight segments 6 and 9.

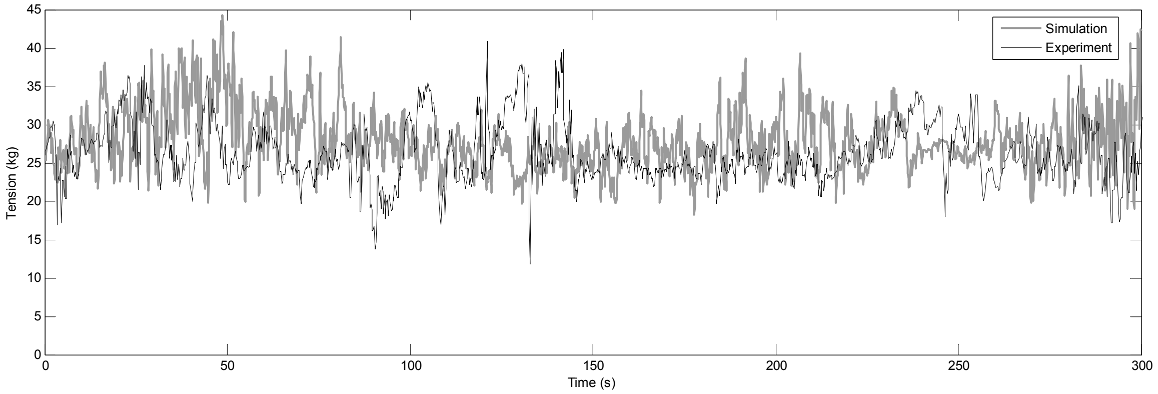

Figure 4.27 - Comparison of the tension results from the simulation with flight segment # 8 (August 23rd)

The results in Table 17 indicate that the simulation does not properly model the dynamic behaviour of the aerostat. The exact source of this weakness is unknown but some aspects of the simulation can be identified as possible areas for improvement.

A substantial effort was made to duplicate the experimental wind conditions as best as possible in the simulation, but the wind model is still a candidate for improvement. In the experimental setup, as outlined in section 2.3.4, the wind is recorded by three wind sensors, located on a tower near the ground. In order to duplicate the wind experienced by the aerostat, the wind must be measured closer to the aerostat and then this recorded wind would have to be implemented in the simulation.

The vertical wind gusts generated in the simulation are a best guess. They are based on the ESDU curves and a single day of measurements. To improve the wind-model, an accurate way of measuring the vertical wind gusts as close to the aerostat as possible is needed.

4.6.3 Simulation of a Controlled Aerostat

Because of the weakness of the dynamic simulation, any attempt to examine the validity of the controllable fin model is difficult. The dynamic pitch behaviour of the modelled aerostat is not a good match with the experimental results. The model must be refined so that it matches well with the experiment before a simulation of the aerostat with controllable tail fins can be rigorously performed.

As an initial assessment of the controllable fin model, the open-loop response of the fins to a step input was examined. This simulation was similar to the experiment described in Section 3.2.4; however the turbulent wind model was omitted from the simulation and only a mean wind speed was used. The turbulent model was omitted because only the steady state effect of the fins was of interest. For comparisons, the mean wind speed from the July 17th flight was used. Figure 4.28 and Figure 4.29 show the simulated aerostat's response to a positive and negative control surface deflection.

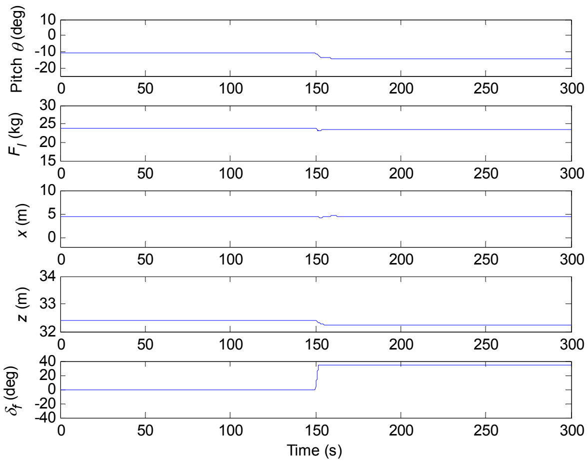

Figure 4.28 – Simulated aerostat response to a positive 35 degree step change in flap deflection

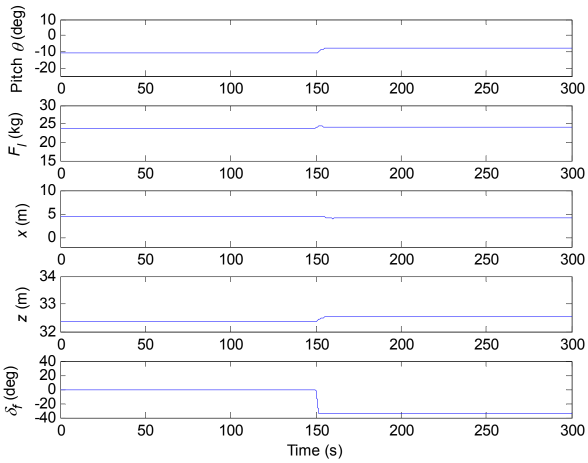

Figure 4.29 - Simulated aerostat response to a negative 35 degree step change in flap deflection

As expected, the positive fin deflection (fin rotating trailing edge upwards) causes the pitch angle of the aerostat to become more negative (nose up). This is consistent with the behaviour of the experimental aerostat. Table 18 gives the simulated mean values of the pitch angle, tether tension, *x*-position, and height for different fin deflections.

Table 18 – Simulated Mean pitch response to a step input control surface deflection

δ_f (deg)	$\bar{\theta}$ (deg)	$\bar{F}_l$ (kg)	$\bar{x}$ (m)	$\bar{z}$ (m)
0	-11.1	23.78	4.29	32.39
35	-14.1	21.48	4.43	32.23
-35	-7.98	24.08	4.15	32.53

On an order of magnitude scale, the results in Table 18 show a good correlation with the experimental results given in Table 8. The values for the tension, *x*-position, and height show such little change that they are not worth comparing with the experiment except in a directional sense. The tension increases and decreases in the same direction as the experimental flight, demonstrating that the overall lift and drag calculation of the simulation is correct.

Both the *x*-position and the *z*-position show a different behaviour in the simulation than in the experiment. In the experiment, for both a positive and negative flap deflection, the *x*-position increases, and coupled with that increase, the *z*-position decreases. In the simulation, a different effect occurs due to the flap deflection. A positive flap deflection causes an increase in the *x*-position coupled with a decrease in the *z*-position. For a negative flap deflection, the opposite occurs. These differences are summarized in Table 19.

Table 19 - Overview of different x-position and z-position response to positive and negative flap changes

	***x*-position**		***z*-position**	
Flap change	Sim	Exp	Sim	Exp
+	+	+	-	-
-	-	+	+	-

The differences between the simulation and experiment outlined in Table 19 are likely due to an underestimate of the drag caused by the tailfin deflection in the simulation. It appears that in the experiment, the drag caused by the fin deflection change is greater than the change in drag caused by the pitch change of the aerostat. In the experiment, when the flaps are deflected, the overall drag of the aerostat increases. In the simulation, when the flaps are deflected in the positive direction, the drag of the aerostat decreases (due to the reduction in pitch angle of the aerostat).

The magnitude of the pitch angle change is sufficient for a useful comparison. Table 20 presents the magnitude change in pitch to a step change in control surface deflection in the simulation and in the experiment. Considering that the experimental results were obtained under turbulent wind conditions (Section 3.2.4) and the simulation only uses an approximation of this wind speed (Section 4.5.2), this match is good.

Table 20 - Comparison between the simulated and experimental pitch angle change caused by a control surface deflection

δ_f (deg)	Simulated $\Delta\bar{\theta}$ (deg)	Experimental $\Delta\bar{\theta}$ (deg)
35	-3.0	-2.7
-35	3.1	1.4

The closed-loop control system used experimentally, and described in section 3.2.5 was implemented in the simulation. As discussed in Section 4.6.2, the modelled aerostat does not re-create well the dynamics of the experimental aerostat; nevertheless the closed-loop simulated response was tested to verify its effectiveness, functionality, and to give a qualitative analysis of the behaviour of a controlled aerostat. Figure 4.30 shows the modelled response of the pitch angle with proportional (k_P = 0.2 rad/deg) only closed-loop control and without, using simulated wind conditions from the August 23rd flight.

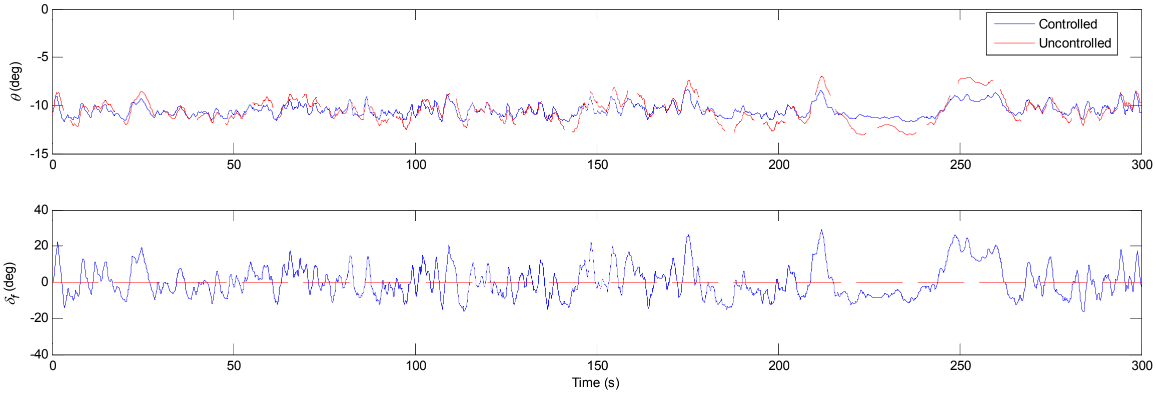

Figure 4.30 – Modeled pitch angle and flap deflection for the closed- loop controlled and the uncontrolled response of the aerostat

Similar to observations from the experimental flights, shown in Figure 3.18, the modelled closed-loop control is effective at reducing the pitch perturbations of the aerostat. The modelled control system also actuates the control surfaces similarly to the response seen experimentally (Section 3.2.6). As in the experiment, the actuated tailfins appear to reduce the magnitude of the low frequency motion, while having little impact on the high frequency as seen in Figure 4.31

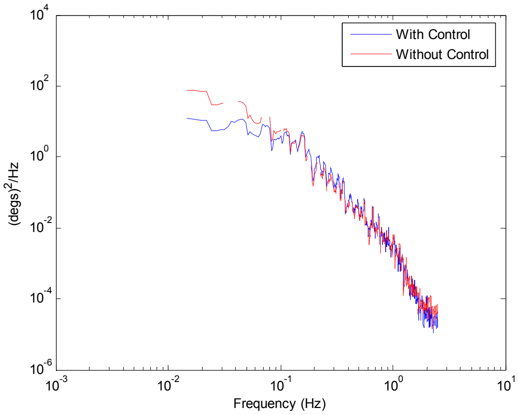

Figure 4.31 - PSD of a five minute simulated segment with P-control and uncontrolled using simulated wind from the August 23rd flight

Unfortunately, the dynamics of the modeled aerostat are quite different from the experiment. The pitch perturbations that occur experimentally are much larger than those that are seen in the model.

Based on the open loop results and a qualitative look at the closed loop response, the modelled control system reasonably duplicates the behaviour of the experimental control system. Before this can be rigorously verified, the dynamic model of the aerostat must be improved so that the results match the experimental results more closely.

Chapter 5 Conclusion and Recommendations

This research investigated the use of a streamlined aerostat with movable tail fins to control the pitching motion of an aerostat in a turbulent outdoor environment. The goal of the research was to reduce the pitch fluctuations of the aerostat by actively controlling the tail fins.

An 8.76 m long streamlined aerostat with four rigid tail fins was modified to include flap type trailing edge control surfaces on the horizontal tail fins. The aerostat was flown at an altitude of 30 m by a crew of two people and it was found to be a reasonable platform for small scale testing. A larger aerostat would not have been safe to operate with only two people; however, the small size severely limited the instrumentation that the aerostat could carry and it constrained the design of the controllable tail-fins.

The horizontal control surfaces were actuated using widely available robotic hobby servos. The maximum available servo torque of 2.35 Nm limited the chord of the control surfaces to be 0.32 m. The servos were easy to integrate with the control system; they performed reliably, and did not limit the actuation angle of the tail fins.

An instrumentation platform was constructed to house the airborne sensors which included a differential GPS system, a 3-axis tilt-sensor, and a load cell. Attitude and tension information were reliably captured at a rate of 5 Hz. The heading data supplied from the tilt sensor was reasonable considering its use of magnetometers and the unknown magnetic interference around the aerostat. Position data was collected at 10 Hz by a pair of high precision differential GPS receivers which, after post-processing, determined the 3-D position of the aerostat with accuracy better than 3 cm.

In addition to the instrumentation, the platform carried a DIGI wireless serial LAN, a conditioner for the load cell, a servo controller, and a custom made lithium-battery power system. The wireless serial LAN provided a reliable communications link between the ground station and the aerostat. It was highly configurable and it did not limit the sampling of data from the instrumentation system. The lithium-battery power system provided better than two hours of flight time and did not interfere magnetically with any of the sensors.

The ground station used for the control of the aerostat and data logging consisted of an electric winch, wind sensors, GPS, and a laptop computer. The electric winch had been successfully used in past research at McGill. Mounted on the winch was 1.75 mm Plasma polyethylene rope from Cortland Cable. The Plasma rope has a high strength-to-weight ratio and provided an estimated factor of safety of five and a 30 m length weighed less than 60 g.

Three wind sensors were fixed on a tower at 2.6 m, 6.1 m, and 9.7 m above the ground, approximately 10 m from the location of the winch. The wind sensors provided low frequency wind direction (0.2 Hz) and wind speed (5 Hz) data. They were limited to recording the wind speed and direction in the x-y plane parallel to the ground. The wind speed at the aerostat's height was extrapolated from the data using a power law. For the nine flights used in the analysis, the reference wind speed at the 9.7 m tower ranged from 1.0 m/s to 5.1 m/s. When the ground wind speed was higher than ~5 m/s the aerostat was not flown for safety reasons.

In order to obtain information about the wind speed in the vertical direction, a sonic anemometer was borrowed and used for a single day to record the 3-D wind field. The sonic anemometer was mounted near the regular wind sensors on a tower three metres above the ground. On a day where the mean wind speed in the horizontal plane was 2.3 m/s, vertical wind gusts in excess of 1 m/s were recorded. This indicated that an important component of the wind speed was not being measured during the experimental flights.

The mean wind speed was not adequate to describe the wind conditions during a particular flight, however it was the most consistent measure and therefore it was used as the standard by which the flights were compared. Using only the wind speed ignored the effects of the variability of the wind turbulence which ranged from 0.21 to 1.17 depending on the measured segment.

In order to characterize its motion and to establish a performance baseline, the aerostat was flown numerous times without active control. The aerostat showed a wide range of motion under different wind conditions. For example at a mean wind speed of 4.9 m/s, the pitch showed perturbations of as much as ± 20 degrees and the position variables had perturbations as large as 20 m. It was found that the motion perturbations were largest in the lateral direction and least in the vertical direction. This is because the lateral motion was the least constrained by the tether and the vertical motion was the most constrained.

The effectiveness of the tail-fin control surfaces was determined by measuring the open-loop response of the aerostat to a step change in the control surface deflection. These experiments were performed under turbulent wind conditions that made judging the effectiveness difficult. By taking the average of the aerostat position and orientation variables it was possible to determine the mean effect of the control surfaces. It was found that a negative control surface deflection had the effect of changing the mean pitch of the aerostat by -1.4 degrees and a positive deflection had an effect of +2.7 degrees. The effect of the control surface deflection on the mean tension in the tether was found to be negligible. This indicated that a controller to reduce the pitch perturbations had the most promise.

The results from the uncontrolled and open loop testing were used to develop the closed loop control system. A PID controller was field tested with various gains. The gains were initially estimated from the open-loop testing and then refined through an iterative process. It was found that a proportional controller with a gain of 0.2 rad/deg was the most effective controller. At a mean wind speed of 5.1 m/s, the controller was effective at reducing the pitch perturbations up to 0.2 Hz. The controller was not able to reduce the large magnitude perturbations because these were commonly coupled with other events (such as a roll) or the controller was saturated. At lower wind speeds, the controller was not as effective because the control surfaces were not being used to their full effectiveness. This indicated that the proportional control system was not adequate for changing wind conditions and that a gain-scheduled or adaptive controller would be more appropriate.

An additional goal of this research was to adapt a non-linear dynamic simulation of the aerostat originally developed by [17] and [16] to simulate the controllable aerostat used in this experiment. For the simulation, the physical parameters of the controllable aerostat were measured and the aerodynamic parameters were estimated using well established empirical relations. The aerostat was completely modelled using Pro-Engineer in order to determine its geometric properties. The shape of the hull was physically measured and this was used to generate the body’s shape in CAD. The Pro-Engineer model correctly estimated the gross-lift of the aerostat to within 5.1%. The model also supplied the other important geometric parameters such as the center of gravity and the moments of inertia. For the most part, the aerodynamic parameters were estimated using empirical relationships developed by Jones and Delaurier [13]. The aerodynamics of the tail fins was estimated using the lift and drag caused by a flat plate.

The wind model used by [16] and [11] was modified in order to improve its representation of actual experimental flights. For each experimental flight used for comparison a low-order polynomial was used to represent the slowly changing mean wind speed and direction. On top of this, turbulence scaled to match the experimental data was superimposed. This allowed for a good representation of the wind speed to be created; however no information about the vertical wind gusts was available for comparison with the simulation.

In general, the ‘non-dynamic’ quantities in the simulation showed a good match. The mean tension, mean *x*-position, and mean pitch were close to the values from the experiment. The dynamic variables did not show as good of a match between the simulation and the experiment. The translational variables differed from 30% to 89% and the rotational variables differed by 37% to 84% suggesting that the model does not correctly represent the dynamic behaviour of the aerostat.

Even though the dynamic pitch behaviour of the modelled aerostat was not a good match with the experimental results, both open-loop and closed-loop control were implemented and tested in the simulation.

The open-loop response of the fins to a step input was simulated and showed pitch behaviour consistent with the experimental aerostat. The tension also increased and decreased in the same direction as the experimental flight; however, both the x-position and the z-position showed a different behaviour in the simulation than in the experiment. This was likely due to an error in the estimate of the drag caused by the deflected fins.

The modelled aerostat does not re-create well the dynamics of the experimental aerostat but the closed-loop simulated response was tested to verify its effectiveness. Similar to observations from the experimental flights, the modelled closed-loop control was effective at reducing the pitch perturbations of the aerostat. It reduced the magnitude of the low frequency motion and had little impact on the high frequency motion.

The implementation of the open-loop and closed loop control in the simulation demonstrated that the simulated behaviour was in general the same as the simulation, however the dynamics of the modeled aerostat are quite different from the experiment and the pitch perturbations that occur experimentally are much larger than those that are seen in the model. The model must be refined and improved before the simulation can be used to design and analyze future control systems.

5.1 Recommendations

The development of the experimental system and the simulation used in this experiment was an iterative process. The work presented in this thesis is an extension of work done by [16] and [11] and there are several improvements that should be implemented in the next iteration.

The measurement of the vertical wind speed is a continuing weakness of this type of experiment. It is likely that the vertical wind gusts are an important feature to consider when characterizing experimental flights. Furthermore, there is little or no validation of the simulated vertical wind speed. The addition of a full time sonic anemometer mounted on the 10 m tower would provide large amounts of valuable data that could be used to improve the system performance and the simulation. In the same vein, investigating the addition of wind speed and direction measurements to the aerostat itself would be useful.

It was found that many of the large position disturbances of the aerostat showed a coupling of the roll, pitch, and yaw modes. The implementation of yaw control by adding vertical control surfaces to the tail fins would allow for the control of the three rotational axes of the aerostat.

It was evident from the experimental control results that a single proportional gain was not adequate for all flying conditions. A gain schedule or a controller that can adapt depending on the wind speed should be investigated.

Because the aerostat is relatively small, any additional weight has a large influence on the dynamics of the aerostat. An effort should be made to lighten the weight of the tail fins and the instrumentation platform. Novel materials such as carbon fibre could be used for the tail fins and instrument platform. Constructing the tail fins from carbon fibre would provide an additional benefit that the tail fins could be designed to be larger and more efficient.

Using the experimental results obtained in this thesis, the dynamics model used in the simulation should be refined. The results suggest that the wind model should be adequate to replicate the experimental wind and therefore the dynamics model should be examined in detail. It is possible that under highly turbulent conditions, and with a small aerostat, that some of the dynamic forces and their effect have not been adequately considered. The unsteady aerodynamic flow effects may have a significant due to the turbulent flow environment and ensuing rapid changes of flow conditions. Future simulation work should try accounting for these unsteady flow effects.

References

1. Makrinos, S., *High-Altitude Airships for Homeland Security Operations.* Sea Technology, 2005: p. 29-32.
2. Mayer, N., *Lighter-than-air-systems*, in *Aerospace America*. 2005. p. 30-31.
3. J.Hain and L. Harris, *Aerostats for Oceanic and Atmospheric Research.* Sea Technology, 2004: p. 75-80.
4. Dewdney, P., M. Nahon, and B. Veidt, *The Large Adaptive Reflector: A Giant Radio Telescope with an Aero Twist.* Canadian Aeronautics and Space Journal, 2002. 48: p. 239-250.
5. Veidt, B. *The Large Adaptive Reflector*. 2004 February 4, 2004 [cited June 23, 2007]; Available from: http://www.drao-ofr.hia-iha.nrc-cnrc.gc.ca/science/ska/.
6. TCOM. *TCOM's Lighter-Than-Air Products*. 2006 [cited June 23, 2007]; Available from: http://www.tcomlp.com/.
7. Deschênes, F., *A Study of Design Improvements for a Multi-Tethered Aerostat System*. Department of Mechanical Engineering. Masters of Engineering. 2005, Montreal: McGill University.
8. Badesha, S. and S.P. Jones, *Aerodynamics of the TCOM 71M Aerostat*, in *10th AIAA Light-Than-Air-Systems Technology Conference*. 1993: Scottsdale, AZ.
9. Jones, S. and L. Schroeder, *Nonlinear dynamics simulation of a tethered aerostat: A fidelity study.* Journal of Aircraft, 2001. 38(1): p. 64-68.
10. Lambert, C., *Dynamics and Control of a Multi-Tethered Aerostat Positioning System*. Mechanical Engineering. PhD. 2006, Montreal: McGill.
11. Coulombe-Pontbriand, P., *Modelling and Experimental Characterization of a Tethered Spherical Aerostat*. Department of Mechanical Engineering. Masters of Science. 2005, Montreal: McGill University.
12. DeLaurier, J.D., *A Stability Analysis for Tethered Aerodynamically Shaped Balloons.* Journal of Aircraft, 1972. 9(9): p. 646-651.
13. Jones, S.P. and J.D. Delaurier, *Aerodynamic Estimation Techniques for Aerostats and Airships.* Journal of Aircraft, 1983. 20(2): p. 120-126.

14. Jones, S.P. and J.A. Krausman, *Nonlinear Dynamic Simulation of a Tethered Aerostat.* Journal of Aircraft, 1982. 19: p. 679-686.

15. Jones, S.P. *Aerodynamics of a New Aerostat Design with Inverted-Y Fins*. in *6th Lighter-Than-Air Systems Conference*. 1985. Norfolk, VA: American Institute of Aeronautics and Astronautics.

16. Lambert, C.M., *Dynamics Modeling and Conceptual Design of a Multi-tethered Aerostat System*. Mechanical Engineering. Master of Applied Science. 1999: University of Victoria.

17. Nahon, M. *A Simplified Dynamics Model for Autonomous Underwater Vehicles*. in *IEEE Symposium on Autonomous Underwater Vehicle Technology*. 1996. Monterey, CA.

18. Driscoll, R. and M. Nahon. *Mathematical Modeling and Simulation of a Moored Buoy System*. in *Oceans*. 1996: IEEE.

19. Deschênes, F. and M. Nahon, *Design Improvements for a Multi-Tethered Aerostat System*, in *AIAA Atmospheric Flight Mechanics Conference and Exhibit*. 2005, AIAA: San Francisco, California.

20. Miller, J.I., *The Design of Robust Helium Aerostats*. Department of Mechanical Engineering. Master of Engineering. 2005, Montreal: McGill University.

21. Jacobs, E.N. and R.M. Pinkerton, *Pressure Distribution Over a Symmetrical Airfoil Section with Trailing Edge Flap*, National Advisory Committee for Aeronautics.

22. Hitec. *HSR-5995TG Digital Robotic Servo*. 2006 [cited 2006 November 1]; Available from: www.hitecrcd.com.

23. Hee, L.J., *General Specification of HSR-5995TG Coreless Digital Servo*. 2004: HITEC RCD Korea Inc.

24. Honeywell, *HMR3200/HMR3300 Digital Compass Solutions*: Honeywell Sensor Products - Solid State Electronics Center.

25. MicroStrain, *3DM-GX1 Detailed Specs rev2*, Williston, Vermont: MicroStrain.

26. Techniques, T. *Mini Low Profile Load Cell Universal / Tension or Compression*. 2005 [cited May 19, 2005]; Available from: www.transducertechniques.com/MLP-Load-Cell.cfm.

27. *D1000 and D2000 OMEGABUS Digital Transmitters*. 2006. C-79 - C-85.

28. Digi, *PortServer TS W MEI Product Data Sheet*. 2005: Digi International Inc.

29. *05103-10 R.M. Young Wind Monitor Instruction Manual*. 1996, Edmonton, Alberta: Campbell Scientific Inc.

30. *PMD-1208FS User's Guide*. 2004: Measurement Computing Corporation.

31. Paul B. MacCready, J. and H.R. Jex, *Response Characteristics and Meteorological Utilization of Propellor and Vane Wind Sensors.* Journal of Applied Meteorology, 1964. 3: p. 182-193.

32. Shenoi, B.A., *Introduction to Digital Signal Processing and Filter Design*. 2006: John Wiley & Sons, Inc.

33. Lambert, C. and M. Nahon, *Stability Analysis of a Tethered Aerostat.* Journal of Aircraft, 2003. 40(4): p. 705-715.

34. Blevins, R.D., *Applied Fluid Dynamics Handbook*. 1984, Agincourt, Ontario: Macmillan of Canada.

35. Jones, S.P. and J.D. Delaurier, *Lighter-Than-Air Vehicles*, in *Handbook of Fluid Dynamics and Fluid Machinery*. 1996, John Wiley & Sons Inc.: New York. p. 1741-1755.

36. McCormick, B.W., *Aerodynamics, Aeronautics, and Flight Mechanics*. 1995, Toronto: John Wiley & Sons, Inc.

37. Hoerner, S.F., *Fluid-Dynamic Drag*. 1958, New Jersey: Published by the Author.

Appendix A

Figure 5.1 shows the flight data from a five minute uncontrolled segment from September 11th at a mean wind speed 3.3 m/s.

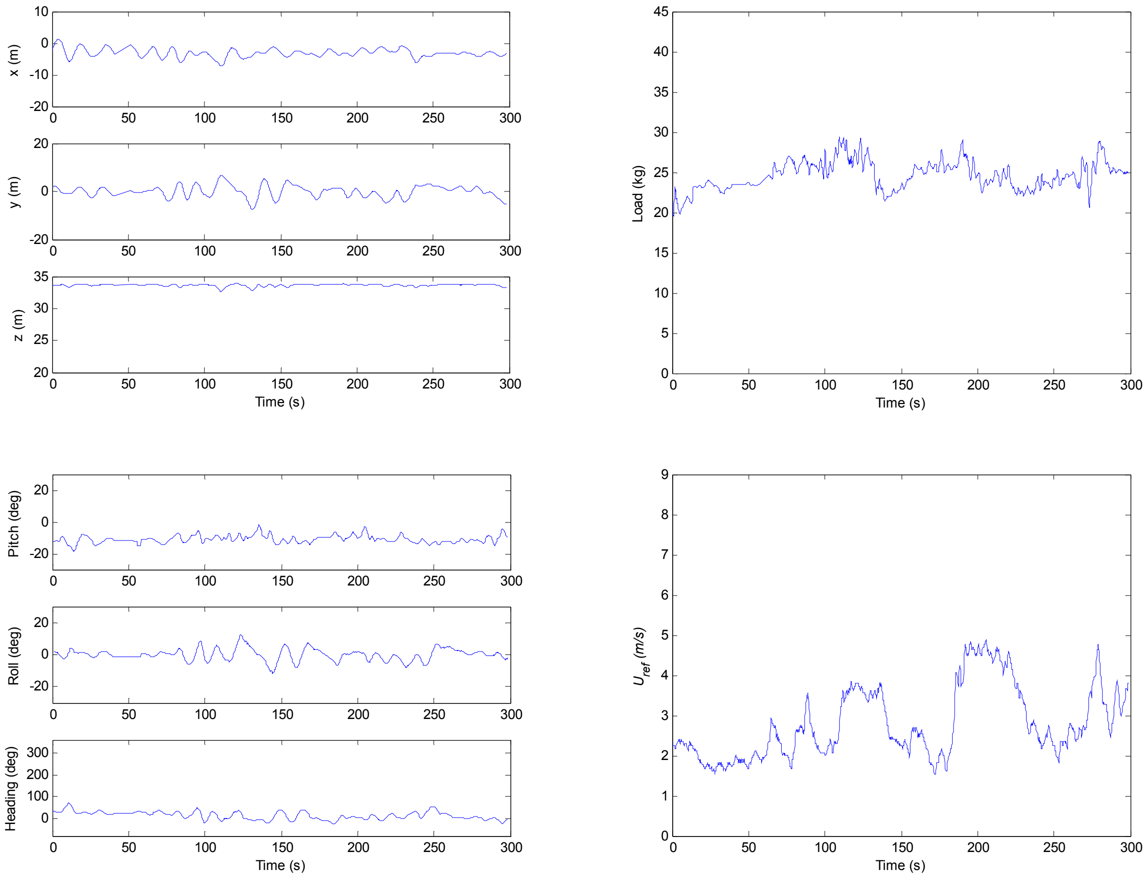

Figure 5.1 - Flight data for a segment of the September 11th uncontrolled flight